Lorenzo Cruciani

Ruthenium thin films: terahertz generation and direct laser patterning

Ruthenium thin films: terahertz generation and direct laser patterning

Lorenzo Cruciani

Ruthenium thin films: terahertz generation and direct laser patterning

ACADEMISCH PROEFSCHRIFT

ter verkrijging van de graad van doctor
aan de Universiteit van Amsterdam
op gezag van de Rector Magnificus
prof. dr. ir. P.P.C.C. Verbeek
ten overstaan van een door het College voor Promoties ingestelde commissie,
in het openbaar te verdedigen in de Agnietenkapel
op donderdag 1 mei 2025, te 10.00 uur

door Lorenzo Cruciani
geboren te Rome

Promotiecommissie

Promotor:	prof. dr. P.C.M. Planken	Universiteit van Amsterdam
Copromotor:	dr. N.J. van Druten	Universiteit van Amsterdam
Overige leden:	prof. dr. M.S. Golden	Universiteit van Amsterdam
	dr. R.J.C. Spreeuw	Universiteit van Amsterdam
	dr. J.A. Dijksman	Universiteit van Amsterdam
	dr. P.M. Kraus	Vrije Universiteit Amsterdam
	prof. dr. J. Gómez Rivas	TU Eindhoven

Faculteit der Natuurwetenschappen, Wiskunde en Informatica

This dissertation was typeset by the author using LaTeX 2_ε, originally developed by Leslie Lamport and based on Donald Knuth's TeX. The body text is set in 12 point Egenolff-Berner Garamond, a revival of Claude Garamont's humanist typeface.

A template that can be used to format a PhD dissertation with this look & feel has been released under the permissive AGPL license and can be found online from the github repository, at github.com/lhoangan/template-uva-thesis, which originates from its lead author, Jordan Suchow, at github.com/suchow/Dissertate.

UNIVERSITY OF AMSTERDAM

The work described in this thesis was carried out at the Advanced Research Center for Nanolithography (ARCNL). This work was partially funded by a grant from the Institute of Physics of the University of Amsterdam.

Пройду,
любовищу мою волоча.
В какой ночи'
бредово'й,
недужной
какими Голиафами я зача'т -
такой большой
и такой ненужный?

Passeró,
trascinando il mio enorme amore
in quale notte
delirante e malaticcia
da quali Golia fui concepito
cosí grande e cosí inutile?

I will pass by,
dragging my giant-love.
in what
delirious,
feverish night,
by what Goliaths was I conceived
so big
and so useless?

(*To His Own Beloved Self The Author Dedicates These Lines* ,
Vladimir Majakovskij, 1916)

Contents

1 Introduction

1.1 Materials development in human history

The advancement of technology in human history has been partially driven by the discovery and subsequent exploitation of novel materials. In some cases, the advent of a new material had such a strong impact on human societies that archaeologists and anthropologists found it useful to label pre-historical human eras based on certain materials. The material used for labelling an era was the one constituting most findings that dated back to that era. This scheme for ancient human history is called *three-age system* and was introduced by the Danish antiquarian Christian Jürgensen Thomsen in the 19^{th} century[1].
The system divides pre-historic periods in mainly three ages: the stone age (which lasted approximately 3.4 million years and ended around 4 000 BC), the bronze age (from 3 300 BC until 1 200 BC) and the iron age (from 1 200 BC until 550 BC).
Among the criticisms that were directed at the three-age system was its oversimplification of human societies. However, although a system that classifies based on the materials mainly used in a certain period is an oversimplification, it is beyond doubt that pre-historic tribal-based human societies were far more simple than more recent ones[2] and, of course, the present one.
The advent of the transistor and the subsequent development of the technology for information processing and transmission shaped the current socio-economical system so much that one might refer to the current age as the *silicon* or the *semiconductors* age. A different

1

view is often applied which slightly shifts the focus from the materials themselves, so that contemporary age is more commonly referred to as the *information age*[3]. The technological progress in this age is therefore strongly related to the development of data processing devices based on novel materials and techniques.
One of the barriers to overcome in order to avoid a stall in the evolution of this technology is illustrated by Moore's law[4]. This is the observation that the number of transistors in an integrated circuit for minimal cost per transistor tends to double every two years. The computational power of a chip depends on the number of transistors contained in it. For this reason, the capability to miniaturise the electronic components became one of the main challenges for semiconductor manufacturers.
The production of integrated circuits with increasingly small dimensions is based on *nanolithography*, a class of techniques which is described in the next section.

1.2 Nanolithography

Nanolithography is the field that developed in order to obtain patterns with increasingly small dimensions and to face the challenge of integrated-circuit miniaturisation. Among these techniques, photolithography is one of the most standard ones[5]. The procedure is illustrated in figure 1.1. A mask is used to project a patterned beam of light onto a sample consisting of the end material, such as a semiconductor thin film. The film is covered with a material (resist) which changes its solubility as a consequence of the light exposure. The exposed or un-exposed parts of the resist are then removed chemically, in a step called *development*. The result is that the end material is partially covered by the resist in a way that mimics the exposure pattern. The last step is to remove the portions of the material which are no longer protected by the resist via etching or deposit new portions of material, and afterwards, remove the resist itself (*lift-off*).
The theoretical limit of the dimensions that can be obtained with photolithographic techniques is given by the Rayleigh criterion which poses a lower limit to the diameter (D) of a focused radiation source due to diffraction (diffraction-limit)[6]:

$$D = \frac{\lambda}{2n\sin(\theta)} \tag{1.1}$$

where λ is the wavelength of the radiation source, n is the refractive index of the medium in which light is travelling and θ is the half-angle of the light cone focused by the exposure optics. The quantity $n\sin(\theta)$ is often referred to as *numerical aperture* NA, which is used

to characterize the resolution of optical systems via their maximum focusing capability. Equation 1.1 shows that, in principle, exposing the samples to short-wavelength-radiation allows to obtain the smallest feature. For this reason, ultra-violet light is generally used in nanolithography [7,8?].

Currently, nanolithographic techniques allow to obtain patterns with features on the or-

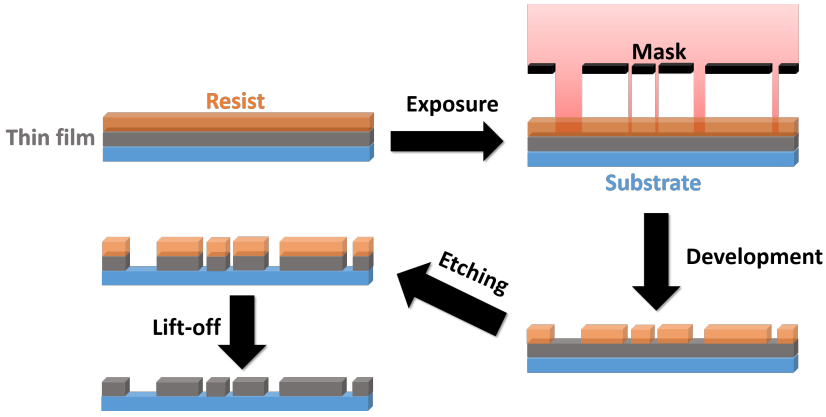

Figure 1.1: Schematics of the steps used to obtain a patterned conductive structure for integrated circuits via photolithography.

der of 5 nm [9]. At this scale the electronic properties of the materials might diverge from the bulk ones. This, together with the requirement of light-induced damage resistance, which enables the avoidance of damage in the fabrication process, and chemical stability, which is beneficial for the long lifetime of the end product, drives a continuous search for suitable materials. In parallel, improvements in processing techniques that increase the processing speed and reduce costs is also a goal of research in this field. A material possessing some of the aforementioned characteristics, raising interest, is ruthenium. In the next section some of its key features are presented.

1.3 Ruthenium

Ruthenium (Ru) is a transition metal with atomic number 44 belonging to group 8 of the periodic table. Similar to other elements in the platinum group, it is chemically relatively unreactive. It has applications in EUV optics for nanolithography [10,11].

Ruthenium has a high melting point of 2583 K. It also has a low electrical resistivity of 7.1 $n\Omega \cdot m$ [12], while ruthenium oxide (RuO_2) has a resistivity of 760 $n\Omega \cdot m$ [13]. Both these values are suitable for applications as conductive material in the semiconductor industry

since, on the nanoscale, Ru appears to have a higher electrical conductivity than Cu, presumably due the smaller grain size. Ruthenium, however, has not been studied as well as many other metals. If Ru is going to be used in future semiconductor devices, it becomes important to know what the effects are of exposing the material to high laser fluences, such as those used in metrology and for wafer alignment. Ru may have other applications as well. Ruthenium-based technology is being developed, for instance, to fabricate electrode materials in electrochemical supercapacitors for energy storage [14,15].
The great interest in the potential applications of ruthenium thus has led to an increased focus of research to expand knowledge on this material and its compounds. The research ranges from the study of ruthenium's magnetic properties [16], the mechanisms of laser-induced damage [17,18] to the oxidation dynamics under different conditions [19].
In the next section, terahertz radiation is introduced. Terahertz emission experiments are indeed a potential tool for the non-invasive study of materials such as ruthenium and could contribute to providing insight into the properties of this material.

1.4 Terahertz emission

Terahertz radiation (THz) is defined as electromagnetic radiation with a frequency between 0.1 THz and 10 THz, corresponding to a wavelength between 30 μm and 3 mm. This range of the electromagnetic spectrum is located between the infrared and the microwaves. In the last 30 years, the progress in the capability to generate and detect this radiation allowed the creation of a whole new field of research spanning from the development of novel sources [20,21] to THz-spectroscopy and imaging [22,23,24].
In particular, the possibility to detect the time-dependent *electric field* of THz radiation provides information on the phase of the radiation, which is lost when measuring the intensity with other spectroscopic techniques, such as visible or infrared spectroscopy. This allows to directly measure the complex refractive index or the complex conductivity of a material without the need to make any assumption. Assumptions need to be made, for instance, when using the Kramers-Kronig relations [25]. These relations allow to calculate the imaginary part of the refractive index once the real part is measured, or vice versa. However, in this calculation it is necessary to extrapolate the frequency-dependence of the refractive index outside of the measurement frequency-interval. The phase information contained in the measurements of the THz electric-field allows to circumvent this problem.
Understanding the processes resulting in the generation of THz radiation is also an active field of research. *Optical rectification*, for instance, is one of the standard generation

mechanisms in which a sub-picosecond near-infrared laser pulse gives rise to THz emission from non-linear optical crystals such as ZnTe [26]. This is a second-order non-linear optical process in which the THz pulse is generated as a result of difference frequency mixing occurring between the frequencies contained in the spectrum of the near-infrared pulse itself. Figure 1.2 shows the THz electric field emitted by a ZnTe crystal by optical rectification.*

The *Photo-Dember effect* is also an established THz generation mechanism. In this, a sub-

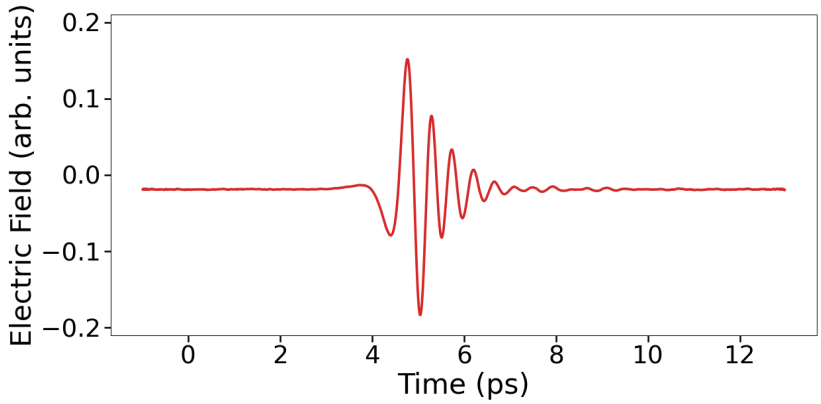

Figure 1.2: A THz electric-field emitted by optical rectification from a ZnTe crystal.

picosecond laser pulse is absorbed by a semiconductor such as GaAs or InAs [27]. Absorption results in the photoexcitation of electron-hole pairs. The concentration of electron-hole pairs changes when moving away from the semiconductor surface. In addition, electrons generally have a higher mobility than holes. These two factors, the gradient in electron-hole concentration and the difference in mobility between the electrons and holes, results in a transient dipole which is responsible for emission of THz radiation. A review of THz generation mechanisms can be found elsewhere [20,28].

In general, THz emission from non-metallic or ferromagnetic materials is a well understood topic. A different situation applies to non-ferromagnetic metals for which, in some cases, extracting reliable conclusions is difficult. This is sometimes partially due to an incomplete determination of the (surface) state of the sample. An example is the case of copper which showed an exponential dependence of the THz-emission energy on the near-infrared pump energy [29]. When in contact with air, copper forms a layer of cuprous oxide (Cu_2O). Later, it was shown that the oxide forms a Schottky contact with the copper and that this is the dominant THz emission mechanism, at least at relatively low optical pow-

*More details about the experimental methods for generating and detecting the THz electric field are given in chapter 2, section 2.2.

ers [30].

1

A Schottky contact can form when a metal and a semiconductor with different Fermi energies are in direct contact. The contact causes the Fermi levels of the two materials to equalize, resulting in electron migration from the material with the higher Fermi energy to the material with the lower one. This results in a region in the semiconductor depleted of free carriers, called the *depletion region*. This charge migration, in turn, results in the creation of an electric field in this region (*depletion field*), as shown in figure 1.3. Illumination with a femtosecond laser pulse results in the photoexcitation of charges in the depletion region which are subsequently accelerated by the depletion field. This charge acceleration is responsible for the emission of a terahertz pulse and, as discussed in chapter 3, it is one of the candidates to explain the THz generation mechanism in ruthenium.

A similar mechanism was observed for THz emission from silver. Silver reacts with traces

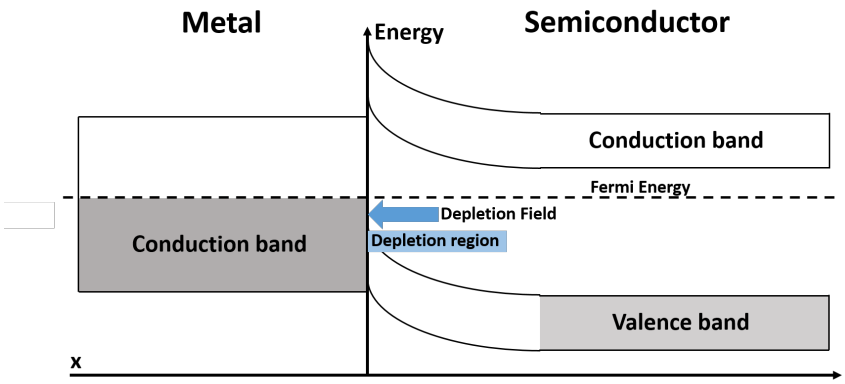

Figure 1.3: Schematics of a Schottky contact. On the left a metal is in contact with a material with an initially higer Fermi energy (such as a semiconductor). This results in charge migration from the metal, giving rise to an electric field in the semiconductor.

of H_2S molecules present in air and forms a layer of semiconducting Ag_2S. The two materials, Ag and Ag_2S, form a Schottky barrier which enhances the emission of THz radiation [30].

These examples show that proper determination of the state of the sample surface is crucial for the interpretation of the results of THz emission experiments. On the other hand, they also suggest that THz emission can be used as a probe for material characterization.

1.5 Patterning of ruthenium via laser-induced oxidation

As was explained in section 1.2, photolithography is based on a change in solubility of a resist, as a result of exposure to electromagnetic radiation. In our experiments to study the emission of THz radiation from Ru, we discovered that above a certain fluence, the laser oxidized the Ru surface. We found that this coincided with a change in solubility in NaClO between the regions exposed to laser light and the un-exposed regions of the samples. While ruthenium can be dissolved in a solution of NaClO in water, resulting in a complete removal from the substrate, ruthenium oxide RuO_2 is not dissolved. If the RuO_2 layer is thick enough, it can prevent the dissolution of the underlying Ru, acting as a protective layer. By tuning the exposure parameters it is therefore possible to use this method to obtain patterns of Ru with a thin oxide layer on top. This method is summarized in figure 1.4, showing that fewer processing steps are required with respect to conventional lithographic techniques described in section 1.2, to pattern Ru.

This method was tested by producing near-circular Ru/RuO_2 islands, providing a proof

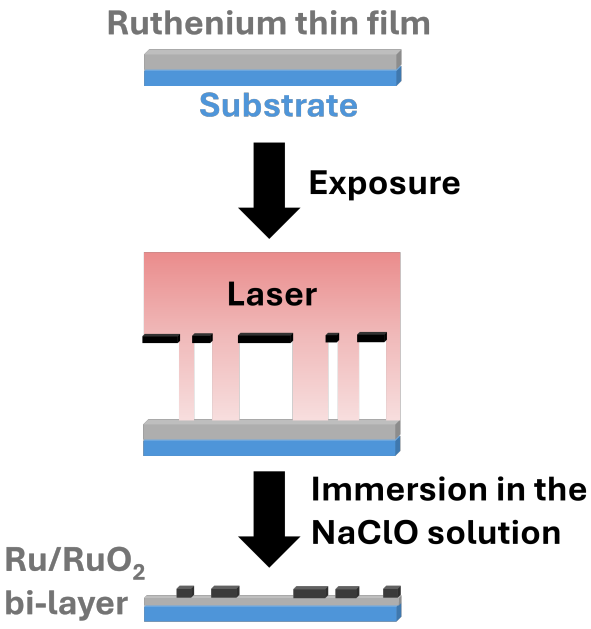

Figure 1.4: Schematics of the steps that would be required to obtain more complicated Ru/RuO_2 patterns based on laser-induced oxidation of a ruthenium thin film

of principle for applications with more complex patterns, similar to what is shown in figure 1.4. Interestingly, we found that the technique also allowed us to create Ru features with

sizes even below the diffraction limit. More details on the method are presented in chapter 2, section 2.3.1.

1.6 Thesis outline

The outline of this thesis is as follows: The next chapter contains the background necessary for the interpretation of the results presented in this thesis. Section 2.1 describes sample fabrication and the techniques that were used for sample characterisation and diagnostics. Section 2.2 describes the basic concepts of research on THz radiation and explains in detail the components of a THz generation and detection setup. Section 2.3 describes in detail the method used for creating the Ru/RuO_2 patterns. Section 2.4 describes the calculations of heat transport in Ru thin films. These calculations are used to gain insight into the laser-induced oxidation process of Ru.

Chapter 3 presents the results of THz emission experiments on Ru thin films. Here, the correlation between THz-emission-strength and oxidation is demonstrated. A dependence of the polarization direction is observed both on the degree of oxidation of the sample and, surprisingly, on the substrate material. In addition, a preferential direction of the THz-polarization is observed, highlighting an anisotropy in the samples. The source of this anisotropy is investigated using two-dimensional x-ray diffraction and atomic force microscopy but, to this day, it remains unknown. This suggests that THz emission could be an extremely sensitive tool to detect features which elude other material characterization techniques.

Chapter 4 introduces the method to obtain Ru/RuO_2 patterns by direct illumination of the Ru films, without the need for a photoresist. A proof of principle experiment is shown in which nearly-circular Ru/RuO_2 islands are created. Two different laser sources are used for exposure, a 5.2 MHz repetition rate laser, focused to a minimum diameter of 8 μm, and a 200 kHz repetition rate laser, focused to a 2 μm diameter spot. The effect of in-plane heat transport on the island formation is more evident when exposure is performed with the high-repetition-rate laser, probably because the short interval between the arrival of each laser pulse results in more pronounced heat-accumulation and in-plane transport. This mechanism is less visible when using the low-repetition-rate laser. In addition, in this chapter, we demonstrate that it is possible to obtain Ru/RuO_2 islands with a diameter as small as 500 nm, which is four times smaller that the diffraction limit of the optical system used for the laser exposure.

Chapter 5 provides additional insight on the Ru patterning method introduced in chapter

4. The effect of the Ru film thickness on the island-formation threshold fluence is tested. It is demonstrated that the threshold fluence for island formation can be determined a priori as long as the Ru film can be considered homogeneously heated by the exposure-laser pulses. The role of the substrates is also probed by producing Ru/RuO_2 islands on Ru samples deposited on three different substrates: glass, sapphire and silicon. The island-formation threshold fluence depends weakly on the substrate material. This is explained in terms of the differences in the interfacial thermal conductances (ITC) between the three substrates. After laser exposure, heat diffusion into the substrate is limited by a finite ITC, resulting in a similar temporal decay of the surface temperature of the Ru for all the substrates. In addition, the role of the exposure beam diameter is tested by comparing the island-formation threshold fluence extracted using a 0.8 μm exposure beam diameter with the one extracted using a 2 μm beam diameter. These experimental results are combined with heat diffusion calculations. This proves that in-plane heat diffusion has a stronger effect when using a sub-micron exposure beam diameter, compared to the 2 μm one. In principle, a smaller exposure beam diameter could be expected to allow to obtain patterns with smaller features. However, the observed in-plane heat diffusion could represent the limiting factor determining the size of the smallest features that can be obtained.

2 Background

This chapter is aimed at providing an overview of the techniques and of the basic concepts necessary to interpret the results presented in chapters 3, 4 and 5. Section 2.1 focuses on the sample preparation, starting from how the substrates are cleaned before the Ru films are deposited through magnetron sputtering, which is described after that. The methods used for inspecting the samples are subsequently explained.
Section 2.2 focuses on some aspects of terahertz electromagnetic pulses generation and detection. It starts by illustrating the main challenges encountered in these measurements. After that, the terahertz generation and detection setup is explained. The sections on electro-optic detection and lock-in amplifier (sections 2.2.2 and 2.2.3) clarify in detail how the terahertz pulses are detected. This lays the groundwork for chapter 3, which present the results of terahertz emission experiments on Ru.
Section 2.3 explains the method for producing conductive Ru/RuO_2 patterns based on laser exposure followed by Ru removal by a NaClO solution. These sections provide an introduction for the results presented in chapters 4 and 5.

2.1 Sample fabrication and characterisation

This section provides the details of the preparation of the samples used for all the results presented in this thesis. It starts by explaining how the substrates are cleaned to remove

potential contaminants.
The Ru thin films were deposited via magnetron sputtering, a standard technique described in section 2.1.2. The sections about sample preparations are followed by those about sample diagnostics (from section 2.1.3 to 2.1.7), concerning x-ray photoelectron spectroscopy, x-ray diffraction, atomic force microscopy, scanning electron microscopy and energy-dispersive x-ray spectroscopy.

2.1.1 Substrates and chemical cleaning

For the experiments reported in this thesis, glass, CaF_2, silicon and sapphire were used as substrate materials.
To prepare and clean the substrates, the following procedure was used. They were first kept in an ultra-sonic water bath for ten minutes. After that, they were kept in a base-piranha solution for 15 minutes at a temperature of 75 ° C. This solution consists of 50 ml of water, 10 ml of ammonia (NH_4OH) and 10 ml of hydrogen peroxide (H_2O_2). The substrates were then rinsed in isopropanol and dried.
Sapphire is a birefringent material. For this reason, commercially available sapphire substrates cut along the C-plane were used, which avoids birefringence for normally-incident light.
The CaF_2 substrates were only rinsed in isopropanol as they could dissolve in the base piranha-solution.

2.1.2 Magnetron sputtering

Magnetron sputtering is a standard technique used for depositing layers of metals with sub-micrometer thickness [31]. In the following the technique is described, providing some parameters used for obtaining the Ru films.
To perform magnetron sputtering, the substrates are loaded into a vacuum chamber, with a pressure of around 10^{-7} mbar. The chamber is then filled with an Ar^+ plasma at a pressure of 10^{-2} mbar. The target material is kept at a negative bias with respect to the substrates, which accelerates the positive Ar^+-ions towards it. The ions hit the target with a high energy, causing the ejection of atoms of the target material. The atoms then land on the substrate, resulting in the growth of the film.

2.1.3 X-ray photoelectron spectroscopy

X-ray photoelectron spectroscopy (XPS) is a widely-used technique for the chemical characterisation of the surface of a sample. First, the principles underlying the measurements are described, and then some basic experimental details are provided. Additional information can be found elsewhere[32].

In XPS, an x-ray source is directed towards the sample, causing emission of core-shell electrons via the photoelectric effect. Electrons with a binding energy (BE) lower than the energy of the x-ray photons ($h\nu$) can be emitted. The electrons emitted by the sample are collected and their kinetic energy (KE) is measured. From this quantity, it is possible to extract the binding energy of the electrons:

$$BE = h\nu - KE - \varphi \tag{2.1}$$

φ is the work function, defined as the minimum energy required to move an electron from a material's surface to the vacuum level. In the context of an XPS spectrometer, the work function refers to the energy needed for an electron to overcome the spectrometer's surface potential barrier and enter the analyzer. This is a known quantity, allowing for corrections to the measured kinetic energy to accurately determine the electron binding energy. Notably, the sample's work function does not need to be known because the sample and the spectrometer are electrically connected, aligning their Fermi levels.

An XPS spectrum generally consists of a series of intensity (usually in electron counts/second) peaks at various binding energies. Each peak is assigned to an atomic orbital by comparing its binding energy to the known value available in the literature.

Shifts in the binding energy of the electrons in an atom occur in response to different chemical bonding states. For this reason, XPS allows to identify the binding states of atoms from the presence of shifted electronic peaks. For instance, in chapter 3 section 3.3.3 the spectra of Ru are shown. The binding energy of the electron in the $3d_{5/2}$ orbital of Ru is 279.8 eV. This same electron has a binding energy of 281.7 eV when the Ru atom is bound to two oxygen atoms. In this case, the presence of oxygen is inferred by this shift without directly detecting any electron emitted from this element.

Figure 2.1 shows a simplified depiction of an XPS spectrometer. The whole setup is kept in an ultra-high vacuum, at pressures around 10^{-9} mbar. This is necessary to avoid scattering of electrons by air molecules and, also, to keep contaminants away from the surface of the sample. For XPS, x-rays are generated by accelerating electrons towards an x-ray anode source. When hit by the electrons, the anode source emits the x-rays. Different sources

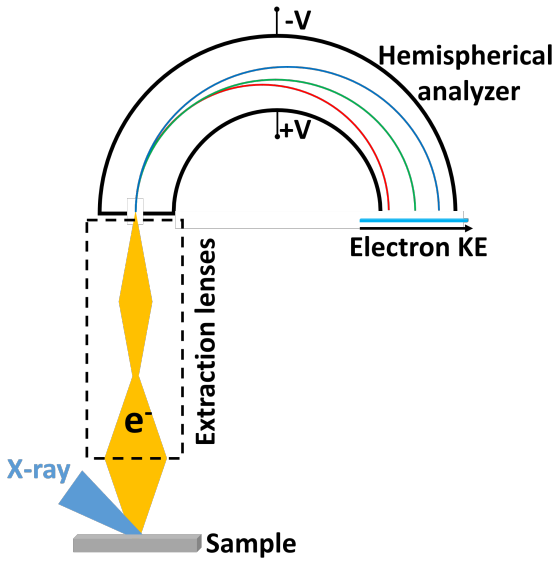

Figure 2.1: Schematic of XPS apparatus. The sample is illuminated by an x-ray beam (light blue) which causes the emission of electrons from the core shells of the atoms. The electrons are then collected and directed towards the entrance of the hemispherical analyzer by a set of electron lenses. The walls of the hemispherical analyzer are kept at a voltage causing the electrons to follow semi-circular orbits with a radius proportional to their kinetic energy. At the end of the hemispherical analyzer, a spatially sensitive detector allows to extract the electron kinetic energies from a map of intensities versus position.

are commercially available, emitting X-rays with different energies and linewidths. For the experiments reported in this thesis, an alluminum Kα source was used. It emits x-rays with an energy of 1486.6 eV (0.834 nm wavelength). The X-rays are directed towards the sample, resulting in the photoemission of electrons (yellow in figure 2.1). The sample should be electrically connected to the spectroscope at a well defined voltage because emission of electron results in charging and, in turn, in shifting of the spectra. For this reason, measurements on non-conducting samples require additional precautions, such as the use of charge neutralizers.

A series of electron lenses (extraction lenses) determine the acceptance angle for the electrons emitted by the sample and affect the energy resolution of the spectrometer by user-defined settings. The extraction lenses focus the electrons to the entrance slit of the *hemispherical analyzer*. This element allows to measure the electron kinetic energy. It consists of two concentric conducting hemispheres with different radii (see figure 2.1). The outer hemisphere is kept at a negative voltage -V with respect to the inner one. The electrons will travel in the analyzer describing semi-circular orbits. The radius of the orbit is directly

proportional to the electron kinetic energy. A detector is placed at the end of the hemispherical analyzer, providing a spatial map of kinetic energies. The intensity of the signal depends on the number of electrons hitting the detector.

2.1.4 1D and 2D X-ray diffraction

X-ray diffraction (XRD) is a standard technique used to determine the crystal structure of materials. The underlying principle of this technique is the diffraction of electromagnetic radiation by a periodic structure. A simplified description is given in the following; a more complete description can be found elsewhere [33].

When a coherent light source is incident on a structure with periodic features with dimensions on the order of its wavelength, diffraction occurs. X-rays have a wavelength on the scale of 0.1 nm, which is on the same scale as the typical spacing between crystal lattice planes. Figure 2.2 shows two rows of atoms representing two crystal planes, with a spacing d between them. An x-ray is incident on the surface at an angle θ. The x-rays interact elastically with the electrons of the atoms, namely in that they are absorbed and re-emitted in all directions. Only the radiation emitted at specific angles interact constructively. These angles are those determined by Bragg's law [6]:

$$\sin\theta = \frac{m\lambda}{2d} \tag{2.2}$$

where m is an integer representing the diffraction order, d is the lattice spacing and λ is the wavelength of the x-rays. If the x-ray interact with a large number of planes such as those sketched in figure 2.2, the radiation re-emitted at angles different than the ones obeying equation 2.2 cancels out and intensity peaks arise at the angles obeying Bragg's law. This way, by varying the angle of incidence of the x-rays, together with the angle of detection, the θ-dependent diffraction pattern is measured. From this, it is possible to extract the lattice spacing d and determine the sample crystal structure. In this case, a point detector is used.

Monocrystalline samples diffract the x-rays towards discrete directions, determined by the geometry of the crystal planes (figure 2.3, left). Samples are often polycrystalline, meaning that they consist of a mixture of domains (crystallites) in which the crystal planes point at random directions. When the region illuminated by the x-rays contains a high number of randomly oriented planes, the diffracted x-rays propagate along the surface of cones (diffraction cones, figure 2.3). Each cone corresponds to a given family of crystal planes. The angles of the vertices of the cones correspond to the diffraction angle θ, determined

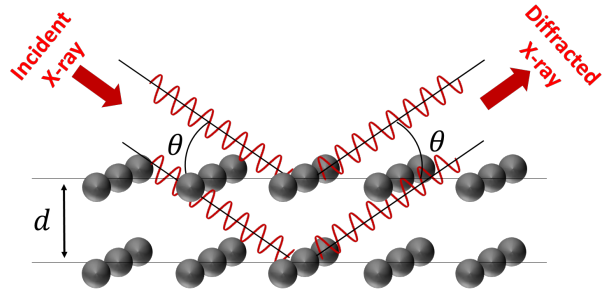

Figure 2.2: Schematic of the interaction between an incident x-ray beam and the ordered array of atoms in a simple crystal. The incident x-ray is reflected from the atoms. Only the beams reflected at an angle θ obeying Bragg's law (equation 2.2) interact constructively, resulting in a diffraction peak.

by applying Bragg's equation to each crystal plane present in the sample. In this case, the diffraction pattern is recorded via a 2D detector and consists of a series of concentric rings, given by the intersection of the detector surface and the diffraction cones. If the crystal planes are oriented randomly with no preferential orientation, the rings will have a uniform intensity. Otherwise, the intensity will not be distributed along the rings and, in the extreme case in which a crystal plane is present in the sample with only one particular orientation, single spots can appear in the diffraction pattern.

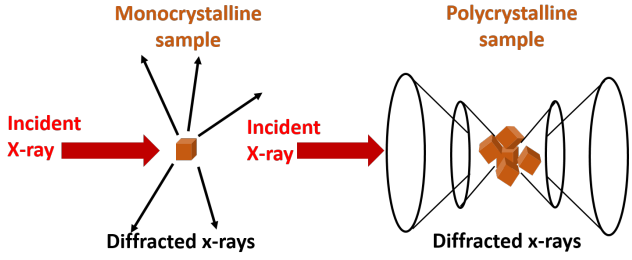

Figure 2.3: Qualitative depiction of the difference of the diffraction from a monocrystalline sample (left) and from a polycrystalline sample with random, uniformly distributed crystal orientations (right). The diffraction pattern from the polycrystalline sample consists of a series of concentric rings.

In chapter 3, this technique is used exactly to test the presence of preferential orientations of the crystallites of the Ru samples.

2.1.5 Atomic force microscopy

An atomic force microscope (AFM) is a device that allows to image the morphology of samples with a resolution on the order of a few nanometers [34].
The main component of an AFM is a cantilever with a tip at its end. The tip has a dimension of approximately 8-12 nm at its end. A laser hits the back of the cantilever. The cantilever is highly reflective so that the laser is reflected and directed towards a quadrant photodiode which records the position of the incident laser. In *contact-mode*-AFM, the tip is brought so close to the sample surface that interatomic interactions such as van der Waals forces act between the two. A raster scan of the surface is performed and changes in the surface morphology result in deflections of the cantilever, which translate into deflections of the reflected laser beam. These are recorded by the quadrant photodiode.
An alternative method to perform AFM is *tapping-mode*. In this case, the cantilever+tip

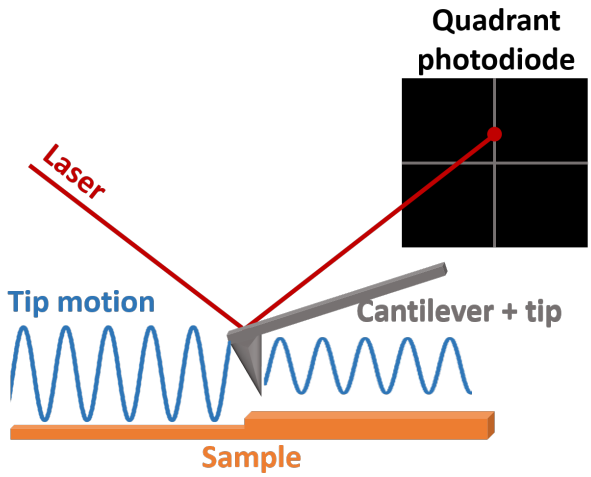

Figure 2.4: Schematic representation of the working principle of tapping-mode AFM. The cantilever oscillates at its resonance frequency with a constant amplitude. Changes in the morphology of the sample surface induce changes in the amplitude and phase of the oscillation of the cantilever. These changes are recorded and allow to image the surface and obtain information on its mechanical properties.

system oscillates at its resonance frequency with a user-defined amplitude (generally on the order of tens of nanometers), as depicted in figure 2.4. This way, the tip is intermittently in contact with the sample surface, unlike in contact mode where the contact is more or less continuous. This has the advantage of reducing lateral forces that occur due to drag during the scanning and, given the short time in which the tip is in contact with the sample, avoid damaging of soft specimens. Changes in the sample morphology induce changes in

the amplitude of the oscillation of the cantilever, which are recorded in the quadrant photodiode. A feedback loop rapidly restores the amplitude to the user-defined value.

In addition to the morphology, tapping mode AFM provides information on the sample mechanical properties. These changes result in phase shifts in the oscillation of the cantilever. Both phase and amplitude changes are recorded simultaneously, showing how tapping-mode AFM allows for a detailed characterisation of the sample in relative short measurement times.

Tapping-mode AFM was used to inspect Ru surfaces in chapter 3.

2.1.6 Scanning electron microscopy

Scanning electron microscopy (SEM) is an imaging technique which uses an electron beam to produce images. The use of electrons allows to reach a higher resolution compared to photons, down to 1 nm [35]. For the images shown in this thesis, however, the SEM reached a resolution of around 10 nm. Electrons allow to reach higher resolutions than photons because they have a shorter de Broglie's wavelength. The de Broglie's wavelength of a particle with mass is:

$$\lambda = \frac{h}{p} \tag{2.3}$$

Where h is Plank's constant and p the modulus of the particle's momentum. The momentum ($p = mv$, where m is mass and v the modulus of the velocity) of an electron accelerated by a voltage V can be obtained from its kinetic energy:

$$eV = \frac{1}{2} m_e v^2 \tag{2.4}$$

where m_e is the mass of the electron. Using equation 2.4 in 2.3, we obtain:

$$\lambda = \frac{h}{\sqrt{2 m_e V}} \tag{2.5}$$

The images presented in this thesis were obtained by using an accelerating voltage $V = 5$ kV, resulting in an electron de Broglie's wavelength of 17.3 pm. Photons at this wavelength are hard x-rays or γ rays, which are not as easy to produce and manipulate for imaging purpose compared to a 5 kV electron beam.

The short wavelength of electrons results in a smaller diffraction limit, which allows to focus the electron beam more tightly than a beam of light. This results in a higher spatial resolution achievable by means of electrons.

In a SEM an electron beam (*primary electrons*) is focused onto the sample surface. The incident electron beam causes emission of various forms of electrons, such as *secondary electrons*, reflected/backscattered electrons, and Auger electrons, but also electromagnetic radiation. The microscope collects the secondary electrons, which are those emitted by the sample atoms in the vicinity of the surface. This is because the secondary electrons are emitted with a relatively low energy of about 50 eV, which limits their mean free path in the solid. Raster scanning by means of the primary electron beam of an area of the sample makes it possible to obtain an image of the sample surface. It should be pointed out that, although the surface morphology plays a role in the result, the contrast in SEM images is ultimately determined by the electronic properties of the sample.
Since electrons are used to image, performing SEM results in sample charging. For this reason, similar to XPS (section 2.1.3) the technique requires a grounded conductive sample to avoid this.
Figure 2.5 is the SEM image of the surface of an 8 nm thick Ru film deposited on glass, showing that Ru thin films typically have a granular structure, with grain sizes of a few nanometers.

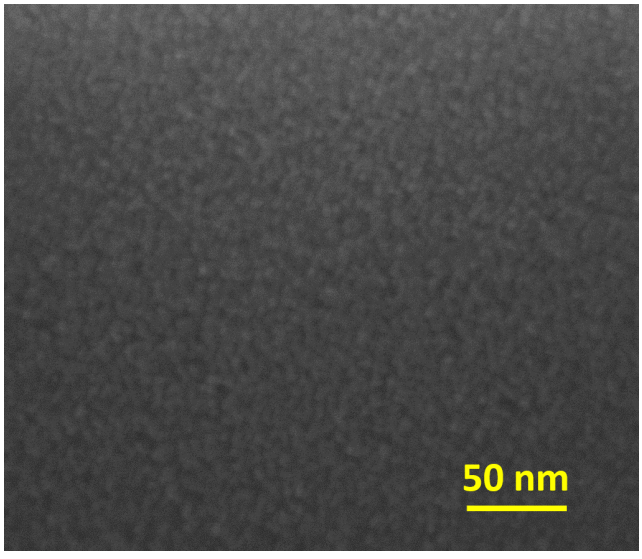

Figure 2.5: SEM image of the surface of an 8 nm thick Ru film.

SEM images were used to inspect and measure the size of the Ru/RuO_2 islands mentioned in the previous paragraph.
A scanning electron microscope equipped with an x-ray detector allows for the elemen-

tal characterization of the sample through a technique called *energy-dispersive x-ray spectroscopy*. This technique is described in the next section.

2.1.7 Energy-dispersive x-ray spectroscopy

Energy-dispersive x-ray spectroscopy (EDX) allows to obtain spatial maps of the elemental composition of samples [36]. As already mentioned in the previous section, an EDX system can be integrated in a SEM.

When the electron beam hits the sample, its energy can be transferred to an electron in the inner orbitals of the sample atoms, resulting in its ejection. This leaves an electron vacancy in the corresponding energy level of the ionized atom. An electron from the outer shell of the atom might fill this vacancy by losing energy in the form of x-rays. The energy of these emitted x-rays corresponds to the energy difference between the energy of the orbital filled by the outer electron and the one from which it was ejected. Since the energies of the atomic orbitals are characteristic for each element, by measuring the energies of the x-rays emitted by the sample, it is possible to infer the elemental composition of the surface.

2.2 THz emission from Ru thin films

In this section the basic concepts underlying experiments on femtosecond laser-induced generation of coherent terahertz radiation are introduced. In particular, justification of the experimental choices that were made, based on the challenges that these kind of experiments present is provided.

The main difficulty encountered when attempting to measure THz pulses from Ru thin films is caused by the weakness of the signal. To give a feeling for this, in figure 2.6 the time-dependent THz electric field emitted by a 0.5 mm (110)-oriented ZnTe crystal (black), a standard THz emitter [37], is compared with the one emitted by an 8 nm thick Ru film deposited on glass (red, scaled by a factor of approximately 1000).*

The signals consist of a quasi single-cycle oscillation, located approximately at 0 ps delay. The most obvious difference between the two traces is the much lower signal-to-noise ratio of the THz pulse emitted from the Ru sample. The THz radiation emitted by Ru (and, in general, by non-ferromagnetic metals) is indeed very weak compared to other emitters. The difference between the two emitters is even more striking considering that the black

*The traces are plotted as a function of the time delay between the near-infrared femtosecond laser pulse inducing THz emission and the detection pulse.

curve was obtained by averaging over 10 traces, while the red one was averaged over 4 000 traces. The magnitude of the THz radiation emitted from Ru should suggest that a fully optimized setup is necessary to measure it.

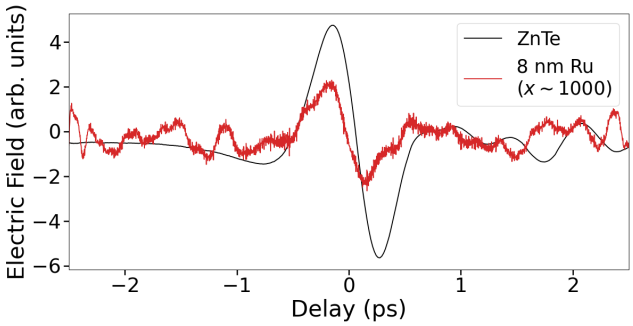

Figure 2.6: Comparison between the time-dependent THz electric field emitted by a standard, relatively strong emitter (2 mm thick ZnTe crystal) and an 8 nm thick Ru film. The THz pulse emitted by the Ru film was magnified by a factor 1000.

The THz radiation emitted from Ru is *coherent*, in the sense that every pulse has a fixed, reproducible phase-relation with the generating laser pulses impinging on the sample. For this reason, we used electro-optic detection as the technique for detecting the THz electric field. In addition, this technique is a time-gated one, meaning that the setup is only sensitive during the short time interval corresponding to the propagation time of the probe-pulse through the detection crystal, which allows to drastically reduce thermal noise. In section 2.2.2 more details of this technique are shown and explained.
To further increase the sensitivity of the THz generation and detection setup, a lock-in amplifier was used, which makes it possible to measure signals at a given bandwidth around a reference frequency, suppressing the noise at other frequencies. The working principle of lock-in detection is described in section 2.2.3.
Before this, in the next section an overview of the THz generation and detection setup is given.

2.2.1 Terahertz generation and detection setup

The setup for generation and detection of coherent THz radiation is depicted in figure 2.7. In the following, each element of the setup is described in order to explain how it operates. The setup uses a 800 nm central wavelength Ti:Sapphire laser oscillator which delivers pulses with a duration of approximately 100 fs with a repetition rate of 5.2 MHz. A beam

splitter (BS) transmits 80% of the laser power towards the pump arm of the setup and reflects 20% of it towards the probe, with which THz light is to be detected. The pump beam is periodically blocked with a frequency of 10 kHz by means of a mechanical chopper consisting of a set of rotating blades. The chopper provides the 10 kHz reference frequency for the lock-in amplifier (see section 2.2.3).

After the chopper, the pump beam is sent to the delay line. It consists of a retro-reflector oscillating over a user-defined distance and frequency, providing a delay between the arrival times of the pump pulses (and, by consequence, the THz pulses) and the probe pulses. To reduce suppression of the higher frequency components in the measured THz electric field by the lock-in amplifier, the oscillation amplitude of the rapid scanner was reduced to about 5 ps, so that the time duration of those components in "lab time" was significantly longer than the integration time constant of the lock-in. This short 5 ps time window is not a limitation for our experiments because most information about the THz generation mechanism is contained in the approximately 1-ps-long main THz peak. For other applications, such as THz time-domain spectroscopy, longer scan ranges are, however, preferable [23].

Exiting the delay line, the beam is weakly focused by means of a lens towards the THz emitting sample. The sample is placed behind the focal point of the lens, where the beam has a diameter of approximately 700 μm. This large diameter is chosen in order to limit the divergence of the generated THz beam (in light-blue in figure 2.7). This might result in losses of the radiation at the edges of the optics collecting it. This optics consists of two off-axis parabolic mirrors.

One parabolic mirror collimates the THz radiation emitted by the sample in the transmission direction. Another parabolic mirror focuses it towards the electro-optic (EO) detection section of the setup. This latter mirror has a hole in its center, allowing for the passage of the probe beam. The probe beam is focused, together with the THz beam, in the EO detection crystal. This is described in more detail in section 2.2.2. Detection of the THz electric field is done by measuring the polarization change that the probe beam undergoes as a consequence of the THz electric field-induced birefringence in the electro-optic crystal.

The change in the probe beam polarization is measured by using a quarter-wave plate in conjunction with a Wollaston prism, splitting the two orthogonal polarization components of the polarization ellipse, and a differential photodetector (DPD, in green in figure 2.7). The latter consists of two photodiodes connected in series and allows to cancel intensity fluctuations common to the two beams arriving at the photodiodes.

The signal from the DPD is then sent to the lock-in amplifier (described in section 2.2.3). The output of the latter is then sent to an analog-to-digital converter and read-out on a PC.

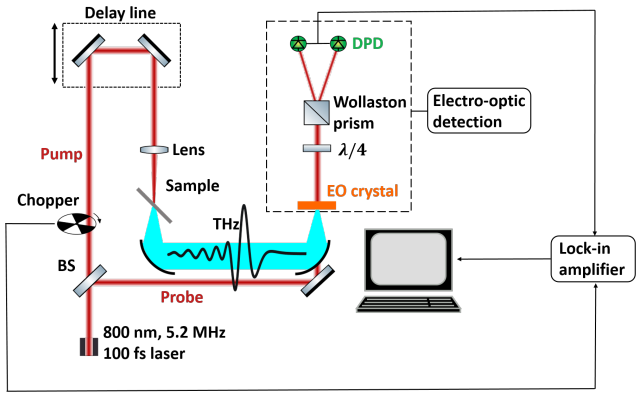

Figure 2.7: Schematic of the THz generation and detection setup. The Ti:Sapphire laser beam is depicted in red. The THz radiation beam is shown in light blue.

2.2.2 Electro-optic detection of terahertz radiation

In this section the working principle of electro-optic (EO) detection is described [38,39,40]. In particular, the goal is to show how this is used to measure the amplitude and the phase of the electric field of a THz pulse.

A schematic depiction of the technique is provided in figure 2.8. The linearly polarized sub-picosecond probe pulse co-propagates with the terahertz wave (black) inside an EO crystal (orange). The probe beam is depicted in red: the envelope of the pulse is represented by the red gaussian curve, the polarization states by the red arrows, and the propagation direction goes from left to right, along the red lines. The THz wave is drawn in black.

When the probe beam is transmitted through the EO crystal without a THz wave, its (linear) polarization is not changed. The optical axis of the quarter-wave plate ($\lambda/4$, black in figure 2.8) is oriented at a 45° angle so that, in this configuration, the probe polarization is transmitted with a circular polarization. The Wollaston prism is a 50:50 polarizing beam splitter which decomposes the incident light into its orthogonal linear components and directs them towards a differential photo-detector. This element provides a ΔI signal corresponding to the difference in intensity of the two polarization components (zero if the components have equal intensity). The setup is therefore *balanced* by setting the orientation of the $\lambda/4$ so that the differential detector measures zero signal when the probe beam is linearly polarized.

The presence of a non-zero THz electric field induces a non-isotropic change in the refractive index of the EO crystal, creating a fast and a slow axis. If the probe beam polarization is oriented such that it has a non-zero component both along the fast and slow axis induced in the EO crystal, a phase difference is introduced between such polarization components. This means that the polarization of the probe beam becomes elliptical. The intensities of the two beams after the Wollaston prism will therefore now be different. The differential photo-detector will measure a signal which is proportional to the amplitude and sign of the THz electric field.

The amount of ellipticity acquired by the probe beam is partially determined by the

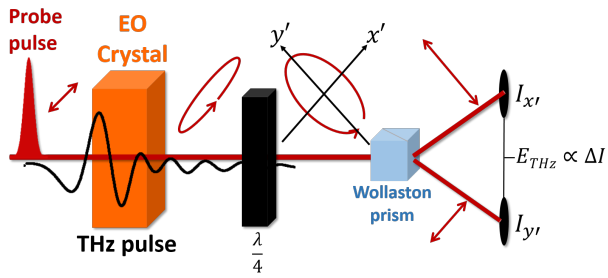

Figure 2.8: Representation of the EO-detection section of the setup. The red lines represent the probe beam, the arrows on top its polarization states.

strength of the electric field of the THz wave, integrated over the duration of the probe pulse. Since the variation of the THz field is much slower than that of an optical/near-infrared wave, the THz electric field can be considered quasi-static. By varying the time delay between the THz wave and the probe pulse, the whole THz waveform is measured with a time resolution partially determined by the duration of the probe pulse.

Since in EO detection the setup is sensitive to THz signals in a time-window corresponding to the duration of probe-pulse, this technique is also known as electro-optic sampling, since the THz signal is "sampled" by the probe pulses. This carries the advantage of drastically reducing thermal noise, making such a technique particularly suitable for the detection of coherent THz pulses.

The above explains how the time-dependent electric field amplitude is recorded by the probe beam. It was mentioned that the amount of ellipticity acquired by the probe beam is partially determined by the strength of the THz electric field. Other factors determining the amount of ellipticity and, therefore, the THz signal strength are:

- the magnitude of the electro-optic coefficient of the EO crystal

- the thickness of the EO crystal
- the relative orientation of the probe beam polarization and the THz polarization with the crystal axes [40]

For the measurements presented in chapter 3 we used a (110)-ZnTe crystal, which has an EO coefficient r_{41} = 4.04 pm/V [41], one of the highest among the crystal commonly used for THz detection. This, in principle, optimizes the sensitivity of our setup to weak THz signals.
The detection sensitivity can also be enhanced by increasing the interaction length between the probe- and the THz pulses. Due to phase-matching, this has the effect of reducing the detection bandwidth [42]. However, in this work, the weakness of the signals requires optimisation of signal amplitude, rather than the bandwidth. For this reason, a relatively thick 2-mm-crystal was chosen for detection. Finally, it is important to point out that EO detection is sensitive to relative changes in the THz polarization direction.
A detailed description of the detection signal as a function of the orientation of the probe-polarization direction and the THz polarization direction with respect to the (001) axis of a (110)-oriented ZnTe crystal is given by Planken *et al.* [40]. Figure 2.9 is a schematic of a (110)-oriented ZnTe crystal. The THz electric field E_{THz} and the probe beam propagate collinearly with wavevectors $\vec{k}_{THz}$ and $\vec{k}_{probe}$ along the (110) crystal axis. The angle between the probe polarization and the (001) crystal axis is α; the angle between the THz polarization and the same axis is β. Then, the intensity difference between the polarization components of the probe beam is:

$$\Delta I(\alpha,\beta) = I_p \frac{\omega n^3 E_{THz} r_{41} L}{2c} (\cos\beta \sin 2\alpha + 2 \sin\beta \cos 2\alpha) \tag{2.6}$$

where:

- I_p is the intensity of the probe beam
- ω is the angular frequency of the probe pulse
- c is the speed of light in vacuum
- L is the length of the EO crystal
- n if the refractive index of ZnTe at the wavelength of the probe beam. Its value at 800 nm is 2.8 [40].

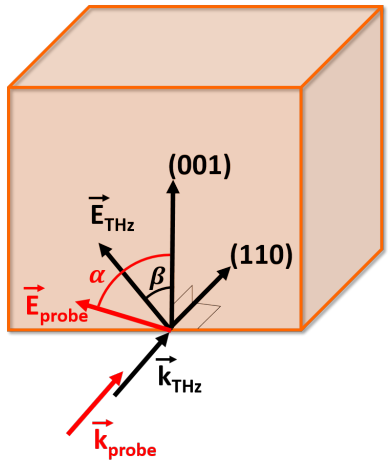

Figure 2.9: Schematic depiction of a ZnTe detection crystal in which the THz pulse co-propagate with the probe pulse. The propagation directions are represented by the wavevectors $\vec{k}_{THz}$ and $\vec{k}_{probe}$, which lie along the (1 1 0) axis (normal incidence). The probe beam is linearly polarized at an angle α with respect to the (0 0 1) crystal axis; the THz electric field is at an angle β with this axis.

Once the EO detection setup is optimized for a given polarization direction, any change in the THz emitter resulting in rotation of the emitted THz polarization will result in a decrease in the amplitude of the detected THz field. This fact will become particularly relevant in chapter 3, section 3.3.4.

2.2.3 Working Principle of a Lock-in Amplifier

As mentioned in section 2.2.1, the output of the differential photodiode is connected to a lock-in amplifier before being digitally converted and read-out by a PC. Here, the basic operating principle of such an instrument is described, showing how it allows to measure signals weaker than the noise level. More details about these devices can be found elsewhere [43,44].

Lock-in amplification detects signals in a user-defined bandwidth around a given frequency (*reference* frequency) over a narrow bandwidth. In this way, noise contributions at frequencies far from the reference frequency can be excluded. It works by adding an amplitude modulation to the laser beam. In our setup, the modulation is provided by the optical chopper: the pump laser is periodically blocked and transmitted by the chopper wheel and, by consequence, the THz signal will have the same periodicity.

The optical chopper is also connected to the lock-in amplifier via its control unit, providing a signal with the same frequency and phase to the lock-in as the modulation(figure 2.7);

this signal is the reference signal. The lock-in uses the reference signal to generate an internal reference by means of a phase-locked-loop.
In order to understand how only signals with a frequency around the reference frequency are detected, let us assume that the input signal (which we want to measure) is a sine wave of the form:

$$Sig = V_{sig}(t)(1 + \sin(\omega_{sig}t + \theta_{sig})) \tag{2.7}$$

where $V_{sig}(t)$ is the time-dependent signal amplitude, ω_{sig} is a modulation frequency and θ_{sig} is its phase; t is time. The internal reference of the lock-in amplifier is of the form:

$$Ref = V_{ref}\sin(\omega_{ref}t + \theta_{ref}) \tag{2.8}$$

The lock-in amplifier multiplies the input signal by the internal reference, which results in an output of the form:

$$\begin{aligned} Output = &\frac{1}{2}V_{ref}V_{sig}(t)[\cos((\omega_{sig} - \omega_{ref})t + \theta_{sig} - \theta_{ref}) + \\ &- \cos((\omega_{sig} + \omega_{ref})t + \theta_{sig} + \theta_{ref})] \end{aligned} \tag{2.9}$$

This output consists of two AC signals with frequencies equal to the sum and difference between ω_{ref} and ω_{sig}. The signal amplitude $V_{sig}(t)$ is also an AC signal but, in order to be properly sampled, it must vary over much longer time scales compared to the reference signal.
The next signal-processing step that occurs in the lock-in amplifier is low-pass filtering, which filters out higher frequency noise signals. This bandwidth goes from DC to a value set by the user through the time constant τ; its inverse $(1/\tau)$ gives the detection bandwidth. From equation 2.9, a quasi-DC signal, corresponding to the slowly-varying $V_{sig}(t)$, can only be present when $\omega_{sig} = \omega_{ref}$. The term oscillating with the angular frequency $\omega_{sig} + \omega_{ref}$ is filtered out this way. The output, at this stage, is therefore:

$$Output(\omega_{sig} = \omega_{ref}) = \frac{1}{2}V_{ref}V_{sig}(t)\cos(\theta_{sig} - \theta_{ref}) \tag{2.10}$$

Equation 2.10 shows that the measurement has a value proportional to the input signal, dependent on the phase difference between the input and the reference signal. This phase difference can be adjusted by the user in order to maximize the output. An amplifier resulting in an output like the one of equation 2.10 is called single-phase-amplifier.
Dual-phase amplifiers allow to eliminate the phase dependence of equation 2.10. These

amplifiers produce two outputs, called *in-phase* (X) and *quadrature* (Y) component. Y is the 90° phase-shifted version of X, namely:

$$\begin{cases} X = \frac{1}{2} V_{ref} V_{sig}(t) \cos(\theta_{sig} - \theta_{ref}) \\ Y = \frac{1}{2} V_{ref} V_{sig}(t) \sin(\theta_{sig} - \theta_{ref}) \end{cases} \tag{2.11}$$

from which the phase-independent (positive-definite) quantity is $R = \sqrt{X^2 + Y^2}$.
Two of the key parameters to adjust when performing lock-in detection are the reference frequency and the time constant. As we have seen, the reference frequency determines the frequency of the signals that the lock-in amplifier will amplify and detect. It is therefore important to chose a reference frequency where noise is low. This is because, together with the signal that one wants to measure, noise present within the detection bandwidth will also be amplified. Typically, the noise spectrum of a Ti:Sapphire laser has a 1/f frequency dependence, therefore high frequencies are preferable. For this reason, a 10 kHz reference frequency was used, the maximum allowed by a mechanical chopper.
As already mentioned, the time constant determines the detection bandwidth of the lock-in amplifier and, therefore, its response time. A too low time constant results in slow response times of the amplifier, which might cause a reduction of the amplitude of the measured signal and smearing out of the signal in time. A high time constant allows for a higher time resolution of the signal but, on the other hand, goes hand in hand with a broad detection bandwidth. This can result in a noise increase.
In the setup (as described in section 2.2.1) a 5 ps pump-probe delay is scanned at a frequency of 10 Hz. Let us estimate the time constant needed to adequately resolve the approximately 1 ps long THz peak. The delay line moves with a speed $V = c \cdot 5$ ps $\cdot 10$ Hz $= 15$ mm/s, c being the speed of light. By imposing a response time approximately 100 times as fast as the 1 ps variation of the THz electric field, we obtain a time constant of $\sim$ 300 μs. This is the value that was used for the measurements reported in this thesis.

2.3 Ruthenium patterning

This section focuses on the details regarding the method for obtaining Ru/RuO_2 patterns which is introduced in chapter 4 and further described in chapter 5. This method simply boils down to exposing a Ru thin film to a pulsed laser and, subsequently, immersing the sample in a NaClO solution. Laser exposure results in the partial oxidation of the Ru film.

The NaClO solution dissolves the un-exposed un-oxidized Ru, leaving on the substrate only the partially oxidized regions. The fact that the method actually results in a Ru/RuO_2 bilayer was demonstrated by performing XPS, as discussed in chapter 4. Shaping the illumination profile in principle allows to produce conductive patterns with the desired shape. As a proof of concept, the method was demonstrated by producing near-circular Ru/RuO_2 islands. This was done by exposing the samples to two different laser sources focused either by means of a lens or a microscope objective. Figure 2.10 is a SEM image of a typical Ru/RuO_2 island obtained using the method described above. The island was obtained by exposing a 50 nm thick Ru film on silicon to the 5.2 MHz repetition rate laser (described in section 4.2 and 5.2). The laser was focused to a spot size of approximately 8 μm. The island has a diameter of approximately 9 μm

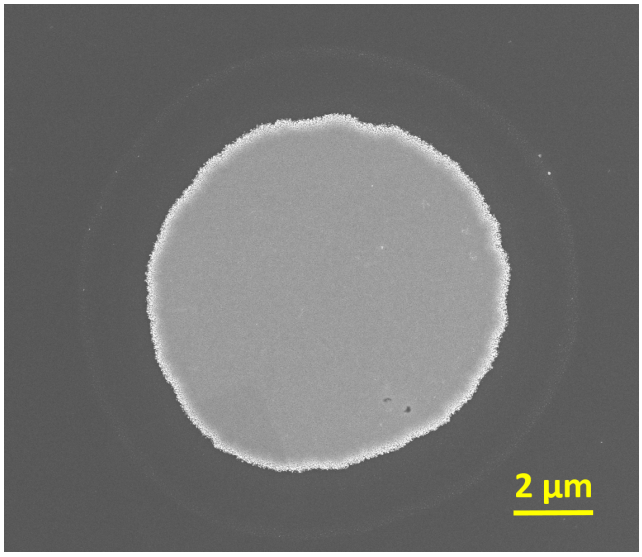

Figure 2.10: Example of a Ru/RuO_2 island obtained using the method described in this thesis. The image was obtained using a SEM.

2.3.1 Ru dissolution in NaClO

Here, the details of Ru removal by sample immersion in the NaClO solution in water are presented.

After exposure, the samples are immersed in a solution of NaClO (Sodium hypochlorite), an alkaline inorganic compound. This causes the dissolution of the un-oxidized Ru. Figure 2.11 shows four photos of an 8 nm thick Ru film deposited on a glass substrate immersed

in the NaClO solution, taken 0 s, 5 s, 10 s and 20 s after the immersion. Two regions of the sample were exposed to the Ti:Sapphire laser described in section 2.2.1, focused to a 1 mm spot. After 5 s, these regions, highlighted by the red ellipse, start to be visible as the surrounding un-exposed Ru starts to dissolve. They become more evident after 10 s and, at 20 s, the un-exposed portion of the glass substrate appears completely transparent. This visual inspection is interpreted as a sign of complete Ru removal.

The immersion time for complete removal of the Ru depends on the film thickness. In

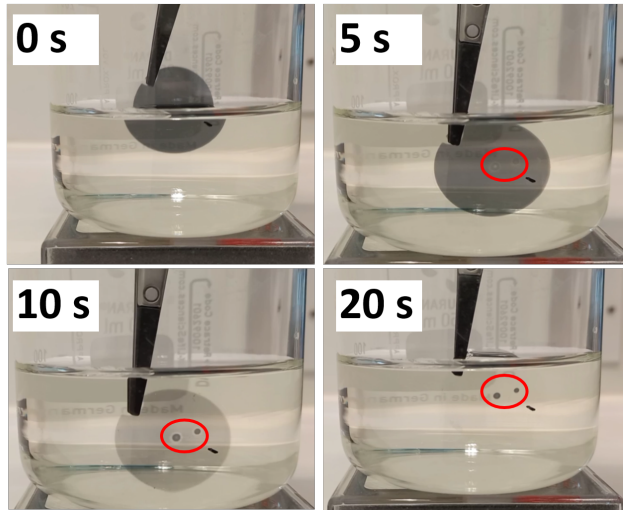

Figure 2.11: Photos obtained after 0 s, 5 s, 10 s and 20 s immersion of an 8 nm thick Ru film on glass in the NaClO solution. After 5 s, the two regions partially oxidized by laser exposure become visible (highlighted by the red ellipse). After 20 s the glass substrate appears clean and only the partially oxidized islands remain on the substrate.

chapters 4 and 5, the method is tested on 8-nm, 20-nm and 50-nm-thick samples. The immersion times for these thicknesses are 90 s, 270 s and 360 s. Although complete Ru removal occurs at even shorter times, it was observed that the remnant Ru/RuO_2 was not affected by the NaClO solution even after approximately 6 hours-long immersion.

After dissolving the Ru, the samples were rinsed using demineralised water. It is important, in this step, to use an abundant stream of water. This is because evaporation of the NaClO was shown to leave traces of crystals similar to those shown in figure 2.12. The figure is an SEM image obtained after dissolving a 50 nm thick Ru layer on silicon. Given the presence of Na and Cl in the solution, these are most likely NaCl crystals. Properly rinsing in water removes the crystals.

The samples were subsequently dried by washing them with isopropyl alcohol and flush-

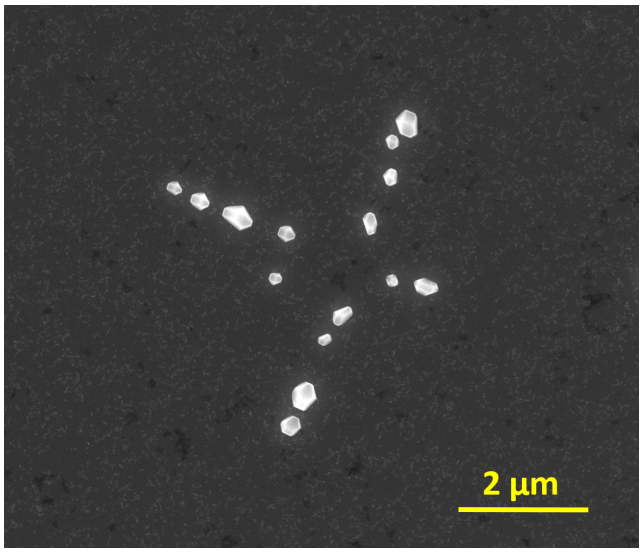

Figure 2.12: Crystals forming on the samples after dissolving the Ru thin film using the NaClO solution as a result of insufficient water rinsing. These crystals are most likely NaCl (rock salt).

ing them with N_2 gas.

2.3.2 Liu analysis

In this section, the so-called Liu analysis is explained. This analysis was first developed by J. M. Liu as a technique to measure the diameter of pulsed Gaussian laser beams and to extract the threshold fluence of laser-induced material modifications such as ablation, crystalline-to-amorphous transitions or, as in the case of this thesis, laser-induced oxidation [45]. In this thesis, in chapters 4 and 5, this method is used to extract the threshold fluence for the formation of the Ru/RuO_2 islands.

In the following it will be demonstrated that, in the absence of in-plane heat diffusion, the area of the laser-induced material modification scales linearly with the natural logarithm of the peak pump fluence F_p of the exposure beam. Following the detailed description provided by E. Abram [46], the intensity profile $I(r,t)$ of a laser pulse with Gaussian spatial and temporal profile is:

$$I(r,t) = I_p\, e^{-4\ln(2)\frac{r^2}{d^2}}\, e^{-4\ln(2)\frac{t^2}{\tau^2}} \tag{2.12}$$

where r and t are respectively the radial and temporal coordinates, τ is the duration of the pulse and d is its diameter, both defined at the FWHM of the intensity profile. I_p is the

peak intensity at the center of the beam. The spatial profile integrated over time is:

$$F(r) = \int_{-\infty}^{+\infty} I(r,t)\,dt = \sqrt{\frac{\pi}{4\ln 2}}\tau I_p\, e^{-4\ln(2)\frac{r^2}{d^2}} = F_p\, e^{-\frac{r^2}{\rho^2}} \tag{2.13}$$

Where F_p is the peak fluence and $\rho = \frac{d}{\sqrt{4\ln 2}}$.
At the perimeter of the laser-induced material modification, at a distance r_0, equation 2.13 is:

$$F_0 = F_p\, e^{-\frac{r_0^2}{\rho^2}} \tag{2.14}$$

This is the threshold fluence at which the process resulting in the material modification occurs. Calculating the natural logarithm on both sides of equation 2.14 and including the area as $A = \pi r_0^2$ we obtain:

$$\ln F_p - \ln F_0 = \frac{A}{\pi\rho^2} \tag{2.15}$$

namely:

$$A = \pi\rho^2(\ln F_p - \ln F_0) \tag{2.16}$$

which shows that the area of the laser-induced material modification of the sample scales linearly with the natural logarithm of the laser peak fluence. This is true as long as the material modification is directly related to the exposure laser spatial profile and no in-plane diffusion process causes the material modification to expand outside of it. In this case, the threshold fluence F_0 can be extracted by plotting A as a function of the exposure peak fluence F_p and extracting the fluence at which $A = 0$.
In chapters 4 and 5, the Liu analysis described above was used to extract the threshold fluence necessary to form a thick enough ruthenium-oxide which allows to prevent dissolution in the NaClO solution. In addition, a non-linear dependence of the area of the Ru/RuO_2 on exposure fluence is used as an indication of in-plane heat transport in the Ru film.

2.4 Heat diffusion in Ru thin films

In section 2.4.3 calculations on the diffusion of heat in a Ru film are presented. The equations were numerically solved to model the temporal evolution of the temperature at the surface of the film. The results presented in chapter 5 are based on these calculations, from which we drew conclusions on the role of in-plane heat diffusion in the formation of the

Ru/RuO_2 islands. In this, we assumed that the partially oxidized region and, therefore, the partially oxidized island forms in the location where the Ru lattice temperature exceeds the temperature threshold necessary for the formation of an oxide which is thick enough to prevent dissolution in the NaClO solution.

As a starting point for the heat diffusion calculations, it was necessary to estimate the energy density of the Ru lattice after the absorption of a laser pulse. This was done by modeling the sample as a three-layer system consisting of air, the Ru film and the substrate. As it will be explained in section 2.4.1, due to the fact that the thickness of the Ru films is on the order of the light penetration depth, it is necessary to take into account the multiple reflections occurring at the interface between the film and the substrate. In similar cases, the optical properties of the substrate influence the amount of light absorbed by the film, from which the energy density can be extracted.

In metals, the energy of a laser pulse is absorbed by the electrons which then transfer the energy to the lattice by the emission of phonons. We assume that both the electron gas and the lattice are internally thermalized, but each at a different temperature. This is described by the *two-temperature model* [47]. This model is illustrated in section 2.4.2. The results of the two-temperature model, consisting of the lattice temperature spatio-temporal profile obtained when the electrons and the lattice approach thermal equilibrium, serve as an input for subsequent calculations of the heat-diffusion using the calculations reported in section 2.4.3.

As a summary, the steps that were followed to compute the temporal evolution of the temperature at the surface of the Ru film are the following:

1. Calculate the energy density deposited in the Ru film by absorption of a laser pulse using the three-layer model (section 2.4.1)

2. Calculate the energy density of the lattice shortly after optical excitation using the two-temperature model (section 2.4.2)

3. Use the lattice temperature distribution obtained via the two-temperature model as the input to calculate the subsequent temporal evolution of the temperature at the surface of the Ru film taking lateral heat diffusion and heat diffusion into the substrate into account (section 2.4.3).

2.4.1 Light absorption in a three-layer system

The absorption of light in a material as a function of the depth z is described by Beer-Lambert's law:

$$I(z,t) = (1-R)I_0(t)e^{-\frac{z}{d_p}} \tag{2.17}$$

where R is the power reflection coefficient quantifying the fraction of reflected light, I_0 is the incident light intensity (therefore at $z = 0$) and d_p is the optical penetration depth. The penetration depth corresponds to the depth at which the intensity of light is decreased to $1/e$ of I_0. Equation 2.17 is only valid if the absorbing layer exceeds the optical penetration depth. If this is not the case, it is necessary to take into account multiple reflections and transmissions inside the material, which occur because the radiation reaching the interface between the material under study (Ru) and the substrate still has significant intensity. The penetration depth for Ru at a wavelength of 800 nm is about 15 nm [48], which is on the order of the thickness of the films used for the results reported in this thesis. For this reason, in this section, light absorption in a three-layer system is described.

A schematic of the model is depicted in figure 2.13. Although the nature of the materials is only taken into consideration at the end of the calculations, making them applicable to various materials, in this case layer 1 represents air, layer 2 the Ru film and layer 3 the substrate. We assume a plane monochromatic electromagnetic wave orthogonally incident on this sample. The electric field (red in the figure) is linearly polarized along the x direction and propagates along z. It is therefore defined as:

$$\vec{E}(z,t) = E_0 e^{i(k_1 z - \omega t)}\hat{x} \tag{2.18}$$

ω is the angular frequency of the radiation; k_1 is the wavevector inside material 1. This quantity depends on the material in which the wave propagates through its dependence on the refractive index: $k_i = \frac{n_i \omega}{c}$, $i = 1, 2, 3$ is the index labeling each layer in our system. The refractive index n and, consequently, the wavevectors k_i are complex numbers.

At each interface between two materials with different refractive indices, the electromagnetic wave is partially reflected and partially transmitted. The reflected waves propagate in the opposite directions with respect to the incident wave and the transmitted one. For instance, within material 1, the continuous incident wave overlaps with the wave reflected from the 1-2 interface (the one between layer 1 and 2); in layer 2, the wave transmitted from layer 1 overlaps with the one reflected from the 2-3 interface, and so on. In each medium, with the exception of layer 3, the electric fields is given by the sum of a wave propagating to

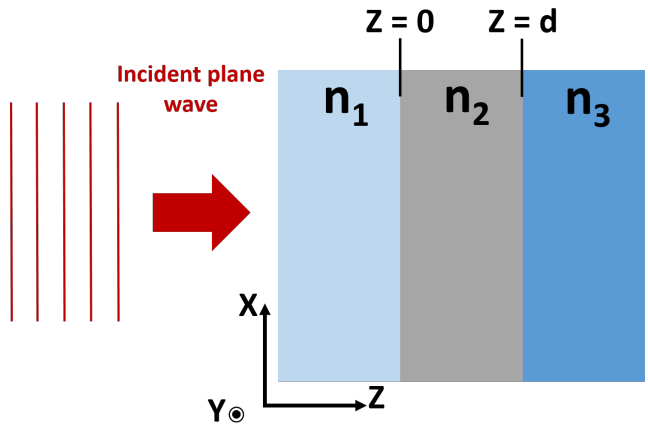

Figure 2.13

the right and a wave propagating to the left. These are the total fields, meaning that they are the sum of all reflections and transmissions in the medium. The exception is medium 3, where the field only propagates to the right. This situation is described by equation 2.19:

$$\vec{E}(z) = E_0 \begin{cases} (e^{ik_1 z} + re^{-ik_1 z})\hat{x} & z \leq 0 \\ (ae^{ik_2 z} + be^{-ik_2 z})\hat{x} & 0 < z \leq d \\ te^{ik_3 (z-d)}\hat{x} & d < z \end{cases} \tag{2.19}$$

where:

- r is the amplitude coefficient describing the field in layer 1, propagating to the left.
- a is the amplitude coefficient describing the field propagating to the right in layer 2
- b is the amplitude coefficient describing the field propagating to the left in layer 2
- t is the transmission coefficient from layer 2 into layer 3

The $z-$ranges were defined assuming that the first layer extends from $-\infty$ to $z = 0$ and has a refractive index n_1. At $z = 0$, the second layer, with refractive index n_2, begins and extends until $z = d$. The third layer spans from $z = d$ to $+\infty$.
Using the boundary condition that no free charges and free currents are present, implies that the component parallel to the surface of both the electric and magnetic fields are con-

tinuous. Using this, we obtain:

$$\begin{cases} 1 + r = a + b \\ ae^{ik_2 d} + be^{-ik_2 d} = t \\ k_1(1 - r) = k_2(a - b) \\ k_2(ae^{ik_2 d} - be^{-ik_2 d}) = k_3 t \end{cases} \tag{2.20}$$

This is a system of four equations with four unknowns, which are the coefficients r, a, b and t. By solving it, we obtain:

$$\begin{cases} r = \frac{p^{-1}(k_1-k_2)-p(k_1+k_2+2k_2t)}{p^{-1}(k_1+k_2)-p(k_1-k_2)} \\ a = \frac{2k_1p^{-1}-(k_1-k_2)t}{p^{-1}(k_1+k_2)-p(k_1-k_2)} \\ b = \frac{(k_1+k_2)t-2k_1p)}{p^{-1}(k_1+k_2)-p(k_1-k_2)} \\ t = \frac{4k_1k_2}{p^{-1}(k_1+k_2)(k_2+k_3)-p(k_1-k_2)(k_3-k_2)} \end{cases} \tag{2.21}$$

where it was defined $p = e^{ik_2 d}$. The coefficients r, a, b and t can therefore be calculated from the refractive indices of each material. Knowledge of these coefficients, obtained from equations 2.21, allows one to obtain the z-dependent electric field inside each layer by means of equations 2.19.

As mentioned in section 2.4, the calculations described here are aimed at extracting the temperature increase after absorption of light in the Ru layer (layer 2). This is done by means of the two-temperature model (described in the next section, 2.4.2). This model takes as an input a source term, representing the increase in energy density in the material. This term is obtained by means of Poynting's theorem:[49]:

$$\frac{\partial u}{\partial t} = -\vec{\nabla} \cdot \langle \vec{S} \rangle \tag{2.22}$$

On the left-hand side, $\frac{\partial u}{\partial t}$ is the time-derivative of the energy density inside the material; on the right-hand side is the gradient of the energy flux, given by the time average over one oscillation period of the Poynting vector. The Poynting vector is defined as:

$$\vec{S} = \frac{1}{\mu_0} \vec{E}(z) \times \vec{B}(z) \tag{2.23}$$

$\vec{B}$ is the magnetic field of the radiation and μ_0 is the magnetic permeability of vacuum. The

time average of the Poynting vector corresponds to the intensity of the radiation, which also defines the intensity as $I \equiv \langle|\vec{S}|\rangle$.
As it was already mentioned, equations 2.21 and 2.19 allow to obtain the electric field everywhere inside the sample. The magnetic field is obtained from Maxwell's equations. Hence, the Poynting vector can be calculated in each region of the three-layer system by substituting equation 2.21 into 2.19, deriving the magnetic field using Maxwell's equations and calculating the cross-product in equation 2.23.
The source term $\sigma(z,t)$, necessary to calculate the lattice temperature increase by means of the two-temperature model is obtained as follows:

$$\sigma(z,t) = \frac{\partial u}{\partial t} = -\vec{\nabla} \cdot \langle\vec{S}\rangle \tag{2.24}$$

2.4.2 Two-temperature model

As was mentioned in section 2.4, in a metal, the energy of a laser pulse is absorbed by the free electron gas. On the timescale of a few hundreds of femtoseconds the electron gas thermalizes so that after absorption a well-defined temperature can be assigned to it[50]. On the picosecond timescale, the electron gas transfers energy to the lattice by the emission of phonons. The electron-phonon coupling constant g quantifies the efficiency of this process. This energy exchange between the electron gas and the lattice is described by the two-temperature model[47]. The following equations illustrates the spatial and temporal evolution of the temperature of the electron gas T_e and of the lattice T_l:

$$\begin{cases} C_e \frac{\partial T_e}{\partial t} = \frac{\partial}{\partial z}(k_e(T_e, T_l)\frac{\partial T_e}{\partial z}) - g(T_e - T_l) + \sigma(z,t) \\ C_l \frac{\partial T_l}{\partial t} = g(T_e - T_l) \end{cases} \tag{2.25}$$

Where:

- C_e and C_l are the electron and lattice heat capacities
- k_e is the electron thermal conductivity
- $\sigma(z,t)$ is the source determining the increase in electron temperature, obtained in section 2.4.1

All terms in this equation are in [W/m^3]. The first term on the right hand side of the first equation represents the local electron-gas energy loss/gain by thermal diffusion. The

second term, $g(T_e - T_l)$, quantifies the energy exchange between the electrons and the lattice through the electron-phonon coupling constant g. The second equation of the system describes the temperature change of the lattice due to electron-phonon coupling.

In equations 2.25, in-plane energy diffusion due to lateral temperature gradients was neglected, reducing the spatial dependence only to the variable z, corresponding to the direction orthogonal to the sample surface. This assumption is valid because we use this equation up to the time at which the difference in T_e and T_l is on the order of 10 % and because the beam spot size on the sample is often much larger than the layer thickness. This time-scale is approximately 2 ps. Lateral energy diffusion occurs at longer time-scales [51].
As already mentioned, solving numerically equations 2.25 allows to obtain the temperature profile which is subsequently used for performing the heat diffusion calculations described in the following section.

2.4.3 Heat diffusion calculations

In this section, the calculation performed to model the temporal evolution of the lattice temperature at the surface of the sample is described. The equation is written by assuming a cylinder with finite length and radial symmetry, which allows to remove the azimuthal-angle dependence from the equation, and it reads:

$$\frac{\partial u}{\partial t} = \frac{k}{\rho c}\left[\frac{\partial^2 u}{\partial r^2} + \frac{1}{r}\frac{\partial u}{\partial r}\right] + \frac{1}{\rho c}\frac{\partial k}{\partial z}\frac{\partial u}{\partial z} + \frac{k}{\rho c}\frac{\partial^2 u}{\partial z^2} \tag{2.26}$$

Where u is the temperature, r is the cylindrical radial coordinate, z is the depth within the layer, k is the thermal conductivity of Ru, ρ is its density and c the specific heat capacity. The z-dependence of the thermal conductivity ($k = k(z)$) is included in order to allow to model a system consisting of different layers. Its derivative is nonzero only at the interface between two materials which, in the case described here, is the interface between the Ru film and the substrate. Equation 2.26 was numerically solved using a forward-difference method while, at the interface between the Ru and the substrate, the equation was solved by applying the *jump matching condition*, as described in [52].
The results obtained by solving numerically equation 2.26, after extracting the initial conditions, as described in sections 2.4.1 and 2.4.2, were used to compare the temporal evolution of the surface temperature of a Ru thin film after exposure to a laser with two different diameters. The results are presented in chapter 5.

3

Femtosecond Laser Induced Emission of Coherent Terahertz Pulses from Ruthenium Thin Films*

Emission of electromagnetic pulses with frequencies in the terahertz (THz) range from ruthenium thin films through a second-order non-linear optical process is demonstrated. Ruthenium deposited on different substrates showed different THz emission properties. Evidence is provided that for Ru on glass, above a certain power threshold, laser-induced oxidation occurs, resulting in an increased slope of the linear dependence of the THz electric field amplitude on pump power. The THz electric field is mainly polarized parallel to the sample surface, pointing in the same direction everywhere. In contrast to Ru on glass, the electric field amplitude of the THz pulses emitted by Ru on sapphire and on CaF_2 shows a simple *single* linear dependence on pump power and it is polarized *orthogonal* to the sample surface. In this case thermal oxidation in an oven enhances the emission and introduces an additional polarization component along the sample surface. This component also points in the same direction everywhere on the surface, similar to as-deposited Ru on glass. Although the precise THz generation mechanism remains an open question, our results show a strong correlation between emission strength and the degree of oxidation. Furthermore, the results highlight the importance of the interfaces,

*This chapter was published in a slightly modified form as: J. Phys. Chem. C 127(46), 22662–22672 (2023)

i.e. both the choice of substrate and the chemical composition of the top surface in THz emission experiments. Knowledge of the state of the sample surface is therefore crucial for the interpretation of THz emission experiments from (non-magnetic) metal surfaces.

3.1 Introduction

Many materials have been shown to emit terahertz (THz) radiation when illuminated with femtosecond laser pulses. The most common ones are semiconductors [53,54,55], non-linear optical crystals such as ZnTe [37,56] and $LiNbO_3$ [57,58], and ferromagnetic metals [59,60]. For these materials the emission process is typically well understood.

Emission of coherent THz pulses from non-ferromagnetic metals has also been demonstrated. [61,62,63]. However, in this case the generation mechanism is less clear. This is partially caused by a number of occasionally contradictory observations. For example, high peak fluence illumination of gold gratings was shown to lead to the emission of THz pulses. This was explained by ponderomotive acceleration of photo-excited electrons in the evanescent field of the surface plasmon polaritons (SPPs) excited on the grating, giving rise to a third- to fourth-order dependence of THz power on pump power [64,65,66]. On the other hand, experiments performed at low peak fluence on Au surfaces also showed SPP-enhanced THz emission [67], although there, a second order non-linear optical process was observed. In this case, unlike in the high laser fluence experiments, the underlying generation mechanism remains an open question.

In general, one of the overlooked aspects in the interpretation of experiments on THz pulse emission from metals is the crucial role that the chemical state and morphology of the sample surface can play. For example, it has been shown that silver can react with H_2S molecules contained in air to create a layer of the semiconductor Ag_2S, forming a Schottky contact with the Ag below. This strongly enhances THz emission through acceleration of photo-excited carriers in the junction's depletion field [30]. Such contamination has been implicated in the search for a possible cause of the difference between THz emission from Au and from Ag observed by Kadlec *et al.* [61]. Still, it remains unexplained how this could cause a change in the order of the non-linear optical process. Likewise, emission of THz pulses from copper was reported by Suvorov *et al.* [29]. Although recording a surprising exponential dependence of the THz pulse energy on pump fluence, the state of the sample surface and the possible role of oxidation was not considered. It was subsequently shown, by Ramakrishnan *et al.* [68], that oxidation of copper results in the formation of a Cu_2O/Cu Schottky contact, enhancing THz emission. The aforementioned examples indicate that

it is crucial to properly determine the state of the sample surface as a starting point for a correct interpretation of the experimental results.
Here, it is shown that ruthenium thin films also emit THz radiation upon femtosecond laser illumination, and that the emission displays a second-order dependence on pump power. Surprisingly, above a certain power threshold, illumination of the Ru on glass strongly enhances the emitted THz electric field. This gives rise to a change in the slope of the linear dependence of THz electric field amplitude on pump power. This process is *not* observed for films deposited on sapphire and CaF_2, for which a *single-slope* linear dependence is seen.
Monitoring THz emission before and after annealing of an as-deposited Ru layer in the presence of oxygen and performing x-ray photoelectron spectroscopy (XPS), yields a clear correlation between emission strength and the degree of oxidation. In fact, upon oxidation, we observe an enhancement of the THz emission electric field amplitude by a factor of $\sim$5.7, corresponding to an increase in THz power by a factor of $\sim$33. These results provide strong evidence that the laser-induced enhancement seen above a certain power threshold is, in fact, caused by partial laser-induced oxidation of the Ru layer.
A surprising dependence of the THz polarization direction on the choice of the substrate is also observed. For ruthenium on glass, the THz electric field is parallel to the sample surface and has the same direction everywhere on the surface. For ruthenium on sapphire and on CaF_2, the THz electric field is polarized orthogonal to the sample surface. In this case, thermal oxidation, apart from enhancing the emission, introduces an additional polarization component parallel to the surface, similar to what is observed for as-deposited Ru on glass.
Emission is found to be independent of laser polarization direction, suggesting that it is not caused by a coherent laser-induced material polarization, but rather, by a laser-induced current.
Our results show the importance of the state of the surface in the emission of coherent THz pulses using femtosecond laser pulses. Moreover, they constitute a potent reminder that the pump laser itself is capable of modifying surfaces, thereby changing the THz emission.

3.2 Methods

The THz generation and detection setup is described in detail in chapter 2, section 2.2.1, and a schematic is shown in figure 2.7. It consists of a Ti:Sapphire laser which produces pulses with a central wavelength of 800 nm at a 5.2 MHz repetition rate and a duration of

approximately 70 fs. The beam is split into a generation (pump) and a detection (probe) arm. The pump power is varied by means of a half-wave plate and a polarizer and is focused on the sample to a spot with a diameter of about 700 μm. The samples are illuminated from the substrate side unless otherwise specified. Coherent THz radiation, emitted in the forward direction, is collimated and focused onto a 2 mm thick (110)-ZnTe crystal, where it co-propagates with the probe beam. Here, the time-dependent THz electric field is measured through electro-optic sampling [40]. An optical chopper modulates the pump beam at 10 kHz and provides the reference frequency used for lock-in detection. The THz beam path is flushed with dry N_2 gas to minimize absorption from water vapor, reducing the humidity down to $6\%_{RH}$, as measured with a hygrometer.

Ruthenium thin films were deposited on borosilicate glass and on sapphire and CaF_2 substrates by magnetron sputtering at an argon plasma pressure of 2×10^{-3} mbar, to a thickness of about 8 nm. Before deposition, the glass substrates were chemically cleaned using a solution of ammonium hydroxide (NH_4OH) with hydrogen peroxide and, after that, rinsed in isopropyl alcohol, while the sapphire and CaF_2 substrates were only rinsed in isopropyl alcohol.

THz emission in the forward direction was also observed for Ru layer thickness in a range between 5 nm and 20 nm without large variations as a function of thickness. Since the 8-nm-thick films showed slightly stronger emission than the other thicknesses, most of the results presented below were obtained using 8-nm-thick films (unless otherwise noted).

For the x-ray photoelectron spectroscopy (XPS) measurements, a monochromatic aluminium Kα x-ray source was used (producing 1486.6 eV photons). The number of emitted electrons as a function of their kinetic energy was measured by a Scienta Omicron HiPP-3 analyzer with a 0.8 mm aperture entrance cone and a slit setting of 1.0 mm. The peaks were analyzed using the KolXPD software and Doniach-Sunjic peak shapes convoluted with a gaussian function for ruthenium metal and ruthenium oxide. Voigt peak shapes were used for carbon and ruthenium oxide satellite peaks. A Shirley function was used to substract the background. More details on the XPS analysis are described in [69]. The atomic ratios were calculated from the peak areas divided by the respective photoemission cross-section.

Tapping mode AFM images were acquired using a Dimension ICON, Bruker with a RTESPA-300, Antimony (n)-doped Si, Bruker tip. The measured images were processed using Gwyddion software [70]. A fifth-degree polynomial flattening was used to correct the images.

3.3 Results

3.3.1 Terahertz emission and pump power dependence

In figure 3.1 the plot of a measured THz electric field as a function of time is shown, emitted by an 8 nm thick ruthenium film deposited on glass, illuminated at a 45° angle of incidence (AOI). Similar traces have been consistently recorded, showing no significant differences, for samples deposited on sapphire and CaF_2. The traces consist of single-cycle electric fields from approximately -0.8 ps to 0.5 ps (relative) delay. The quasi-oscillatory signal seen for delays beyond 0.6 ps, is caused by spectral filtering of THz light by water vapor not completely removed by purging with the N_2 gas [23]. We note that the signals typically obtained in our setup from the 8-nm-thick Ru samples are rather weak: by a rough comparison, we estimate them to be approximately three orders of magnitude lower in amplitude than those obtained from a 0.5 mm (110)-ZnTe crystal. In order to confirm that

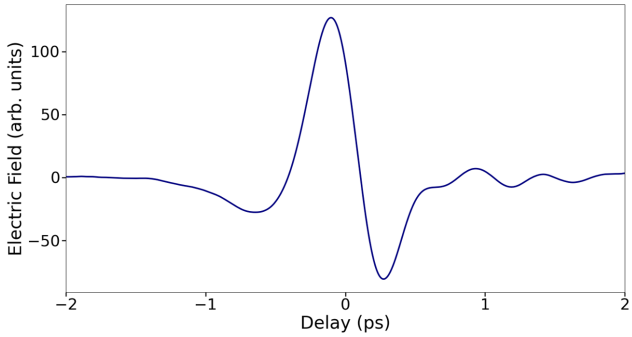

Figure 3.1: Measured THz electric field as a function of time, emitted from an 8 nm thick Ru layer on glass after illumination with an 800-nm central-wavelength femtosecond laser pulse.

the Ru layer is responsible for the THz emission, and not the substrate, we also performed measurements on bare substrates. No emission was observed within the sensitivity of our setup. Additionally, measurements on a 150 nm thick Ru layer deposited on glass were also performed by illuminating the samples from the metal side. In this case, no transmission of laser light was detectable, all of it being partially absorbed and partially reflected by the thick metal layer. The penetration depth for 800 nm light in ruthenium is approximately 15 nm [48]. When illuminating the 150-nm-thick ruthenium sample from the metal side, no light reaches the Ru/substrate interface. In addition, the electron-phonon coupling constant in Ru is high, so that on the time scale of a few picoseconds, a negligible amount of electron energy reaches the Ru/substrate interface [71]. In this case, THz emission in the reflection direction was also observed but not in the transmission direction. This supports

the conclusion that the emission comes from the metal surface (or from a layer near to it) rather than from the Ru/substrate interface.

To measure the order of the optical non-linearity the peak-to-peak (pk-pk) field amplitudes of the THz pulses as a function of average pump power P_{pump} were extracted. The resulting curve, measured for 8 nm Ru on sapphire at an AOI of 45°, is plotted in figure 3.2. The data follow a linear trend, as highlighted by the linear fit plotted as a solid line. A similar behavior was observed for Ru deposited on CaF_2. These measurements suggest that the emission is due to a second-order non-linear optical process.

Figure 3.3(a) shows the pk-pk field amplitude of the emitted THz pulses as a function of

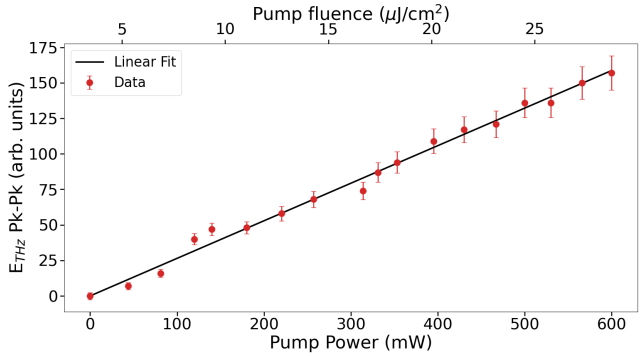

Figure 3.2: THz pk-pk electric field amplitude emitted by an 8 nm thick Ru layer deposited on sapphire as a function of pump power. The solid line is a linear fit. Similar results have been obtained for Ru on CaF_2.

P_{pump} for an 8 nm thick Ru film deposited on glass, illuminated at a 45° AOI. For pump powers below approximately 250 mW (pump fluence of 12.5 μJ/cm^2) the THz electric field amplitude scales linearly with pump power. However, around a pump power of 250 mW, a transition to a different linear power-dependence regime is observed, one with a steeper slope, extending to at least 700 mW (35 μJ/cm^2). The sudden change in slope at P_{pump} higher than 250 mW deviates from the observations for Ru on sapphire and CaF_2, where no such change was observed. As it will be shown below, the results for Ru on glass are caused by a permanent laser-induced material modification occurring at high-power illumination. This modification could be responsible for the enhanced THz emission observed at high power illumination. It should be pointed out that the data plotted in figure 3.3(a) were obtained by continuously measuring at the same spot on the sample, going from low to high pump power. This means that each data point is the result of the cumulative exposure to all the lower powers used previously.

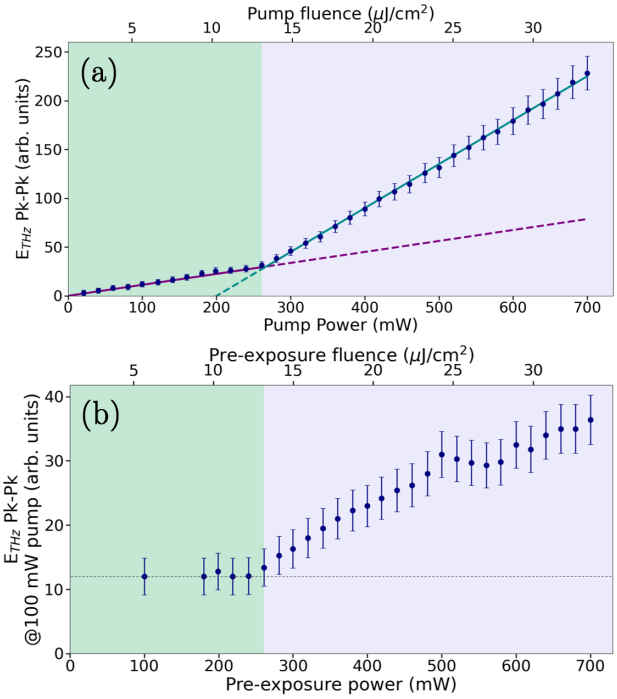

Figure 3.3: **(a)** THz peak-to-peak electric field amplitude as a function of pump power for Ru on glass. Linear fits are plotted as solid lines, they are extended as dashed lines to emphasize the different slopes. **(b)** THz peak-to-peak amplitudes emitted at a fixed reference pump power of 100 mW (pump fluence of 5μJ/cm^2) as a function of laser pre-exposure power, for 240 s exposure time. The horizontal dashed line indicates the THz pk-pk amplitude emitted prior to laser exposure.

3.3.2 Laser-induced material modifications

The THz emission versus pump-power qualitatively changes at a pump power of about 250 mW. Here, it is demonstrated that these changes are irreversible, indicating a permanent material modification.

In order to monitor the change in THz emission caused by laser exposure, the THz emission at a pump power $P_{ref} = 100$ mW (reference fluence of 5μJ/cm^2) was recorded after pre-exposing the sample to increasing laser powers for a fixed time duration of 240 s. The experiment was carried out by illuminating a single spot and going from low to high pre-exposure powers. The peak-to-peak THz electric field emitted by the Ru at reference pump power of 100 mW (5μJ/cm^2), as a function of pre-exposure power, are shown in figure 3.3(b). The data show that the emission amplitude is approximately constant for low exposure powers, up to approximately 250 mW (12.5 μJ/cm^2). From 250 mW until 700 mW (12.5 until 35 μJ/cm^2), the emission amplitude increases, reaching an enhance-

ment factor of THz electric field amplitude of approximately 3, equivalent to a factor of 9 in power. The observed increase of the THz emission at a given pump power after laser exposure is a permanent effect: the metal is permanently modified by laser exposure in a way that makes it capable of emitting more intense THz light. Furthermore, the onset of the "steeper slope" regime in figure 3.3(a) and of the emission enhancement of figure 3.3(b) are both located around 250 mW pump/exposure power (12.5 μJ/cm^2 pump/exposure fluence). This correspondence suggests that the change in slope of the power dependence is the result of a progressive material modification caused by the pump laser during the measurement.

3.3.3 Thermal oxidation and x-ray photoelectron spectroscopy

Given the results presented above, it seems likely that some form of laser-induced-annealing was responsible for the enhanced THz emission observed after high power illumination. To test this, THz signals obtained before and after annealing the samples in an oven in a 10^{-3} mbar O_2 atmosphere at 400 °C for 60 minutes were compared. Before annealing, the samples were kept in vacuum (10^{-5} mbar) for 30 minutes to allow evaporation of water films on the sample and on the walls of the oven, as well as to purge other contaminants such as carbon-containing molecules.

Figure 3.4(a) shows the THz traces obtained before (blue) and after (orange) oxidation from Ru on glass. We observe a THz electric field enhancement factor of approximately 3 after annealing in the O_2 atmosphere. A similar effect is observed for Ru on CaF_2 (figure 3.4(b)) and sapphire substrate (not shown). The enhancement factor for Ru on CaF_2 is 5.7, which becomes particularly impressive considering that it corresponds to a 36-fold increase in THz power. The enhanced emission amplitude observed at high pump power from the not-annealed sample seems to be correlated with an increased presence of ruthenium oxide.

Within the signal to noise of these experiments, and taking the relatively limited phase-matching bandwidth of the 2 mm thick ZnTe detection crystal into account, we are unable to determine whether the rise time or bandwidths of the generated THz pulses before and after oxidation are different.

The same pump-power-dependent measurements as those in figure 3.3 were performed on Ru on glass *after* thermal oxidation at 400 °C in a 10^{-3} mbar oxygen atmosphere for 1 hour. Enhanced THz emission amplitude was observed compared to the emission from a pristine sample. However, a single linear trend was recorded, with no change in slope at

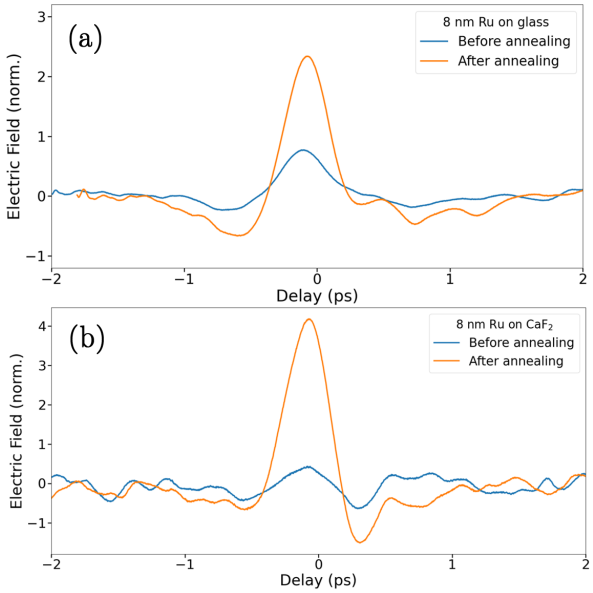

Figure 3.4: THz electric field as a function of time emitted after excitation with an 800 nm pump pulse measured from 8 nm Ru before (blue) and after (orange) thermal oxidation. The traces are normalized to the peak-to-peak amplitude of the THz pulses obtained before thermal oxidation. **(a)** Emission from Ru on a glass substrate, **(b)** emission from Ru on CaF_2.

high pump powers. This implies that no further laser-induced modification occurs for a sample pre-oxidized under these conditions.

To confirm the correlation between increased Ru oxidation and enhanced THz emission, XPS was performed on an 8 nm thick Ru-on-glass sample on an area exposed to high laser power, on an un-exposed one and on a thermally oxidized sample.

The resulting data are plotted in figure 3.5, showing the Ru 3d lines (Ru $3d_{5/2}$ at 279.8 eV and Ru $3d_{3/2}$ at 284 eV). Figure 3.5(a) shows the spectrum of as-deposited ruthenium (area not exposed to laser light). Apart from the Ru metal peaks we observe a weak contribution from RuO_x at 281.7 eV and 286 eV. From these measurements, a thickness of this oxide layer of approximately 0.5 nm is extracted, and a ratio of oxidized over metallic ruthenium (RuO_x/Ru-M) of 0.10. We also notice the presence of carbon contamination appearing as the C 1s peak at 284.8 eV. For this sample (pristine Ru, area not exposed to laser light), the atomic ratio of carbon over ruthenium (C/Ru) is 0.32. The XPS spectrum obtained from the area exposed to high laser power is shown in figure 3.5(b). Relative to the Ru metal peaks, we observe a strong increase of the RuO_x peaks, as well as the rise of the RuO_2 satellite peak at 283.6 eV. The latter is a signature of the presence of the ruthe-

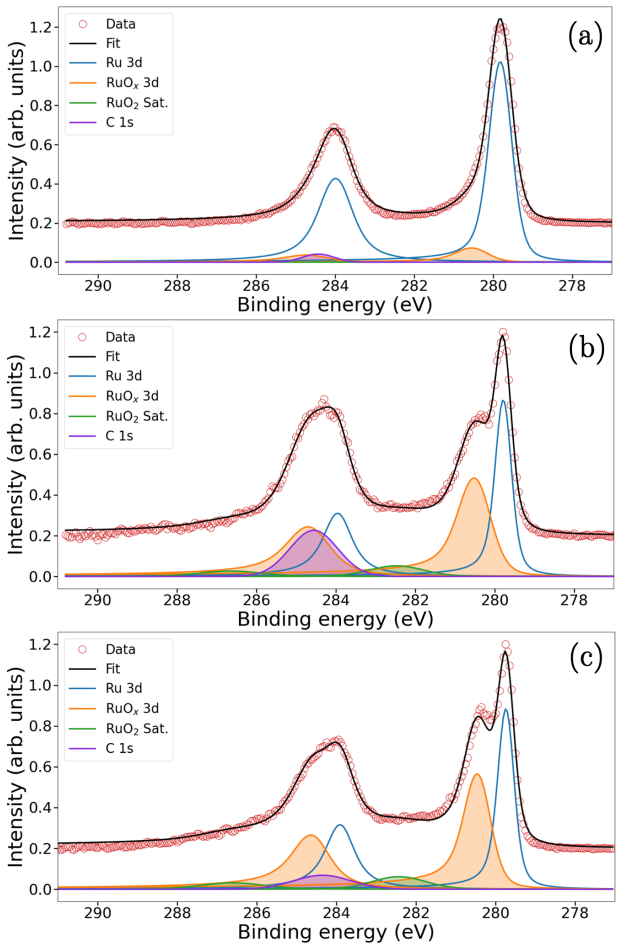

Figure 3.5: XPS of an 8 nm Ru sample on glass. **(a)** XPS spectrum measured on a region not exposed to high laser power in air, **(b)** on a region exposed to high laser power and **(c)** on a sample annealed in 10^{-3} mbar of oxygen.

nium oxide rutile phase [72]. In this case, the RuO_x/Ru-M ratio is 1.06. We also observe an increase in carbon content through the C 1s peak, leading to a C/Ru atomic ratio of 2.16. Compared to the unexposed region discussed previously, this corresponds to a 6.75-fold relative increase in carbon intensity and a 10-fold increase in oxidized Ru.

Up to this point, enhanced THz emission resulting from high laser power exposure seems to correlate both with increased ruthenium oxidation and increased presence of carbon. Since we suspected that laser-induced carbon deposition can occur in ambient atmosphere, XPS on a sample annealed in a 10^{-3} mbar O_2 atmosphere at 350 °C for 30 minutes was also performed. Similar to the samples used for the measurements reported in figure 3.4, these

samples were kept in vacuum for 30 minutes before and after the annealing.This treatment is expected to result in a lower carbon content, allowing to clarify to what extent carbon deposition plays a role in enhancing the THz emission.

Figure 3.5(c) shows the resulting XPS spectrum. The spectrum, again, shows increased ruthenium oxidation, resulting in a RuO_x/Ru-M ratio of 1.03, comparable to the value obtained from the laser exposed region (1.06, figure 3.5(b)). The C 1s peak located at 284.8 eV, on the other hand, is significantly lower, as can easily be seen by comparing the relative peaks in figure 3.5(b) and figure 3.5(c). The resulting C/Ru atomic ratio, in this case, is 0.77.

These results support the conclusion that only increased Ru oxidation (not carbon deposition) and THz emission strength are strongly correlated.

A qualitative explanation for the fact that the laser-induced THz emission enhancement has not been observed with sapphire and CaF_2 substrates could be the difference in thermal conductivity between the three substrates. Their thermal conductivities are 1.15 W/K·m for glass [73], 9.7 W/K·m for CaF_2 [74] and 23 W/K·m for sapphire [75]. This implies that the glass substrate allows the metal to retain heat for a longer time after absorption of laser light and to reach a high enough temperature to overcome the reaction barrier for the material modification. The thermal conductivities of the crystalline substrates on the other hand, could be high enough to cause the Ru temperature to decrease below the value where oxidation can occur more quickly [51].

It would be interesting to estimate the time evolution of the temperature of the Ru during excitation. However, estimating the temperature increase is rather difficult in our case. A maximum Ru temperature shortly after excitation with a single laser pulses can easily be estimated. With a specific heat of Ru of 0.238 x 10^3 J/(kg·K), an estimated absorbed energy of 29 nJ per pulse, and a laser beam radius on the 8-nm-thick sample of about 350 μm, we get a temperature increase for a single laser pulse of about 3.4 K. However, calculating the temperature is significantly more complicated for multiple pulses. This is due to the fact that we use a 5.2 MHz repetition rate laser. In this case, heat accumulation due to the short time interval between the pulses plays a role, and changes in the absorption coefficient due to gradual heating of the material during excitation are difficult to predict. Furthermore, as we already mentioned, heat diffusion into the substrate is also bound to occur, requiring knowledge about the heat resistivity between the ruthenium and the substrate for an estimate of the temperature reached after a certain time interval. However, the experiments clearly show that sufficiently high temperatures are reached for a sufficiently long period of time for partial oxidation to occur.

3.3.4 Dependence of THz emission on the sample azimuthal orientation

Many conventional non-absorbing THz emitters such as ZnTe or GaP show a distinct azimuthal-angle dependence in the emitted THz polarization direction, when the emitter is rotated around the normal to the surface. As we cannot rule out that our samples might behave in a similar way, we have also measured THz emission as a function of the sample azimuthal angle φ. This was done at low pump power (150 mW, 7.5 μJ/cm^2) to avoid self-induced material modifications.

In general, $\vec{E}_{THz}$ can be decomposed into a component parallel, $\vec{E}_{THz\parallel}$, and orthogonal, $\vec{E}_{THz\perp}$, to the sample surface (see inset of figure 3.6(b)). At an AOI of 45°, both the in-plane and orthogonal-to-the-surface electric field have a component perpendicular to the pump and probe beam propagation direction, and can therefore be measured in our setup. Changing the azimuthal angle by rotating the sample around the direction normal to the surface has no effect on $\vec{E}_{THz\perp}$, since it is parallel to the rotation axis. This means that the presence of the component of the THz-polarization orthogonal to the sample surface results in a *φ-independent* offset in the azimuthal-angle-dependent measurements. A φ-dependent contribution occurs only if $\vec{E}_{THz\parallel}$ is present *and* and if it points towards a fixed direction on the sample surface. In this case, rotating the sample rotates this polarization component as well, with respect to the (fixed) laser polarization.

The THz traces obtained as a function of the azimuthal angle of an 8 nm Ru sample on glass, illuminated at a 45° AOI, are plotted in figure 3.6(a). The amplitude of the pulses clearly depends on the angle φ and the absolute value reaches a maximum for $\varphi = 180°, 0°$ and 360°, and reaches a minimum for $\varphi = 90°$ and 270°. The measurements have been performed at a fixed orientation of the ZnTe detection crystal. Although we did not determine the absolute sign of E_{THz} with our setup (see experimental section and Planken *et al.* [40]), changes in the sign of the THz peaks correspond to actual flips in the sign of the THz electric field. The peak-to-peak amplitudes of the traces plotted in figure 3.6(a) were extracted and a plus or minus sign was assigned to the values obtained for each trace depending on the sign of the first peak. In this way, for instance, the trace corresponding to $\varphi = 180°$ results in a positive pk-pk value, while the one at $\varphi = 0°$ in a negative one. This convention has been used for all the results discussed below. The values obtained from the traces of figure 3.6(a) are plotted in figure 3.6(b). The data were fitted with a function of the form $A \sin(\varphi + \alpha) + \Delta$; A describes the variation of the THz amplitudes as a function of the azimuthal angle φ, Δ the azimuthally-independent contribution to the THz emission (related to $\vec{E}_{THz}$, see above). α is a phase offset. Figure 3.6(b), together with the values

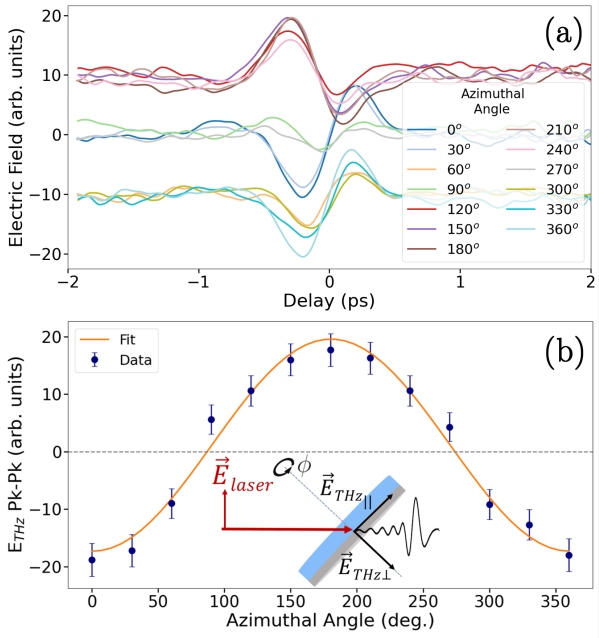

Figure 3.6: **(a)** THz traces obtained at different azimuthal orientations at a 45° angle of incidence for Ru deposited on glass. The traces have been vertically displaced in three groups for clarity, despite corresponding to the same set of measurements. **(b)** Pk-pk amplitudes extracted from the traces of figure **(a)** (blue dots) and fitted curve (orange). Inset: schematic of the two components of the vector THz electric field. The red arrows represent the laser beam propagation direction and its p-polarized electric field.

of $A = 18.5$ and $\Delta = 1.1$, shows that, for Ru on glass, the main component of the THz-polarization is parallel to the sample surface. This conclusion is further supported by the fact that THz emission was also measured at normal incidence. Furthermore, from such azimuthal-angle dependences, we find that the THz-polarization points towards a fixed direction on the surface, such that sample rotations are accompanied by rotations of the THz polarization. At a given orientation of the ZnTe electro-optic detection crystal, there is an optimal sample orientation which maximizes the detected THz signal [40].

The azimuthal-angle dependence of the in-plane THz polarization component follows a simple sine (or cosine) dependence and is a linear polarization [40]. However, knowing the absolute linear direction of the THz polarization is not very useful unless we can somehow connect this to another ”directional” feature on the sample surface, which we unfortunately haven't been able to do. The rotation of the THz-polarization highlighted by figures 3.6 should be interpreted as a rotation relative to some preferential direction that was not possible to conclusively identify using the diagnostic tools at our disposal.

It should be pointed out that the measurements were performed by focusing the laser on

a spot at a somewhat random distance from the rotation axis of the samples. As a result a different part on the sample is illuminated at each azimuthal angle. Nevertheless, the same THz signal is obtained at a given φ throughout the whole sample. This means that the direction of the emitted THz electric field component parallel to the sample surface is the same over the whole sample. The effect is therefore macroscopic, in contrast to the observation of Zhang *et al.* [63].

To understand whether this azimuthal-angle dependence results from an anisotropy present in the absorption process or whether it occurs purely at the emission stage, we have measured the THz emission as a function of pump-polarization direction. The measurements have been performed at normal incidence to eliminate the dependence of the sample reflection on the pump polarization. The results (appendix 3.6.1) do not show any measurable dependence on the incident polarization. In contrast, varying the sample azimuthal angle in the same normal incidence configuration produces a clear sinusoidal dependence, strongly suggesting that the azimuthal-angle-dependence stems purely from the emission process. The results obtained by varying the incident pump polarization make it less likely that a macroscopic single-crystal-like pump-induced, second-order non-linear optical polarization is responsible for the emission.

2D-x-ray diffraction at grazing incidence was performed on a 20 nm Ru sample after confirming that azimuthal-angle dependence of the THz-emission was also present for this sample. The sample thickness was chosen in order to reduce x-ray diffraction contributions from the substrate. The measurements were carried out to determine whether a preferred crystal direction was present in our samples (texturing). No preferential crystal orientation was observed within the measurement accuracy (figure 3.10).

Surprisingly, no THz pulse generation and thus no azimuthal angle dependence were observed at normal incidence for ruthenium films deposited on sapphire or CaF_2 substrates, unless the samples were thermally oxidized under conditions such as the ones resulting in figure 3.4. These observations show a substantial difference between the emission process in as-deposited Ru on glass and on sapphire/CaF_2. To understand the appearance of azimuthal-angle-dependence in the THz emission for Ru deposited on sapphire, measurements were performed after annealing the 8-nm Ru samples on sapphire in an O_2 atmosphere at a 10^{-3} mbar pressure, for 30 minutes. The degree of oxidation was varied by changing the annealing temperature T. The samples were then placed at a 45° AOI to access both electric field polarization components of the emitted $\vec{E}_{THz}$, parallel and perpendicular to the surface. THz time traces as a function of φ were recorded and the pk-pk amplitude values were extracted following the same procedure as the one described for figure

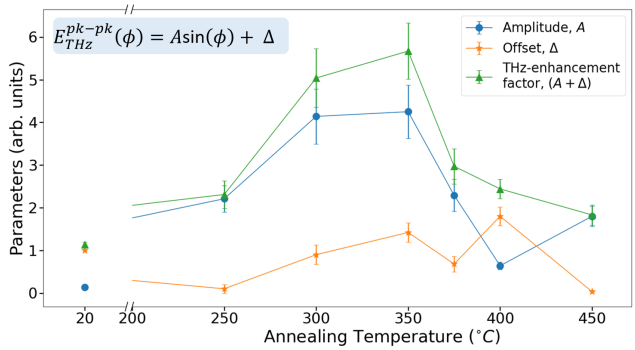

Figure 3.7: Parameters extracted from azimuthal-angle dependent THz pk-pk amplitude measurements, similar to figure 3.6, as a function of annealing temperature for Ru on sapphire. The values are normalized by the azimuthal-angle independent emission amplitude *before* thermal oxidation of Ru on sapphire. The parameters were obtained by fitting a function of the form $A\sin(\varphi) + \Delta$ to the data. A (blue) is the amplitude of the azimuthal variation, related to the anisotropic component of the THz generation process along the sample surface. Δ is the offset of the sinusoidal curve, related to the component orthogonal so the sample surface. The THz-enhancement factor (green) is the maximum THz electric field obtained as a function of the azimuthal angle φ.

3.6. The parameters A and Δ were extracted and divided by the THz-peak-to-peak amplitude emitted by each sample before annealing (measured on the same day). This scaling was performed in order to circumvent variations of the THz-emission due to slight differences between the samples and/or beam alignment. The results are plotted in figure 3.7. The sum of the two scaled parameters, which we define here as THz-enhancement factor, shown in green, corresponds to the maximum THz electric field observed as a function of φ after annealing, divided by the φ-independent THz-peak-to-peak amplitude measured before annealing.

The figure shows that the THz enhancement factor increases with annealing temperatures up to 350 °C and decreases for higher temperatures. A similar behavior is observed for A and Δ separately, the latter peaking at 400 °C rather than 350 °C.

In agreement with the results of figure 3.4, the THz-enhancement factor increases with oxidation. It reaches a maximum value of 5.7 for the electric field, equivalent to a factor of 32 in power, at 350 °C. As explained above, the development of the parameters A and Δ provides information on the direction of the $\vec{E}_{THz}$ vector. Without annealing, the THz field polarization is completely orthogonal to the sample surface for Ru on sapphire and on CaF_2, and thus no in-plane THz electric field component is present. The growth of the oxide layer introduces a component parallel to the surface, pointing in the same direction everywhere on the sample, as highlighted by the presence of the azimuthal-angle

dependence ($A \neq 0$). A increases from 250 °C, peaks at 350 °C and decreases at higher annealing temperatures; similarly, Δ increases from 250 °C but it peaks at 400 °C. This seems to indicate that the growth of the oxide layer does corresponds to the combined increase of both THz-polarization component, at least until 350 °C annealing temperature.

3.3.5 Surface morphology: atomic force microscopy

There is a clear azimuthal angle sine-dependence when the Ru samples are rotated around the surface normal. Normally, this would imply some fixed direction of emission and one would expect the presence of some form of directionality in the sample, perhaps in the form of oriented microcrystals. For this reason, tapping mode atomic force microscopy (AFM) was used to examine changes in the surface morphology upon thermal oxidation.
Figure 3.8 shows the results for Ru on glass before (figure 3.8(a)) and after (figure 3.8(b)) thermal oxidation in a 10^{-3} mbar O_2 atmosphere at 350 °C for 30 minutes. Increased surface roughness is observed as a result of a higher density of nano-protrusions (bright spots) on the oxidized sample with respect to the as-deposited one. This observation agrees with the results by Jelenkovic *et al.* [76].
In an attempt to identify the source of the anisotropy observed in the THz emission we show the AFM image of a smaller area of the annealed sample in figure 3.8(c). This gives a clearer view of the nano-protrusions and allows us to extract four height cross sections of these features, indicated in figure 3.8(c) by the numbered arrows and plotted in figure 3.8(d). Although their size varies, they reach approximately 8 nm in height with a base width of approzimately 30 nm. Cross section number 1 shows an asymmetric shape, being somewhat steeper on the left hand side than on the right. The same applies to profile number 2 and 4. The asymmetry is far less evident in profile number 3. We identify these features as the precursors of the nano-pillars observed by Coloma Ribera *et al.* in [77].
Although a similar asymmetry appears with different AFM tips and on different samples, we do not exclude the possibility of a tip artifact caused by asymmetric AFM tips [78]. The evidence for the asymmetry is therefore inconclusive.
AFM measurements were also performed on 8 nm Ru deposited on sapphire (appendix 3.6.3). Prior to annealing we observe a smaller density of the nano-protrusions compared to Ru on glass. Also, the features are higher in glass compared to Sapphire. A similar increase in surface roughness is observed as a function of annealing temperature. This seems to indicate that such nano-protrusions might be the source of the anisotropy observed in the THz emission, although proving this is currently difficult.

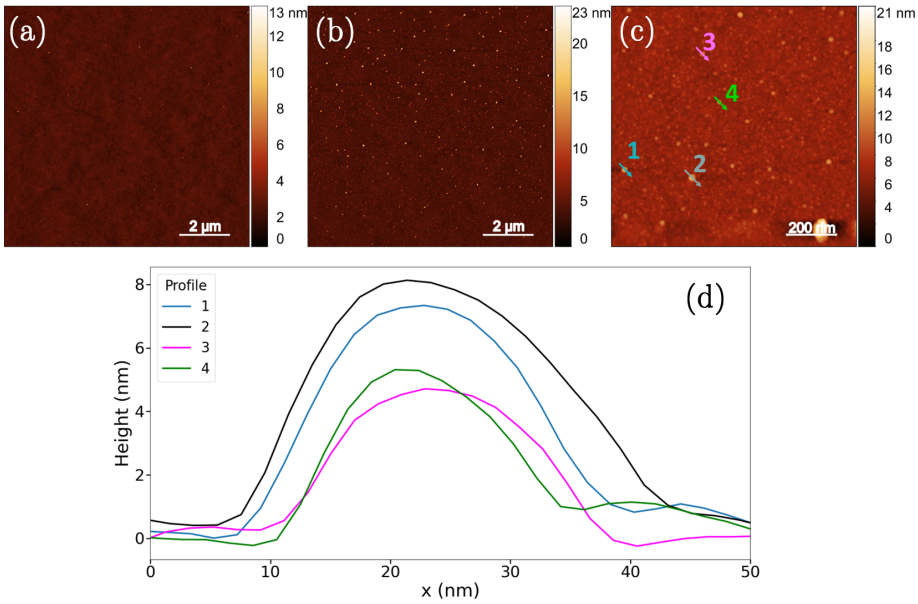

Figure 3.8: AFM images of Ru on glass.**(a)** before thermal oxidation and **(b)** after thermal oxidation at 350 °C. Increased presence of nano-protrusion can be seen by comparing these two images. **(c)** Zoomed-in AFM image of the thermally oxidized sample. The arrows correspond to the direction of the height cross-sections plotted in **(d)**. Here, it can be seen that profiles number 1,2 and 4 are steeper on the left hand side, whereas profile number 3 is symmetric or only weakly asymmetric.

3.4 Discussion

3.4.1 Correlation between THz-emission amplitude and oxidation

The enhancement of THz emission observed after high-power illumination, as well as after annealing in an O_2 atmosphere, in combination with XPS measurements, indicates that oxidation plays an important role in the THz generation process.

Exposing Ru on glass to high laser powers enhances THz emission by a factor of approximately 3 in THz electric field (9 in THz power, figures 3.3(a) and 3.3(b)) and increments both oxidation and carbon content (figure 3.5(a)) with respect to as-deposited samples. Annealing of pristine Ru on glass in O_2 results in a similar THz emission-enhancement-factor (figures 3.4) and oxide content, compared to the previous case, but a much lower increase in carbon content (figure 3.5(b)). Therefore, THz emission-strength strongly correlates with oxidation. The correlation with carbon content, if present, is much weaker. As a consequence it seems likely that oxidation causes the change in slope of the THz electric field amplitude dependence on pump power for Ru on glass by enhancing the THz emission

(figures 3.3(a) and (b)). This correlation points towards a generation mechanism based on the interaction between the Ru and the Ru-oxide layers.

It has been demonstrated (figure 3.5(a)) that a thin sub-nanometer thick (∼0.5 nm) layer of oxide is formed on top of a ruthenium film under ambient conditions, a feature observed also by Coloma Ribera *et al.* [77]. Thermal annealing has been proven to lead to the formation of the rutile phase RuO_2 [79]. Although we are unable to precisely monitor the thickness of the Ru and RuO_2 layers for each annealing temperature, the oxidized layer is known to grow in thickness with annealing temperature and with annealing time [19]. We believe that the relatively weak THz emission of the as-deposited samples, compared to the thermally oxidized ones, is due to the small thickness of the native oxide layer formed by contact with the atmosphere.

From the literature and from our XPS measurements we know that a native oxide forms on as-deposited Ru thin films upon contact with ambient air [77,79], a so called O-Ru-O trilayer. Thermal annealing above a threshold temperature causes the formation of the RuO_2 rutile phase, which grows with annealing time and temperature. The fact that a single threshold power is observed for the pump-power-dependence of THz emission from Ru on glass (figure 3.3(a)) indicates that a Ru/RuO_2 bilayer is forming, rather than a heterojuction with multiple layers. Although both Ru and RuO_2 are conductive (RuO_2 has a resistivity of 76 $\mu\Omega\ cm$ [80], compared to the one of Ru being 7.1 $\mu\Omega\ cm$ [81]), they might form a Schottky junction. In that case, acceleration of photoexcited carriers in the junction's depletion field would be a possible generation mechanism, similar to the one described in [68] for Cu/CuO_x. However, in our case, the depletion width would most likely be extremely narrow since both Ru and RuO_2 have high carrier concentrations. This emission mechanism, however, would result in a THz electric field polarized orthogonal to the sample surface, which does not explain the in-plane main THz polarization component that we observe.

The THz-emission-enhancement factor grows with increasing annealing temperature, up until approximately 350 °C (figure 3.7), after which it starts to decrease again. It is possible that, at this temperature, some optimal relative thickness of the ruthenium oxide with respect to metallic ruthenium is reached.

3.4.2 THz polarization direction: role of the substrate

Thermal oxidation of Ru, apart from enhancing the THz emission with each substrate tested, also results in a change in the polarization direction of the THz electric field for Ru on sapphire and CaF_2. On these substrates $\vec{E}_{THz}$ is orthogonal to the sample surface prior to oxidation (no emission when pump is at normal incidence, no azimuthal-angle dependence); a component parallel to the surface appears after oxidation (emission when pump is at normal incidence, azimuthal-angle dependent emission at 45° incidence). Remarkably, ruthenium on glass emits THz-pulses with both polarization components also when *no* thermal oxidation is performed. Any time a parallel component is present, a dependence of the THz electric field amplitude on the sample azimuthal orientation is observed. The fact that azimuthal-angle dependence is observed for as-deposited Ru on glass, but not on sapphire and CaF_2, shows that the the substrate plays a role in the THz emission.
Our observations suggest that the degree of oxidation correlates with the presence of a THz-polarization component parallel to the surface. Although such polarization component is not present in ruthenium as-deposited on sapphire and CaF_2, it is present also in as-deposited ruthenium on glass. Nevertheless, it is known that chemical reactions can occur, even at room temperature, between metallic films and silicon substrates [82]. We speculate that, perhaps, a similar effect could be occurring with glass substrates during ruthenium deposition. If true, a ruthenium oxide layer forms at the interface with the substrate, in addition to the one formed upon contact with air. Chemical changes at the metal/substrate interface would not easily be detectable through XPS due to its surface sensitivity which is limited to the uppermost ∼6 nm. Crystalline substrates such as sapphire and CaF_2 could be chemically too stable, compared to glass, to react with the metal. Furthermore, CaF_2 contains no oxygen. Therefore, although some process at the interface between the metal and the substrate may be occurring, we have evidence that it corresponds to the formation of an additional oxide layer and, in fact, the high stability of SiO_2 (contained in borosilicate glass) compared to that of ruthenium oxide, in principle, does not favor this process [83,77]. Our confidence in this explanation is therefore fairly low.

3.4.3 Search for a source of asymmetry

AFM measurements (figures 3.8) showed that oxidation is also accompanied by increased surface roughness, related to the growth of nano-protrusions. Such features seem to tilt towards a preferential direction, but, we cannot exclude the possibility that this is a result of a tip artifact. No other measurable asymmetry was found using other diagnostics tech-

niques. 2D-XRD, in fact, showed that, before annealing, our Ru on glass samples consist of polycrystalline Ru with no clearly measurable preferential crystal orientation (appendix 3.6.2).

3.4.4 Potential explanation based on previous observations

We note that THz emission from ruthenium deposited on porous glass was reported by Zhang *et al.* [63]. Azimuthal-angle-dependent THz emission was also observed in that case. Similar to our results, Zhang *et al.* did not observe azimuthal-angle dependence for Ru deposited on sapphire substrates. The azimuthal-angle dependence was explained by an anisotropic porous glass structure. Although our samples are different from the nanostructured ones by Zhang's group, it is tempting to compare their results with ours. In particular, it would be interesting to find out whether the anisotropy in THz emission that they observed is caused by the porous nanostructure itself or by a more subtle mechanism, still related to the substrate choice, similar to the one taking place in our non-nanostructured ruthenium films.

THz generation from heterostructures composed of a non-magnetic metal and single-crystal RuO_2 or IrO_2 has been reported very recently by S. Zhang *et al.* [84]. The proposed generation mechanism is based on current injection from the non-magnetic metal into the single-crystal oxide, and subsequent deflection induced by its anisotropic conductivity. Although we find it unlikely that a crystal-symmetry-based model could apply to polycrystalline films, a similar mechanism could be occurring in our samples if we could assume a weak, sample-wide net orientation of the RuO_2 crystallites. In that case, electrons excited in the metallic Ru would give rise to a current inside the RuO_2 with an in-plane component and thus THz emission with a field-component parallel to the surface.

THz emission with a polarization component parallel to the sample surface and independent on the pump-laser polarization direction was reported by B. Guzelturk *et al.* for periodic stripe-domain multiferroic materials (BFO) [85]. In that work, the THz-polarization direction is related to the direction of the ferroelectric polarization and the THz-emission amplitude is shown to correlate with the density of the domain walls (DW). However, to our knowledge, ruthenium and ruthenium oxide have not been proven to possess any ferroelectric behavior. Therefore, this seems an unlikely explanation for the in-plane polarization component observed in our measurements.

3.5 Conclusion

We have shown that 8-nm-thick ruthenium films are capable of emitting coherent THz radiation when illuminated with femtosecond laser pulses through a second order non-linear optical process. Laser-induced THz-field enhancement was observed when using glass substrates. This manifests itself as a change in the slope of the linear dependence of the THz-field amplitude on pump power at a certain threshold, and as an increased emission at a fixed pump power as a result of pre-exposure to high laser powers. XPS shows that this behavior is most likely due to laser-induced oxidation. The laser-induced enhancement was not observed for films deposited on sapphire or CaF_2. For these samples a "pure" linear dependence was observed. Nevertheless, for these substrates, annealing the metal films in an O_2 atmosphere at high temperature resulted in increased emission in addition to the formation of a THz field component parallel to the surface. These results show a correlation between oxidation and enhanced THz emission for all substrates. We observed a large THz-field enhancement, reaching a factor of 6 for Ru on CaF_2, corresponding to a power enhancement of a factor of approximately 36.
Although the exact generation mechanism of THz electromagnetic radiation from ruthenium thin films as a consequence of femtosecond laser illumination remains an open question, we have provided a comprehensive characterization of the emission features. In addition, our results demonstrate the importance of an accurate determination of the state of the sample surface for a correct interpretation of the experimental results.

3.6 Appendices

3.6.1 Dependence of THz emission on incident laser polarization

Figure 3.9(a) shows the peak-to-peak amplitude of the THz electric-field emitted by a 8 nm Ru sample as a function of the angle of incident (linear) polarization. This angle was varied by means of a half-wave plate. The measurements were carried out at normal incidence to exclude the dependence of the absorption on incident polarization at non-zero AOI. Figure 3.9(b) shows the THz electric-field peak-to-peak amplitude as a function of the sample azimuthal orientation. These measurements were carried out in the same configuration and on the same sample as the ones reported in figure 3.9(a). By comparing these two plots and the values of the fit parameter A (obtained via the procedure explained for figure 3.6), 0.79 ± 0.6 for figure 3.9(a), 22.7 ± 1.12 for figure 3.9(b)) it is clear that rotating the incident polarization has little to no effect on THz emission, while rotating the sample has

an evident effect, as is also show in the main text (figure 3.6).

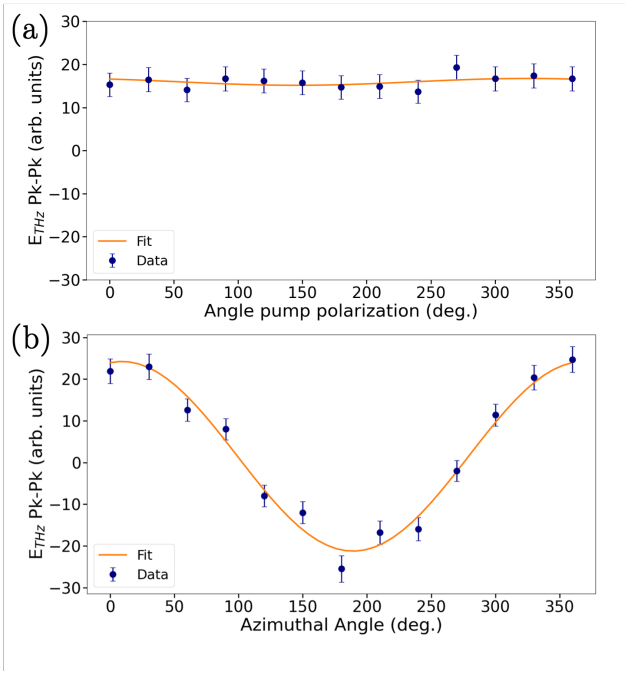

Figure 3.9: **(a)** THz Pk-Pk amplitude as a function of the angle of the incident (linear) polarization. **(b)** THz Pk-Pk amplitude as a function of the sample azimuthal orientation.

3.6.2 X-ray Diffraction

To obtain information on the crystallinity of the sample, we performed 2D x-ray diffraction measurements. The resulting diffraction pattern contains information about the orientation of the crystallites because it captures different rotation angles of such crystallites. Each crystallite contributes to the diffraction intensity in one point of the surface of a cone, which is defined by the diffraction angle. If all crystallites were oriented in the same way with respect to the substrate, we would obtain a diffraction pattern consisting of spots. Only if there is a very large number of randomly oriented crystallites, as there is in a polycrystalline thin film, there is homogeneously distributed intensity across the full surface of the cone, and a 2D cut gives continuous rings without intensity variations in reciprocal space. This description can be clarified by looking at figures 2,3 and 4 of[86]. Figure 3.10 reports the grazing incidence X-Ray diffraction pattern obtained from a 20 nm Ru film. The black line corresponds to the experimental data, the red lines are peak position retrieved from the Materials project for Ru (mp-33) from database version v2022.10.28.,

DOI:10.17188/1206459. The diffraction pattern corresponds to polycrystalline ruthenium with no preferential crystal orientation. We can therefore exclude that the preferential direction observed in the THz polarization is caused by a preferential orientation of the crystallites in the sample.

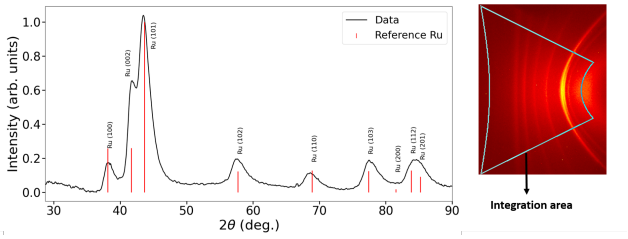

Figure 3.10: Grazing incidence XRD pattern obtained from a 20 nm Ru film on a glass substrate (left) extracted from the 2D-diffraction pattern (right).

3.6.3 AFM of Ru on sapphire

Figures 3.11 are AFM images obtained from 8 nm Ru on Sapphire before annealing (a) and after annealing (b) at 350 °C in a 10-3 mbar O2 atmosphere for 30 minutes. Comparing figure 3.11 with the figure 3.8(a) we notice a lower density of nanoprotrusions, with a lower height for Ru on sapphire than on glass. Similarly, comparing figure 3.11(b) with figure 3.8(b), corresponding to the annealed samples, Ru on sapphire shows less and lower protrusions than glass. Since we observed azimuthal-angle dependence in THz emission from the sample after annealing at 350 °C but not before annealing, we believe that the height and/or density of nanoprotrusions in the as-deposited sample is not sufficient to introduce the anisotropic surface-parallel component of THz emission. It is instead sufficient to introduce this polarization component after annealing.

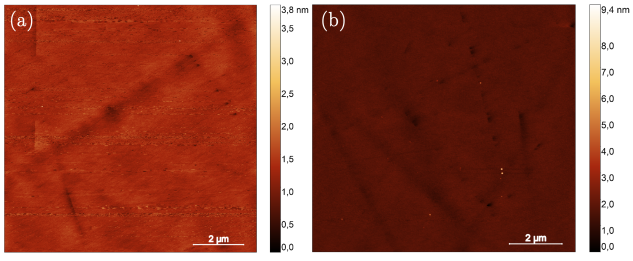

Figure 3.11: AFM images of an 8 nm Ru layer on sapphire. **(a)** As-deposited not-annealed sample. **(b)** Sample annealed at 350 °C in a 10^{-3} mbar O_2 atmosphere for 30 minutes.

4

Direct Laser Patterning of Ruthenium Below the Optical Diffraction Limit*

A method that can be used to produce ruthenium/ruthenium oxide patterns starting from a ruthenium thin film is described. The method is based on highly localized oxidation of a small surface area of a ruthenium film by means of exposure to a pulsed laser under ambient conditions. Laser exposure is followed by dissolution of the un-exposed ruthenium in a NaClO solution, which leaves the conductive, partially oxidized ruthenium area on the substrate. Spatially selective oxidation, material removal and, by implication, patterning, is therefore achieved without the need for a photoresist layer. Varying the exposure laser parameters such as fluence, focus diameter and repetition rate allows us to optimize the process. In particular, it enables us to obtain circular Ru/RuO_2 islands with a sub-diffraction-limited diameter of about 500 nm, for laser exposure times as short as 50 ms. The capability to obtain such small islands suggests that heat diffusion, in this case, is not a limiting factor to pattern Ru by laser heating on a (sub-)micron scale. In fact, heat diffusion helps in that it limits the area where a sufficiently high temperature is reached and maintained for a sufficiently long time for oxidation to occur. Our method provides an easy way to produce metallic Ru/RuO_2 (sub-)micron structures and has possible applications in semiconductor manufacturing.

*This chapter was published in a slightly modified form as: Applied Physics Letters, 124, 171902, (2024)

4.1 Introduction

In recent years ruthenium (Ru) has appeared as a promising candidate to replace more conventionally used metals such as Cu and W in semiconductor device manufacturing [87,88,89]. A prerequisite for many applications in this field is the capability to produce patterned Ru structures on (sub-)micrometer scales. In optical lithography, structures are usually created by first applying patterned illumination of a photoresist layer deposited onto a substrate. Subsequent removal of the exposed regions of the resist, followed by material deposition, etching and other steps, are needed to create the pattern [8]. Other methods to fabricate patterns are e-beam lithography [90], electron beam induced deposition [91], selective area atomic layer deposition [92,93] or rheology printing [94].

Here, we show how direct laser writing can be used to pattern Ru without the need for a photoresist. In this method, ultrashort laser pulses are focused to a small spot on a Ru thin film under ambient conditions. Partial absorption of the light by the Ru increases the local temperature and locally oxidizes the surface of the film. Subsequent etching of the layer using a NaClO solution removes the Ru except in the areas where the surface of the layer has been (partially) oxidized. We find that after exposure times as short as 50 ms, we can fabricate Ru/RuO_2 islands with diameters as small as 500 nm. This is three to four times smaller than the focal diameter of the laser beam and in fact below the diffraction limit of the optical system. From an application perspective, this capability is particularly interesting for the semiconductor manufacturing industry. Creating these structures requires that the local thermal energy at the Ru surface is larger than the threshold energy needed for oxidation for a sufficiently long time. By adjusting the laser pulse energy, reaching this threshold energy can be limited to the most central part of the Gaussian spatial beam profile, thus creating oxidized areas significantly smaller than the full width at half maximum of the focused beam. Our method constitutes a very simple technique for producing Ru/RuO_2 structures with sub-diffraction limited features.

4.2 Methods

The ruthenium thin films were deposited by magnetron sputtering at an argon plasma pressure of 2×10^{-3} mbar. Both glass and silicon were used as substrates. The substrates were chemically cleaned using a solution of ammonium hydroxide (NH_4OH) with hydrogen peroxide in water and, after that, rinsed in isopropanol.

The calculated penetration depth of light for ruthenium on glass, as well as absorbed and reflected fractions of 800 nm and 1030 nm light are provided in appendix 4.5.1.
The Ru/RuO_2 islands were fabricated by first exposing the ruthenium samples to laser light. Subsequently, the samples were immersed in a 3-7% NaClO solution in water. This step causes the un-exposed ruthenium to dissolve, leaving the areas partially oxidized by the laser on the substrate. After that, the samples were first rinsed in demineralized water, and subsequently in isopropanol to facilitate the drying.

4.3 Results

Figure 4.1(a) is a scanning electron microscopy (SEM) image of a Ru/RuO_2 island obtained by exposing a 50 nm thick Ru-on-silicon sample to a 70 fs, 800 nm wavelength 5.2 MHz repetition rate laser for 15 s, focused to a diameter of about 8 μm. The sample was then rinsed in the NaClO solution for 720 s. We found that a minimum rinse time is required to remove the Ru layer and that longer times are necessary for thicker films. However, once the un-exposed layer is dissolved, rinsing for times up to several hours does not have a significant influence on the island. The island shown in figure 4.1(a) has an approximately round shape and a small diameter of approximately 9 μm.
In figure 4.1(b) we show a photograph of a set of large Ru/RuO_2 islands obtained with a weakly focused laser beam. The islands have a shiny metallic look and the surrounding area of the glass substrate appears clean.
We chemically characterized the islands by performing X-ray photoelectron spectroscopy (XPS). This was done on a large island obtained from an 8 nm thick Ru sample on glass, exposed to the laser and rinsed in NaClO. The results (appendix 4.5.2) show that our method produces a partially oxidized Ru film, similar to the one we described previously (chapter 3)[95]. This film is a partially oxidized Ru layer in which the oxide is in the rutile phase. By extracting the average oxide thickness from the XPS measurements using the flat overlayer approximation[96] we found that oxide thicknesses as low as 2.4 nm are already sufficient to prevent the laser-exposed area from being removed by the NaClO solution. If the same measured XPS intensities are used within the hypothetical high-roughness limit of Ru/RuO_2 core-shell particles[97] assembled into a layer, this number decreases to 1.4 nm. It is possible that even thinner rutile-phase RuO_2 layers may prevent etching of the Ru in the NaClO solution, but this has not been tested
To gain information on the island-formation process, and to find the optimal exposure

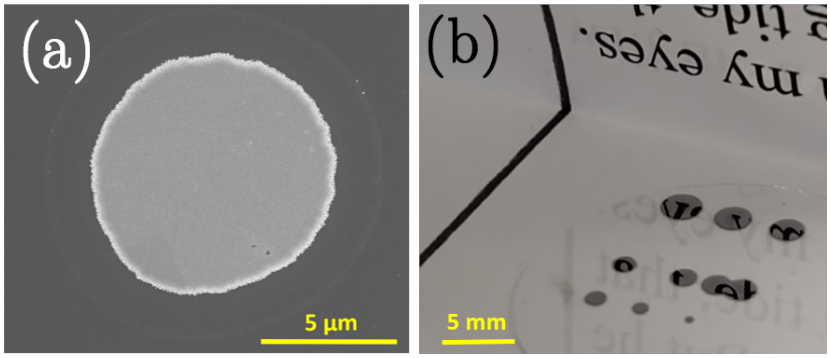

Figure 4.1: (a) SEM image of an island obtained with the 5.2 MHz repetition rate laser focused to a spot with a diameter of about 8 μm. This island has a diameter of approximately 9 μm. (b) Photograph of a set of Ru islands on a glass substrate, placed on a piece of paper with a rectangular fold, illustrating the high optical reflectivity of the islands.

parameters to create the smallest spots, Ru layers with a thickness of 8 and 20 nm on a glass substrate were exposed to the same 5.2 MHz-repetition rate laser at different fluences. Throughout this chapter, fluence is defined as the *single-pulse* energy divided by the FWHM area of the laser spot, although exposure is performed with multiple pulses. After exposure, the samples were rinsed with the NaClO solution for 90 s (8 nm) and 210 s (20 nm).

Optical microscopy images of two islands obtained on these samples after exposure to a 9.5 mJ/cm^2 fluence are shown in figure 4.2(a). The observed diameter is approximately 16 μm for the 8 nm film and 13 μm for the 20 nm film. The island obtained from the 8 nm film does not have sharply defined edges. This is also the case for the islands obtained with higher exposure fluences, which results in larger error bars for the areas extracted from this sample.

To learn more about the process resulting in the formation of Ru/RuO_2 islands, we performed a Liu analysis [45] (also described in chapter 2, section 2.3.2). This analysis is valid for laser-induced processes occurring at fluences exceeding a certain threshold and when the laser beam profile is gaussian. Often, in these cases, the area of a laser-induced material modification scales linearly with the natural logarithm of the fluence. When these conditions are satisfied, it is possible to extract the threshold fluence at which the islands are formed by extracting the fluence level where the island area is zero from a linear fit to the data.

The Liu plots, obtained from optical microscopy images similar to the ones shown in figure 4.2(a), are shown in figure 4.2(b). For both the 8- and the 20-nm thick films, the figure

clearly shows that the area of the islands does not scale linearly with the logarithm of the exposure fluence. The vertical lines in the plot indicate the fluence beyond which optical microscopy images show a darker region in the center of the island. This was identified as an ablated region. The lines are located at a fluence of 17 mJ/cm^2 for the 8 nm thick film and 23 mJ/cm^2 for the 20 nm thick film. We note that melting can already occur at fluence levels somewhat below the damage threshold. The effect of melting on the formation of the oxide is at present unknown. Understanding the effect of ruthenium melting on the island formation process is an interesting question. However, given the high melting temperature of ruthenium (2 603 K) it might not be as relevant from an application point of view as it increases the risk of damaging the material underneath the ruthenium and is therefore beyond the scope of this chapter. Fluences below the range reported in figure 4.2(a) were also tested, but no islands were observed. This applies also to the other Liu plots presented in this work.

Since the spots obtained for thicker films produced more uniform and smaller islands, we also tested our method on 50-nm-thick Ru samples for two different exposure times: 5 s and 15 s. After exposure, the samples were rinsed in the NaClO solution for 390 s. Note that the thickness of 50 nm was chosen more or less randomly, and for applications in the semiconductor manufacturing industry, it would also be interesting to test our method with even thicker films, up to 100 nm, although we expect to obtain similar results.

Selected microscopy images of islands are shown in figure 4.2(c) for both exposure times. These islands were obtained with an exposure fluence of 9.5 mJ/cm^2. Their diameters are 7 μm (5 s exposure) and 9 μm (15 s exposure), close to the illumination spot size ($\sim$ 8 μm). The Liu plots obtained for the 5 s (red) and 15 s (black) exposure times are shown in figure 4.2(d). Both curves are similar to the ones obtained for the 8 nm and 20 nm samples, showing a super-linear dependence on the logarithm of the exposure fluence. For each fluence, the red curve indicates that, overall, a 5 s exposure leads to smaller areas than the ones obtained with the 15 s exposure.

The non-linearity of the Liu plots is an indication that in-plane heat transport may affect the island size. Additional evidence of in-plane heat transport is the observation of islands with an area much larger than the laser spot size, at high exposure fluences. Optical microscopy images of such areas, with a diameter of approximately 80 μm (ten times larger than the exposure spot diameter), are shown in appendix 4.5.3.

The above suggests that varying the number of laser pulses, as well as the time interval between them, has an influence on the formation of the Ru/RuO_2 islands. Furthermore, smaller islands could be achievable by tighter focusing. For this reason, we tested our

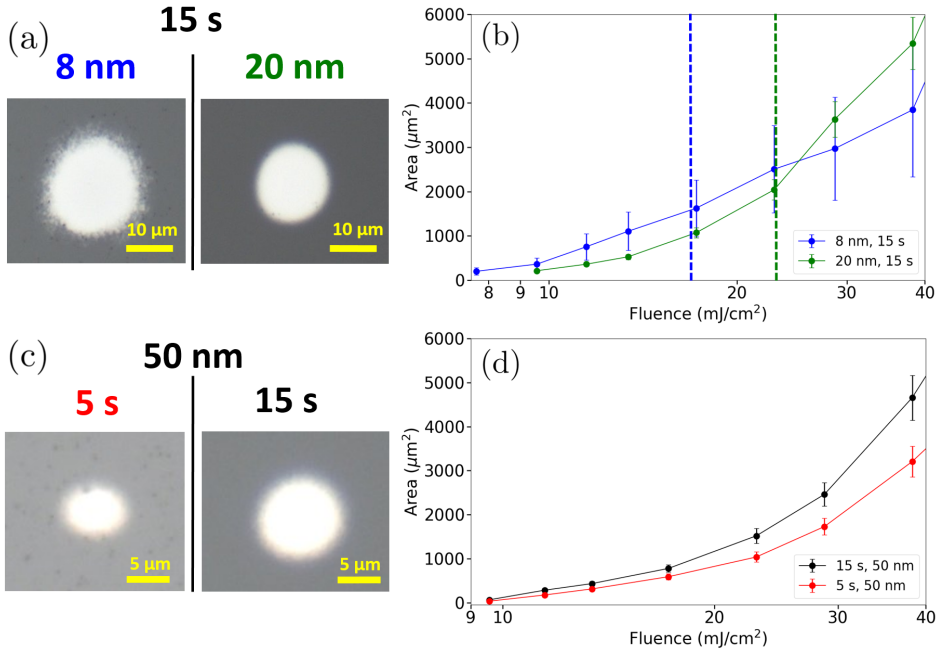

Figure 4.2: (a) Optical microscopy images of the islands relative to the Liu plot in the sub-figure (b). (b) Liu plot of the RuO_2/Ru islands obtained after 15 s exposure of 8 nm (blue) and 20 nm (green) Ru films on glass to the high repetition rate, 800 nm laser. The dashed vertical lines correspond to the measured ablation thresholds. (c) Optical microscopy images of the islands relative to the Liu plot in the sub-figure (d). (d) Liu plot obtained from a 50 nm Ru film on glass exposed for 15 s (black) and 5 s (red) to the high repetition rate, 800 nm laser.

method with a lower repetition rate laser capable of generating a variable number of pulses. The laser delivers 200 fs pulses at a 1030 nm central wavelength with a repetition rate of 200 kHz. This source was focused onto the sample to spots with a diameter of approximately 2 μm. This system is described in more detail elsewhere [98].

Figure 4.3(a) is an optical microscopy image of a typical grid of islands obtained using the aforementioned illumination system on a 50 nm Ru film on glass. Each spot was exposed to different numbers of laser pulses at a (single-pulse) fluence of 18.2 mJ/cm^2. The number of pulses increases in a "meandering" fashion from the top-right corner of the image to the bottom-right one and is varied from 1 to 50 000. The islands are remarkably small: most of them have sub-micrometer diameters and none of them exceeds the illumination spot size by more than a few percent.

The size of one the smallest islands that we could obtain with the low repetition rate laser is estimated by performing SEM. In addition, this allows to characterize the island morphology. As SEM on glass is complicated by charge accumulation, we fabricated islands on a 50 nm Ru film on silicon, for which charging is not an issue.

A typical SEM image of one of the smallest islands that we obtained is shown in figure 4.3(b). The central Ru/RuO_2 region has an exceptionally small diameter of approximately 500 nm, four times smaller than the diffraction limit of the objective used to focus the laser. The central area is surrounded by an additional region having a different appearance and approximately the same diameter as the illumination beam.

In an attempt to identify the content of the region surrounding the central island, we performed energy-dispersive x-ray spectroscopy (EDX) [36]. The results, presented in appendix 4.5.4 show the presence of Ru but no other potential contaminants such as sodium or chlorine. We note that this region is not affected by additional rinsing in the NaClO solution or by varying the NaClO concentration between 2-5% and 6-14%.

To learn more about a typical Ru/RuO_2 island morphology and to determine the amount of under-etching, we performed cross-sectional SEM imaging on an island obtained from a 50 nm thick Ru film on Si, exposed to the 200 kHz laser focused to a 2 μm spot size. This was done by first depositing a layer of platinum over the island and by subsequently removing a section of the island with a focused ion beam (FIB). The Pt layer facilitates the attainment of sharp edges in the FIB cut. The resulting image, recorded by orienting the sample at an angle of 52° with respect to the detector, is shown in figure 4.3(c). The island has a $\sim$2 μm diameter and a flat cross section. Figure 4.3(d) is the high magnification image of the area inside the yellow square in figure 4.3(c). Here, it can be seen that the under-etching is limited to a distance from the edge of $\sim$35 nm.

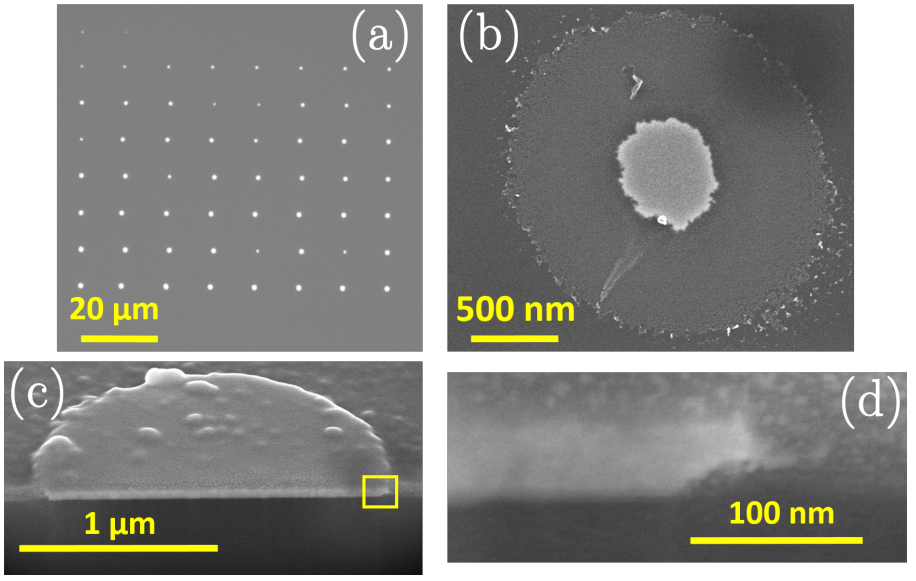

Figure 4.3: (a) Optical microscopy image of a grid of Ru/RuO_2 islands on silicon obtained with a 2 μm beam diameter of the 200 kHz repetition rate, 1030 nm laser. (b) SEM image of a typical island. (c) Cross sectional SEM of an island viewed at an angle of 52°. (d) Detail of the region highlighted by the yellow square in image (c), showing that the amount of under-etching is limited to a distance of ~35 nm from the edge of the island.

Liu plots of the islands obtained by exposing 50-nm-thick Ru films on glass to different numbers of laser pulses from the 200 kHz repetition rate laser are shown in figure 4.4(a). The areas of the islands were extracted from optical microscopy images similar to the one shown in figure 4.3(a). Since the island size, in this case, is close to the resolution limit of the optical microscope, the resulting areas have large error bars. Unlike the case of exposure to the 5.2 MHz repetition rate laser (figure 4.2), the areas now depend approximately linearly on the logarithm of the exposure fluence. Furthermore, at a given fluence, the island area increases with an increasing number of pulses. In this case, the fluence range was fine tuned in order to include fluences high enough for island formation for many different numbers of pulses, while keeping the fluence below the ablation threshold. This results in a narrow fluence interval. The linearity of the Liu plots over a broader fluence range is confirmed in appendix 4.5.5.

The effect of exposure to different numbers of pulses is further examined by performing a linear fit on a large set of Liu plots, similar to those of figure 4.4(a) and by extracting the intercepts with the x-axis. This value corresponds to the (single-pulse) oxidation threshold-fluence F_0, which is then plotted as a function of the number of pulses in figure 4.4(b). This

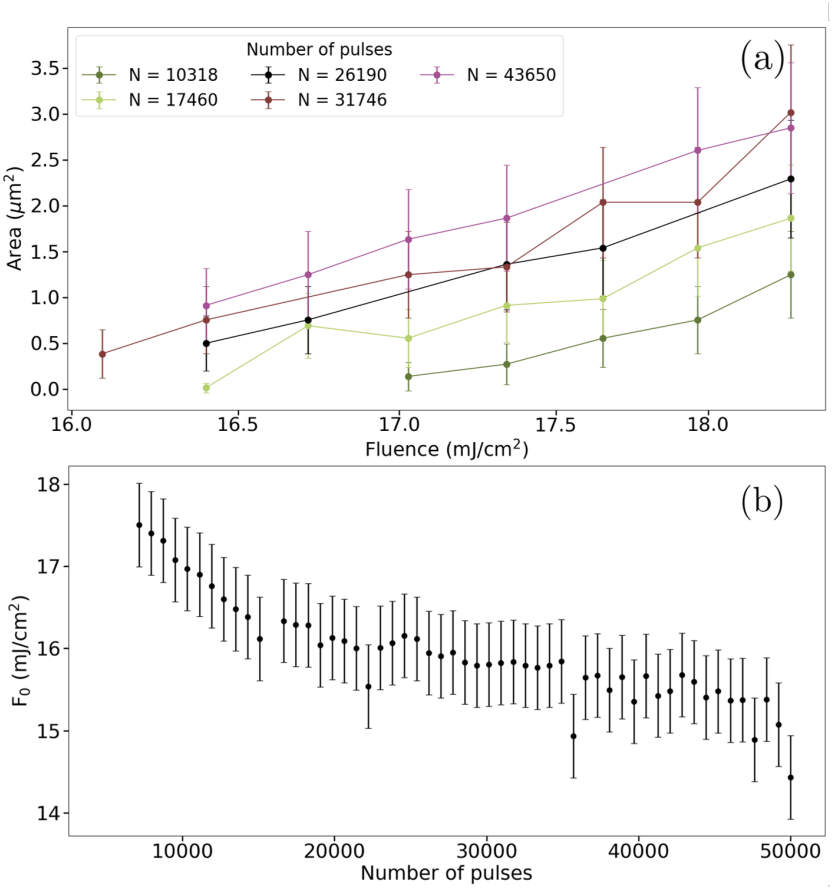

Figure 4.4: (a) Liu plot obtained from a 50 nm Ru film on glass exposed to the 200 kHz repetition rate laser for different number of laser pulses. (b) Threshold fluences for islands formation (F_0) as a function of number of pulses. This quantity is obtained from the intercepts with zero from the Liu plots similar to the one in figure (a).

shows a modest linear decrease of F_0 from a value of 17.5 ± 0.5 mJ/cm^2 for approximately 7 000 pulses, down to a value of 16.1 ± 0.5 mJ/cm^2 for 16 000 pulses. From here, it keeps decreasing, although with a lower slope. The cumulative effect of exposure to multiple laser pulses, therefore, becomes less important for $N \gtrsim 16\,000$. We note that 10 000 pulses corresponds to a total exposure time of 50 ms.

To confirm that our process produces electrically conductive samples, we measured the sheet resistance of an oxidized sample rinsed in the NaClO solution, using the four-point probe van der Pauw method [99] and compared it with an as-deposited Ru sample, which has a sheet resistance of 4.3 Ω/sq. Oxidation was performed in a oven, in order to oxidize the whole sample, which is necessary for the four-point probe measurement, at 350 °C at a 10^{-4} mbar O_2 atmosphere for 75 minutes. The sample was then rinsed in the NaClO solution for 390 s. In this case, we obtained a sheet resistance of 8.6 Ω/sq: only a two-fold increase with respect to the pristine Ru sample. This result shows that partial oxidation and subsequent immersion in the NaClO solution does not cause a dramatic increase in resistivity and produces conductive samples.

4.4 Discussion and Conclusion

For both high- and low-repetition rate lasers we observed the effect of multiple-pulse exposure: with the 5.2 MHz repetition rate, we found non-linear Liu plots and islands with an area largely exceeding the illumination spot size; with the 200 kHz repetition rate laser we observed a dependence of the oxidation threshold fluence on the number of laser pulses. All of these effects could either be due to a (high) temperature increase resulting from multiple pulse heat accumulation in combination with in-plane heat transport, by an accumulation of (single-pulse) oxidation steps, or by a combination of the two.

Heat accumulation is most likely to occur with the 5.2 MHz repetition rate system due to the short time interval between the pulses (192 ns) and the relatively long exposure times (5 to 15 s). In this case, after each laser pulse, the illuminated area does not return to room temperature before the arrival of the next one. This results in a high temperature increase which, together with in-plane heat transport, produces a super-linear growth of the (partially) oxidized area as a function of the logarithm of single-pulse exposure fluence, as observed in figure 4.2.

The aforementioned mechanism is less likely to apply to the case of the 200 kHz repetition rate laser. In this case, the Liu plots are approximately linear (figure 4.4(a)) and the island

area does not exceed the exposure area as dramatically. The accumulation effect manifests itself as an increase in the island area at a fixed exposure fluence, for an increasingly higher number of pulses, as well as a modest decrease of the threshold fluence F_0 (figure 4.4(b)). We attribute these features to accumulation of oxidation: each laser pulse oxidizes a fraction of the thickness of the illuminated area. The minimum fluence necessary to oxidize a thick enough layer to prevent dissolution in NaClO therefore depends on the number of laser pulses. This process results in a linear dependence of the island area on the logarithm of the exposure fluence as in-plane heat transport does not seem to increase the island size dramatically.

In conclusion, we have demonstrated a method for producing conductive Ru/RuO_2 islands. We obtained islands with a diameter as small as 500 nm using a 2 μm beam diameter at a wavelength of 1030 nm. Our method can produce sub-diffraction limited island sizes, which is somewhat surprising for a thermally-driven process. We note that, in principle, once the sub-diffraction-limited Ru/RuO_2 patterns are obtained, the RuO_2 can be reduced back to Ru by exposure to reducing agents such as hydrogen gas at high temperatures[100,101]. Smaller features may be obtained by further fine tuning parameters such as laser wavelength, beam size and exposure time. Finally, we note that laser-induced oxidation should be taken into account in the interpretation of pump-probe measurements on Ru[95,102,11] and, possibly, on other metals as well[103]. Our measurements shed some light on the circumstances under which this can occur.

4.5 Appendices

4.5.1 Penetration depth and fraction of absorbed and reflected light for ruthenium on glass

The complex refractive index (n, k) of Ru, obtained using ellipsometry, was found to be (5.271, 5.106) at 800 nm, and (4.925, 5.020) at 1030 nm. The latter values were taken to be the same as those at a wavelength of 1000 nm, the longest wavelength present in the ellipsometer data. Considering the small difference with the actual used wavelength of 1030 nm, corrections to these values are most likely to be smaller than a few percent. From these values, we can calculate the bulk optical power penetration depth in the ruthenium. We find a value of 12.5 nm at a wavelength of 800 nm, and 16.4 nm at a wavelength of 1030 nm. Note that when the Ru layer thickness becomes on the order of the penetration depth or less, interference caused by reflections inside the Ru layer can have a significant effect

on the total reflection and absorption. To quantify this, we have performed multilayer calculations to calculate the fraction of absorbed and reflected light at 800 nm and at 1030 nm, for Ru on glass, with Ru thicknesses of 8, 20 and 50 nm. The results are shown in Table 4.1. Note that because of the interference inside the layer, the absorbed optical power has an oscillatory component as a function of the layer thickness, explaining the increase in absorption when decreasing the Ru thickness from 50 nm to 8 nm.

Table 4.1: Absorption and reflection fraction for 800 nm and 1030 nm light illumination for ruthenium on glass. Note that the reflected and absorbed fractions don't have to add up to 1 as some light is also transmitted.

Ruthenium thickness (nm)	8	20	50
Fraction absorbed (800 nm)	0.40	0.30	0.31
Fraction reflected (800 nm)	0.43	0.65	0.69
Fraction absorbed (1030 nm)	0.40	0.34	0.30
Fraction reflected (1030 nm)	0.36	0.59	0.69

4.5.2 X-ray photoelectron spectroscopy

In this section we present XPS measurements performed on a pristine, as-deposited, 8 nm thick Ru sample, and on a sample obtained after exposure to the 5.2 MHz repetition rate laser and immersion in the NaClO solution. Both samples were deposited on glass. Before laser exposure, the Ru thickness was 8 nm.

The XPS spectra are shown in figure 4.5. The black curve (vertically displaced) is the one obtained from the as-deposited Ru sample. The spectrum shows the characteristic peaks of Ru (highlighted in the figure) and the oxygen 1s peak at 530 eV. The latter is due to the sub-nanometer native oxide layer forming upon contact with the atmosphere [77].

The red curve in figure 4.5 is the spectrum obtained from the sample exposed to the laser and rinsed in the NaClO solution. This curve shows peaks at the same binding energy as the ones visible in the black curve. The spectra only differ in the relative height between the Ru peaks and the O 1s peak, as a result of laser-induced oxidation.

These results demonstrates that laser exposure results in partially oxidized Ru films and that rinsing in the NaClO solution does not introduce appreciable contamination.

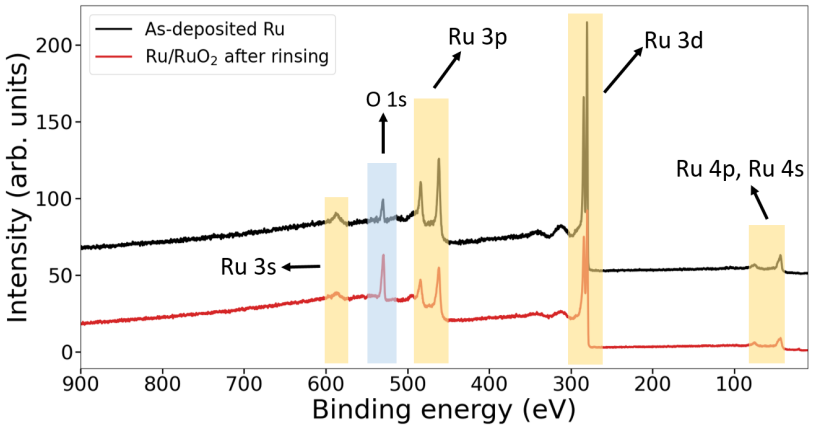

Figure 4.5: XPS spectra obtained from an as-deposited Ru sample (black, vertically displaced) and from a sample exposed to the 5.2 MHz laser and rinsed in the NaClO solution (red).

4.5.3 Islands largely exceeding the illumination diameter

Here, we show two examples of optical microscopy images of Ru/RuO_2 islands obtained by exposing a 50 nm thick Ru film on glass to the 5.2 MHz repetition rate laser focused to a spot with a 8 μm diameter. The exposure fluence is 33 mJ/cm^2. After exposure, the samples were rinsed in the NaClO solution for 390 s. Figure 4.6(a) shows an island obtained with a 5 s exposure. This island has a diameter of approximately 70 μm. The island shown in figure 4.6(b) was obtained with a 15 s exposure time and has a diameter of approximately 80 μm. The dark region visible in the center of both islands corresponds to a region where the ruthenium was ablated due to the high local fluence reached in the center of the gaussian beam.

The fact that we could obtain islands with a diameter approximately ten times larger than the beam diameter is a clear indication of the presence of in-plane heat transport.

4.5.4 Energy-Dispersive X-ray Spectrometry

In this section we present the elemental characterization of an island resulting from Energy-Dispersive X-ray Spectrometry (EDX) measurements[36]. The measurements were performed on an island obtained from a 50 nm thick Ru film deposited on silicon, exposed to the 200 kHz repetition rate laser and rinsed in NaClO for 720 s.

Figure 4.7(a) is an SEM image of the inspected island. It shows a central bright region with a diameter of approximately 500 nm, surrounded by an additional rim located approxi-

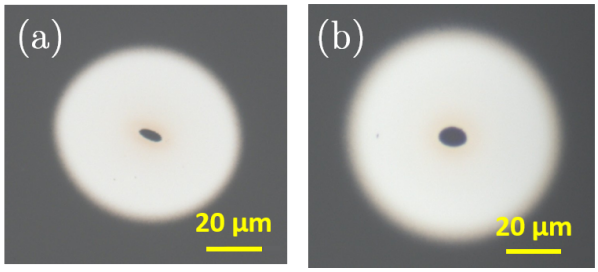

Figure 4.6: Examples of islands with diameters largely exceeding the illumination beam diameter. (a) Island obtained with a 5 s exposure time. (b) Island obtained with a 15 s exposure time.

mately 1 μm from the center.

Figure 4.7(b) shows the EDX signal of Ru as a function of position x, integrated over y in the area imaged in figure 4.7(a), over the range indicated by the vertical red lines on the left and right sides of the image. As expected, it clearly shows a peak corresponding to the island at a position around 1.8 μm.

Figure 4.7(c) is the high-magnification image of the area in the yellow rectangle of figure 4.7(a), showing the outer rim running vertically, approximately in the center of the image. Figure 4.7(d) is the Ru signal as a function of position x integrated over the vertical direction y in figure 4.7(c). It shows a small Ru signal, decreasing when moving from left to right. The Ru signal is very small, due to a the near absence of Ru (as is clear from figure 4.7(b)). The decrease in the Ru signal stops at a position around 2.6 μm, close to the rim delimiting the region surrounding the main Ru/RuO_2 island. We therefore conclude that the area immediately around the islands in figure 4.3 and in figure 4.7(a) contains traces of ruthenium.

In figure 4.8 we show the EDX signals corresponding to Ru, Cl, C and Na. The figure suggests the presence of chlorine in correspondence with the Ru signal. However, independent chlorine detection was hampered by the fact that the chlorine $K\alpha^1$ line overlaps with the Ru $L\alpha^1$. This was verified independently in a control experiment on an un-treated as-deposited Ru sample. The observations are consistent with the absence of chlorine.

The map describing the carbon distribution shows some presence of carbon on the Ru/RuO_2 island. XPS measurements on pristine Ru showed the presence of 0.3 nm of carbon which grew to 2 nm after exposure to the laser. XPS measurements after etching with an NaClO solution showed again a carbon thickness of 0.3 nm, similar to that of the pristine layer. NaClO is known to remove carbon and the 0.3 nm observed after etching is almost certainly deposited after exposure to ambient atmosphere again.

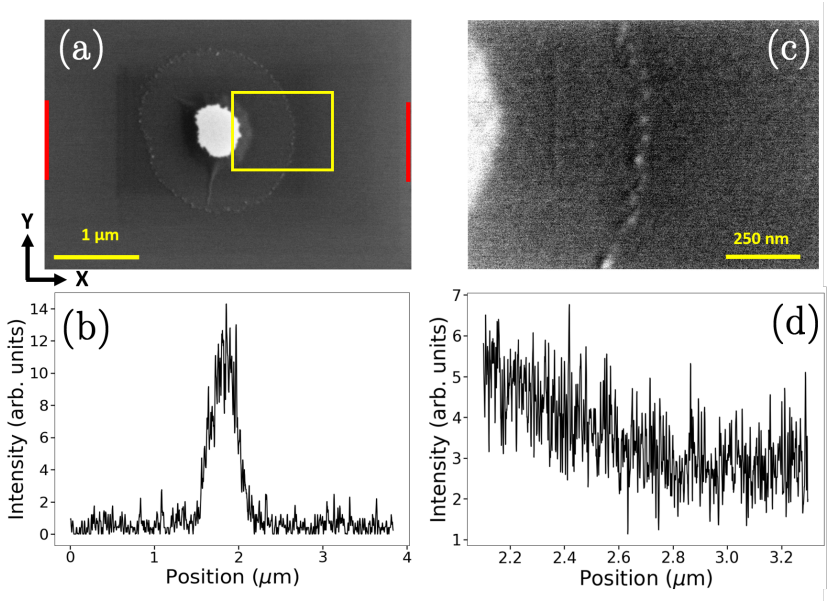

Figure 4.7: (a) SEM image of a Ru/RuO_2 island. The vertical red lines indicate the region over which the rows of pixels are summed to obtain the plot of figure (b). (b) EDX signal from Ru integrated over the vertical direction of the region shown in figure (a). (c) High magnification SEM image of the area enclosed in the yellow square in figure (a). (d) EDX signal from Ru integrated over the vertical direction of the region shown in figure (c).

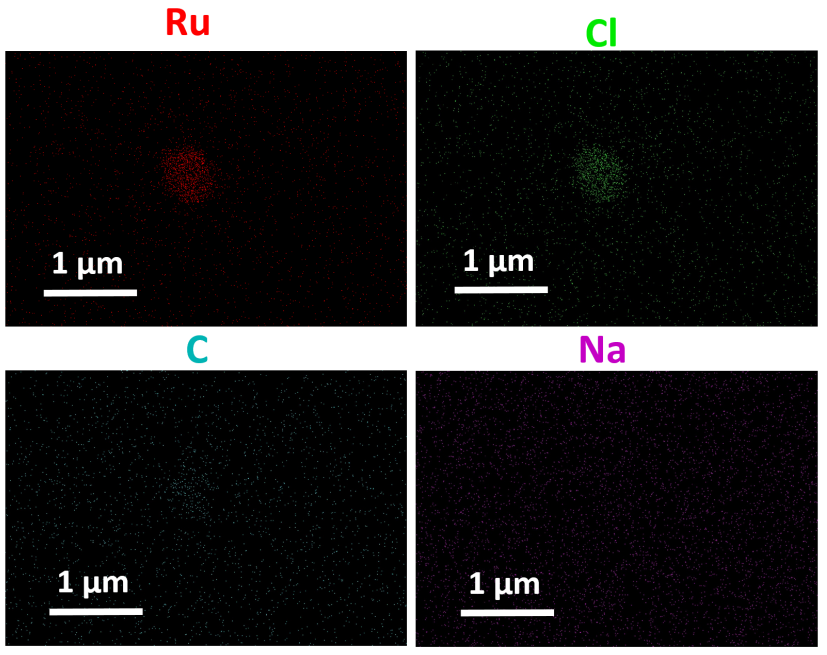

Figure 4.8: EDX signal of the elements indicated above each map obtained from the same region imaged in figure 4.7(a).

The EDX map of Na does not show the presence of this element on the sample.

4.5.5 Linearity of Liu plots over an extended fluence range

In this section, we show an example of a Liu plot obtained by exposing a 50 nm Ru film on Si to 25 000 laser pulses at a 200 kHz repetition rate. The laser, similarly to the case of figure 4.4(a), was focused onto the sample to a spot with a 2 μm diameter.
The Liu plot, shown in figure 4.9, does show an approximately linear dependency of the island area with the logarithm of the exposure fluence. This result therefore supports the observation of figure 4.4(a).

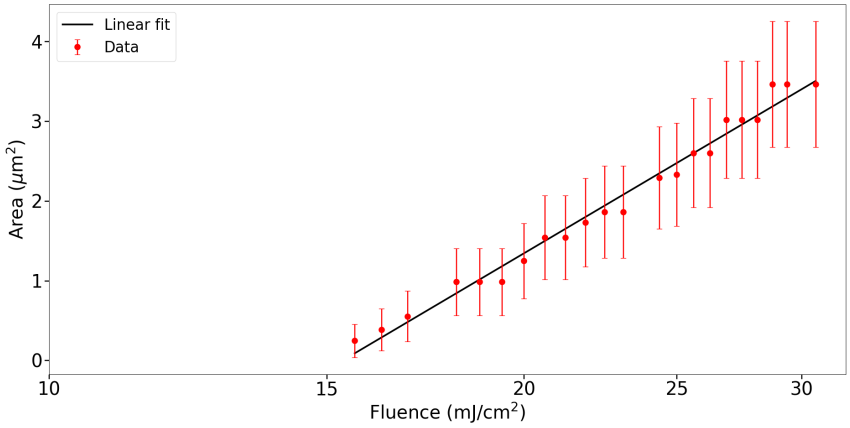

Figure 4.9: Liu plot obtained by exposing a 50 nm thick Ru film on Si to 25 000 pulses at a 200 kHz repetition rate. The fluence range is broader than the one used in figure 4.4(a), demonstrating the linearity of the dependence of the island area on the logarithm of the exposure fluence.

5

Effect of Substrate and Beam Diameter on Direct Laser Patterning of Ruthenium Thin Films*

In chapter 4, a method was introduced to produce ruthenium/ruthenium-oxide electrically conductive islands through laser-induced oxidation of ruthenium thin films, followed by subsequent removal of the un-oxidized ruthenium using a NaClO solution. In this chapter, additional insight in the patterning process by measuring the effect of Ru film thickness and substrate material on the pattern formation is provided. In particular, understanding the role of the substrate, which affects the island formation mainly through the Ru film-substrate interfacial thermal conductance, is crucial. Experimental results and numerical heat diffusion calculations are used for comparing the island formation process when using a 2 μm exposure beam diameter and a 0.8 μm one. It is shown that in-plane heat diffusion results in a faster decay of the surface lattice temperature of the film after exposure to the 0.8 μm beam diameter. Although exposing the samples to a smaller beam diameter could, in principle, enable obtaining patterns with smaller features, in-plane heat diffusion may be the limiting factor for the smallest achievable features that can be obtained using this method.

*This chapter was submitted to *Optical Materials Express*

5.1 Introduction

In recent years, novel materials have been investigated with the goal of improving the performance of semiconductor devices[104,105]. Among these, ruthenium has raised interest due to its relatively high nanoscale electrical conductivity resulting from the small grain sizes[106,107]. In addition, Ru and RuO_2 are suitable for applications in semiconductor manufacturing thanks to their chemical and thermal stability[108,109,110], both of which are beneficial for the lifetime and the performance of devices. Ruthenium being a relatively unknown material, it is worth pointing out a number of interesting properties, such as the high melting point of Ru (2 583 K), and the fact that the oxide RuO_2 is also metallic. Recently we described a method for patterning Ru based on laser-induced oxidation of Ru thin films[111]. In short, exposure to femtosecond (fs) laser pulses results in a temperature increase of the Ru film. When the temperature exceeds a certain threshold, a less than 2 nm thick layer near the surface of the film is partially oxidized. By focusing a beam with a gaussian spatial profile and by tuning the exposure fluence, repetition rate and exposure time, it is possible to limit oxidation to the most central region of the beam. The un-exposed Ru is dissolved using a NaClO solution, while the top layer of RuO_2 prevents dissolution of the exposed region, such that the Ru pattern with a thin conductive RuO_2 top layer remains. Using a fs pulsed exposure laser with a 1030 nm wavelength, focused to a spot with a 2 μm diameter this method allowed us to obtain islands with a diameter of approximately 500 nm: four times smaller than the beam diameter and therefore below the optical diffraction limit of the system used for illumination.

Here, we further explore our patterning method with the aim of providing additional insight into its applicability. We explore the effect of Ru film thickness, correlating it with the exposure fluences necessary to produce the patterns. We calculate the absorption of Ru as a function of the film thickness, which shows a weak dependence for thicknesses above approximately 8 nm. We find that the threshold fluence necessary to produce Ru/RuO_2 islands from 20 nm and 50 nm thick films, scales with the film thickness. This suggests that the fluence needed for applying this method to different film thicknesses may simply be predicted from the film thickness, as long as the film is homogeneously heated over its thickness.

The role of the substrate material underneath the Ru is studied by comparing the island formation process on three different substrates: glass, sapphire and silicon. We extract similar threshold fluences for sapphire and silicon, regardless of their different thermal conductivities. This suggests that the Ru/substrate interfacial thermal conductances (ITC) for the

three substrate materials play a crucial role in slowing down heat transport into the substrates.

Results obtained with different exposure beam diameters are compared both by measuring the island-formation threshold fluence as a function of the number of pulses used for exposure and by numerical simulations of heat diffusion. This shows that, after exposure to a 0.8 μm beam diameter, in-plane heat transport results in a faster decay of the lattice surface temperature, compared to exposure to a 2 μm diameter beam. While in principle the possibility to produce patterns by means of a smaller exposure diameter would make it possible to obtain features with smaller dimension, in-plane heat transport may be the limiting factor determining the minimum achievable feature size.

5.2 Materials and methods

Ruthenium thin films were deposited via magnetron sputtering at an argon plasma pressure of 2×10^{-3} mbar. Glass, silicon and sapphire were used as substrates. The substrates were chemically cleaned using a solution of ammonium hydroxide (NH_4OH) with hydrogen peroxide in water and, subsequently, rinsed in isopropanol.

A schematic of the setup used for laser exposure is shown in figure 5.1. The laser has a

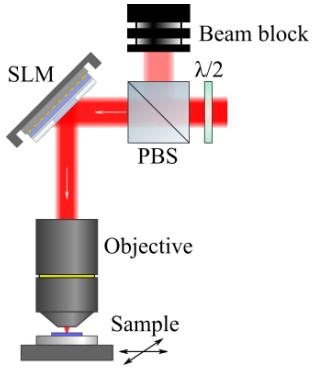

Figure 5.1: Schematics of the laser-exposure setup used for producing the laser-induced oxidation with variable beam diameter before immersion in the NaClO solution[98]. PBS: polarizing beam splitter; SLM: spatial light modulator.

1030 nm wavelength and delivers pulses with a duration of approximately 200 fs with a 200 kHz repetition rate. A half-wave plate and a polarizing beam splitter (PBS) are used to control the exposure fluence. We note that, throughout this work, we report the single-pulse fluence even when referring to exposure to multiple pulses. A reflective spatial light modulator (SLM) is used to control the diameter of the beam. This is done by forming a

blazed grating within a circular area on the SLM. This grating effectively acts as an aperture, as only the light that hits the grating will show a first order diffraction. By changing this *effective-aperture* diameter, the diameter of the first-order diffracted beam is varied. The diffracted beam is then directed to a microscope objective, which focuses it onto the sample. The beam diameter at the focus of the objective can be continuously varied between 2 μm and 0.8 μm by varying the diameter of the effective aperture of the spatial light modulator. When the aperture is fully open, the diameter of the first-order-diffracted beam is largest and it illuminates the full entrance of the objective, resulting in the smallest focal diameter of 0.8 μm. Decreasing the effective aperture diameter reduces the diameter of the diffracted beam, which results in an increased focal spot diameter.

After exposure, the samples were immersed in a 3-7% NaClO solution in water, which dissolves the un-exposed Ru and leaves only the partially oxidized areas on the substrates. After this, the samples were rinsed in demineralized water and, subsequently, in isopropanol. The Ru/RuO_2 island formation process is studied by measuring the area of the islands remaining after the aforementioned fabrication procedure, using an optical microscope. We then plot the area of the islands as a function of the logarithm of the exposure fluence of the beam. When this so called Liu plot [45] is linear, it is possible to extract the (single-pulse) threshold fluence for island formation by performing a linear fit to the data and, from this, extracting the fluence value at which the area is zero.

5.3 Results

To gain more insight into the effect of Ru layer thickness on the amount of absorbed light, we calculated the percentages of absorbed, transmitted and reflected light as a function of the Ru film thickness on glass. The calculations were performed by assuming light orthogonally incident on the sample, and using the complex refractive index $\tilde{n} = n + ik$ of Ru obtained earlier using ellipsometry, namely $\tilde{n} = 4.925 + i5.020$, obtained at 1 000 nm, the longest wavelength accessible in the ellipsometer. For glass, we used a refractive index of 1.5.

The results are shown in figure 5.2. The percentages of reflected and transmitted light approach the bulk values for thicknesses above approximately 60 nm (69% and ∼0% in the figure, respectively). The amount of absorbed light (black solid line) has a maximum of 40% for a Ru thickness of 8 nm, after which it slightly decreases to a value of 29% at a thickness of approximately 40 nm and increases again until reaching the bulk value of 33%

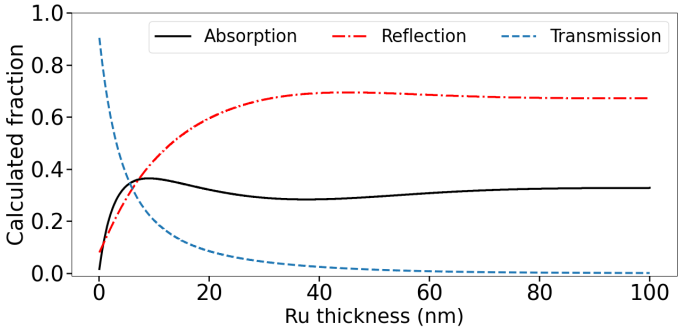

Figure 5.2: Calculated amounts of absorbed (black, solid line), reflected (red, dashed-dotted) and transmitted (blue, dashed) light with a wavelength of 1000 nm from Ru films on glass, as a function of ruthenium thickness.

around 80 nm. Below, we will show results of experiments performed on Ru layers having a thickness of 20 and 50 nm. From figure 5.2 we can see that for the 20 nm thick sample, the expected percentage of absorbed light is 34 %, whereas for the 50 nm thick layer it is about 30%. The same calculations resulting in figure 5.2 were performed for Ru on sapphire and for Ru on silicon. The refractive index of the substrates used in the calculations was 1.7557 for sapphire and $3.5757 + i4902 \times 10^{-4}$ for silicon. For both substrates, the calculations do not show large variations in the amount of absorbed light for Ru film thickness above ~10 nm.

Table 5.1 summarizes the results described above, showing the calculated amounts of absorbed light for 20 nm and 50 nm thick Ru films on glass, sapphire and silicon for a wavelength of 1 000 nm. For each of the three substrates the absolute variation of the amount of absorbed light with film thickness is below 10% for thicknesses above approximately 10 nm.

As a next step, we tested our patterning method on Ru samples on glass with a thickness of

Table 5.1: Calculated percentages of absorbed light for 20-nm and 50-nm thick Ru films on different substrates

Substrate	Absorption (20 nm Ru)	Absorption (50 nm Ru)
Glass	34%	30%
Sapphire	32%	30%
Si (includes 5 nm native SiO_2)	24%	29%

20 nm and 50 nm, in order to characterize the dependence of the island-formation threshold fluence on film thickness. The samples were exposed to the beam focused to a 2 μm

diameter spot, 10 000 pulses and a (single-pulse) fluence varying from 0.8 mJ/cm^2 to 50 mJ/cm^2.

Figure 5.3(a) shows the optical microscopy image of an 8×8 grid of Ru/RuO_2 islands remaining after exposure (followed by rinsing in the NaClO solution) of a 20 nm thick Ru film. Each spot corresponds to a different exposure fluence, which increases from the top right to the bottom right corner in a meandering fashion. The first row of islands is missing (top region, hence only 7 rows are visible), and the second row only shows islands, corresponding to the white spots, starting from the second position from the left. The first row is absent because the exposure fluence did not result in the formation of a thick enough oxide to prevent dissolution of the Ru in the NaClO solution. The second line (the first visible one from the top) consists of seven bright spots, corresponding to the Ru/RuO_2 islands. As demonstrated previously (chapter 4)[111], the islands can have diameters from 500 nm to a maximum of 2 μm. The exposure fluence for these spots is between 7.8 mJ/cm^2 and 10.25 mJ/cm^2. The regions exposed to higher fluences have an irregular shape and a hole in the center, indicating damage in the form of ablation of the Ru. The same experiment was performed on a 50 nm thick Ru sample, for which we found that the fluence interval corresponding to island formation is from 16.4 mJ/cm^2 to 23.4 mJ/cm^2.

To extract a more precise threshold fluence for island formation, we performed a Liu analysis on the Ru/RuO_2 islands shown in figure 5.3(a) (20 nm thick Ru film), and on the islands obtained on the 50 nm thick Ru sample. The results are shown in figure 5.3(b). For this plot, and for all the others presented in this paper, we only extracted the areas of the "smooth-looking" Ru/RuO_2 islands and excluded the damaged ones. The solid lines are the linear fits to the data, from which the threshold fluences are extracted. The island-formation threshold fluence is 7.5 mJ/cm^2 for a 20 nm film, and 16.1 mJ/cm^2 for a 50 nm film. Island formation therefore occurs at a lower fluence for a 20 nm film, compared to a 50 nm one.

Similar results were obtained for the same film thicknesses when exposing the samples to 50 000 pulses, instead of 10 000. In that case, the extracted threshold fluences are 4.8 mJ/cm^2 (for the 20 nm thick film) and 10.8 mJ/cm^2 (for the 50 nm thick film). This agrees with what we have shown earlier: exposure to a higher number of pulses results in only a moderate decrease in the threshold fluence[111]. We note that the ratio between the threshold fluences for the 20 nm film and for the 50 nm one (0.43 for 10 000 pulses exposure; 0.44 for 50 000 pulses exposure) is similar to the ratio of the film thicknesses (0.4). As we show in figure 5.2, the two films absorb similar amounts of light. After absorption, thermalisation of the electrons with the lattice occurs on a picosecond time-scale[102]. After that, the

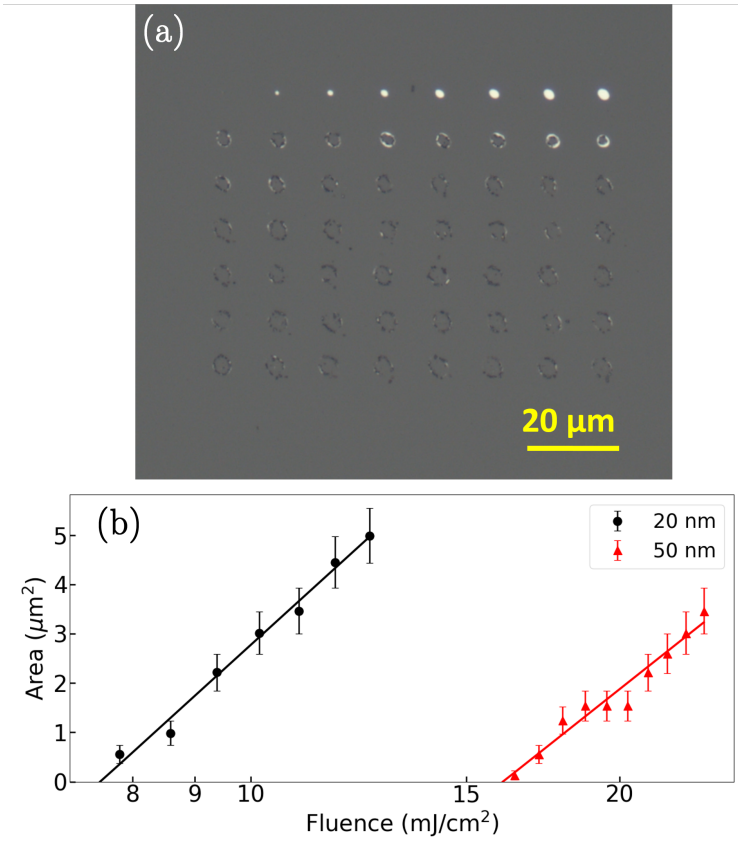

Figure 5.3: **(a)** Optical microscopy image of an 8×8 grid of exposure sites obtained from a 20 nm thick Ru film on glass. Each site was exposed to a different fluence, increasing from the top-right to the bottom-right corner of the image. **(b)** Liu plots obtained from optical microscopy images similar to figure (a) from a 20 nm (black) and a 50 nm (red) thick ruthenium film. Note the logarithmic scale of the horizontal axis.

thermal energy density in the film formed at the island formation threshold fluence scales by the same factor as the thickness: an n-fold thickness increase in thickness corresponds to an n-fold increase in threshold fluence. This should allow to extrapolate the fluences necessary to obtain Ru/RuO_2 patterns from Ru films with a chosen thickness, at least as long as it can be assumed that the film is homogeneously heated throughout its thickness. The latter is confirmed by two-temperature model calculations (see also below) for a 50 nm thick layer, which show that after approximately 2.5 ps, the lattice temperature at the surface is only about 20 K higher than at the back of the layer. This might, however, not be true for much thicker films.

In the following, the effect of different substrates on the production of Ru/RuO_2 patterns is studied. We deposited 50-nm-thick Ru films on two additional different substrates: sap-

phire and silicon. The laser was again focused to a 2 μm spot and the films were exposed to 25 000 pulses. The exposure fluence was varied between 0.6 mJ/cm^2 and 40 mJ/cm^2, in an experiment similar to the one resulting in figure 5.3. For sapphire (silicon), Ru/RuO_2 islands are formed for fluences between 15 mJ/cm^2 (15.6 mJ/cm^2) and 29 mJ/cm^2 (30 mJ/cm^2). At higher fluences, damage was observed.

The Liu plots obtained from the optical microscopy images of the samples are shown in figure 5.4. For Ru deposited both on silicon (black dots) and sapphire (red triangles) we observe a linear dependence of the island area on the logarithm of the exposure fluence. This allowed us to perform a linear fit (solid lines) and extract the threshold fluences for island formation, similar to what we did for Ru on glass shown in figure 5.3(b). The threshold fluence is 14.4 mJ/cm^2 for Ru on sapphire and 15.3 mJ/cm^2 for Ru on silicon.

The thermal conductivity of sapphire is 23 W K^{-1} m^{-1} [75], while that of silicon is 142

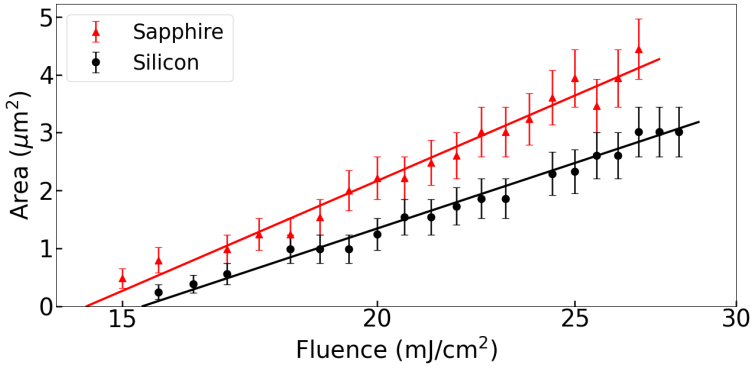

Figure 5.4: Liu plots obtained from the areas of Ru/RuO_2 islands produced from 50 nm thick Ru deposited on silicon (black circles) and sapphire (red triangles) exposing the samples to 25 000 pulses

W K^{-1} m^{-1}. Given such a large difference in the thermal conductivities of the substrates, it is a bit surprising that the threshold fluences for island formation are not very different between sapphire and silicon. Note that these numbers are still comparable with those found for Ru on glass for 10 000 shots (16.1 mJ/cm^2) and for 50 000 shots (10.8 mJ/cm^2), even though glass has a much lower thermal conductivity of about 1.14 W K^{-1} m^{-1}. A higher thermal conductivity should result in a more efficient diffusion of heat from the metal into the substrate, therefore lowering the Ru temperature in a shorter time. This would require higher fluences to maintain a high enough temperature for a long enough time to form the oxide layer which prevents dissolution in the NaClO solution. However, the threshold fluences for Ru on sapphire and on silicon, for example, are very similar (14.4 mJ/cm^2 for Ru on sapphire; 15.3 for Ru on silicon) while their thermal conductivities are

very different. The small difference with glass is even more striking, considering that its thermal conductivity is more than an order of magnitude lower than that of sapphire. The fairly similar fluence thresholds are probably due to the presence of a finite heat diffusion-limiting interfacial thermal conductivity (ITC)[102]. It is therefore possible that finite ITCs result in similar heat transfer dynamics even if the thermal conductivities of the substrates are largely different. For silicon, the presence of a native oxide may also have an effect on the heat diffusion into the substrate, having interfaces with both the Ru and the silicon, effectively lowering the ITC between the Ru and the silicon.

The patterning method allows us to fabricate Ru/RuO_2 islands with a diameter below the optical diffraction limit of the system used for the exposure. Indeed, we obtained islands with a diameter of about 500 nm by focusing the 1030 nm laser to a spot with a 2 μm diameter[111]. To study the effect of the laser spot size on the formation of these islands, we exposed the Ru to a beam focused to 0.8 μm diameter. This was done on a 50 nm thick Ru film on glass. Again, 8×8 grids of regions exposed to different fluences were produced.

Figure 5.5 is the optical microscopy image of one grid of Ru/RuO_2 islands on glass obtained by exposing the sample to 10 000 laser pulses with a 0.8 μm diameter beam. Similar to figure 5.3(a), the exposure fluence increases from the top-right corner to the bottom-right corner in a meandering way. The exposure fluence was varied between 2 mJ/cm^2 and 124 mJ/cm^2. The two topmost rows of exposed spots are empty, showing that a not thick enough RuO_2 layer formed on top of the Ru, while the islands in the two lowest rows show evident signs of laser-induced damage. This is also true for the five islands on the right of the third row from the bottom of the grid. From this, the fluence resulting in island formation ranges from 35 mJ/cm^2 to 75 mJ/cm^2. This result demonstrates that not only a 2 μm, but also a 0.8 μm dameter exposure spot is capable of producing Ru/RuO_2 islands. Note that because the substrate used for these experiments is glass, SEM imaging could not be used to determine the size of the smallest islands created due to charge accumulation on the sample.

We repeated the experiment resulting in figure 5.5 by using 1, 1 000, 20 000, 50 000 and 200 000 pulses. Exposure to a single pulse did not result in island formation. The diameters of the Ru/RuO_2 islands were extracted to obtain the Liu plots similar to those of figure 5.3(b), which are shown in figures 5.6(a) to (e).

We note that the islands have dimensions which are close to the resolution of the optical microscope, resulting in the relatively large error bars in the plots in figures 5.6(a)-(e). In addition, the smallest increase in island diameter that we could extract corresponds to about one image pixel. For this reason, plateaus appear in the data in the Liu plots. However,

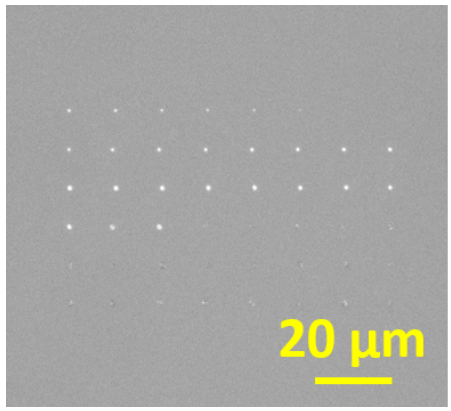

Figure 5.5: Optical microscopy image of a grid of Ru/RuO_2 islands obtained with a 0.8 μm exposure diameter. The 50 nm thick Ru film was exposed to 10 000 pulses with fluence increasing in a meandering fashion. The fluence increases from the top-right to the bottom-right corner of the grid.

it can be seen that the area of the islands scales approximately linearly with the logarithm of the exposure fluence within the error bars, and taking into account the aforementioned step-wise increase due to the microscope resolution. In addition, by comparing figures 5.6(a) to (d), the lowest fluence that results in the formation of a Ru/RuO_2 island decreases with exposure to a higher number of pulses. An exception is figure 5.6(e), corresponding to exposure to 200 000 pulses, in which the smallest island forms at an exposure fluence slightly higher than the one corresponding to 50 000 pulses. This difference is currently not understood.

To determine the threshold fluence F_0 for island formation, linear fits in the data in figures 5.6(a)-(e) were performed (solid lines), similar to what was done in figures 5.3 and 5.4. In figure 5.7 we plot F_0 as a function of the number of pulses extracted from the Liu plots of figures 5.6(a)-(e). The threshold fluence decreases steeply in a non-linear fashion from 51 mJ/cm^2 at 1 000 pulses, down to 25 mJ/cm^2 at 50 000 pulses. A moderate increase occurs for exposure to 200 000 pulses, at which F_0 has a value of 30 mJ/cm^2. This marked dependence on number of pulses is an indication that heat and/or oxidation accumulation plays a role in the island formation.

In the previous sections, the results obtained by exposing the samples to a beam focused to a 2 μm and to a 0.8 μm diameter were reported. For the 2 μm spot, we found a threshold of 10.8 mJ/cm^2 for Ru on glass exposed to 50 000 pulses, significantly lower than for the 0.8 μm laser spot size.

We now turn to the heat diffusion analysis. Heat deposited by the laser can diffuse in the direction orthogonal to the sample surface and into the substrate, and it can diffuse radi-

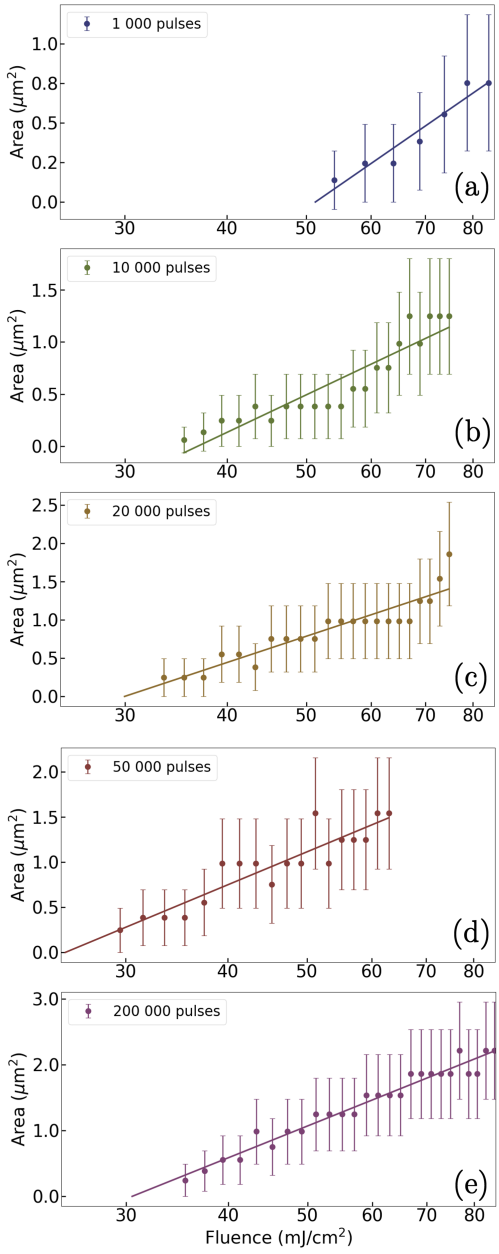

Figure 5.6: Liu plots obtained by extracting the Ru/RuO_2 island areas after exposure to the laser focused to a 0.8 μm diameter spot, for different numbers of pulses (indicated in the figures).

ally in the in-plane direction. To quantify the effect of heat diffusion, we performed heat diffusion calculations for a 50 nm thick Ru film on glass in order to model the temporal

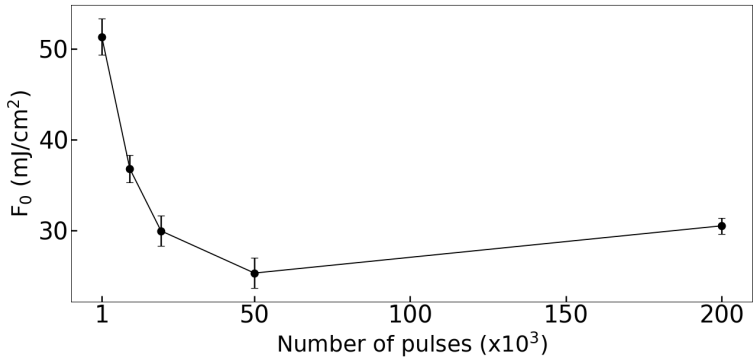

Figure 5.7: Island formation threshold fluence F_0 extracted from the Liu plots of figure 5.6, as a function of the exposure number of pulses.

and spatial evolution of the temperature at the surface of the Ru film which, in turn, results in oxidation. In the following, the procedure used for performing these calculations is described (a more detailed description is provided in chapter 2, section 2.4).

As a starting point, the percentage of absorbed light was calculated in the same way as for figure 5.2. In metals, the energy deposited by laser illumination is absorbed by the electron gas. The electron gas thermalizes on a timescale of a few hundreds femtoseconds [50]. Subsequently, within a few picoseconds, the electron gas transfers energy to the lattice via electron-phonon coupling. The energy exchange between the electron gas and the lattice is described by the *two-temperature model* (TTM) [47]. This model consists of two coupled differential equations describing the spatio-temporal evolution of the temperature of the electron gas and of the lattice, respectively. The TTM was used to obtain the spatial temperature profile of the lattice once it approximately reaches thermal equilibrium with the electron gas, which occurs after approximately 2 ps after the light absorption. The temperature distribution of the lattice at this moment is used as the starting condition for the single-temperature heat diffusion calculation described below. The latter calculations focus only on the lattice temperature.

In order to model heat transport, we assume rotational symmetry, assuming no azimuthal-angle dependence. The heat diffusion equation thus obtained is:

$$\frac{\partial u}{\partial t} = \frac{k}{\rho c}\left[\frac{\partial^2 u}{\partial r^2} + \frac{1}{r}\frac{\partial u}{\partial r}\right] + \frac{1}{\rho c}\frac{\partial k}{\partial z}\frac{\partial u}{\partial z} + \frac{k}{\rho c}\frac{\partial^2 u}{\partial z^2} \tag{5.1}$$

Where u is the temperature, r is the radial coordinate, z is the depth within the sample, k is the thermal conductivity, ρ the material density and c the specific heat capacity. In-plane

heat diffusion is described by the terms between the square brackets. The z-dependence of the thermal conductivity ($k = k(z)$) is included to model a system consisting of different layers. Its derivative is nonzero only at the interface between two materials which, in the case described here, is the interface between the Ru film and the substrate. Equation 5.1 was numerically solved using a forward-difference method. At the interface between the Ru and the substrate, *jump matching conditions*, as described in [52], were used. Our numerical calculations are limited to single pulse excitation only. Nevertheless, as we will show, this still gives significant insights into the heat diffusion dynamics occurring in our samples.

The temperature at the surface ($z = 0$) of a 50 nm Ru film on glass was calculated using the method described above, after exposure to a single laser pulse with a gaussian spatial cross section. In the calculations for Ru we used $\rho = 12.45 \times 10^3$ kg m^{-3}, c = 238 J kg^{-1} K^{-1} and $k = 120$ W K^{-1} m^{-1} [112]. For borosilicate glass we used k = 1.14 W K^{-1} m^{-1}, ρ = 2.23 $\times 10^3$ kg m^{-3}, and c = 820 J kg^{-1} K^{-1}. The value of the ITC between Ru and glass is unfortunately unknown. A value of 3.5 $\times 10^8$ W K^{-1} m^{-2} was measured in [51] for Ru on sapphire. Since we do not know this value for Ru on glass and, furthermore, because it can change based on the Ru deposition method, we varied its value between 10^8 and 10^{10} W m^{-2} K^{-1}. The calculations were performed for exposure diameters of 2 μm and of 0.8 μm. An exposure fluence of 1 nJ was used for the 2 μm diameter beam and 0.16 nJ for the 0.8 μm diameter one. Although heat transport can be affected by differences in the ITC, we found that the general conclusions that we can draw by comparing the results for the two exposure diameters, do not strongly depend on this value.

Figure 5.8 shows the temporal evolution of the temperature at the center of a spot exposed to a 2 μm beam diameter (red curve) and to a 0.8 μm beam (black curve). An ITC value of 10^9 W m^{-2} K^{-1} was used in this calculation. From the initial temperature of approximately 935 K, a steep temperature decrease occurs up to approximately 20 ps for both curves, although the decay of the black (dashed) curve begins to deviate from the red (solid) one already around 20 ps. This initial steep decay is associated, in both cases, with the equilibration of the lattice temperature within the Ru layer, as confirmed by comparing these heat transport calculations with TTM calculations in Ru for the first 20 ps. In this time interval, the curves overlap because there has not been enough time yet for radial heat diffusion and heat diffusion into the substrate.

The faster decay of the surface temperature observed at times $>$ 20 ps for the 0.8 μm diameter exposure with respect to that of the 2 μm exposure is due to the fact that, for a smaller focal diameter, the spatial temperature distribution has a steeper gradient in the ra-

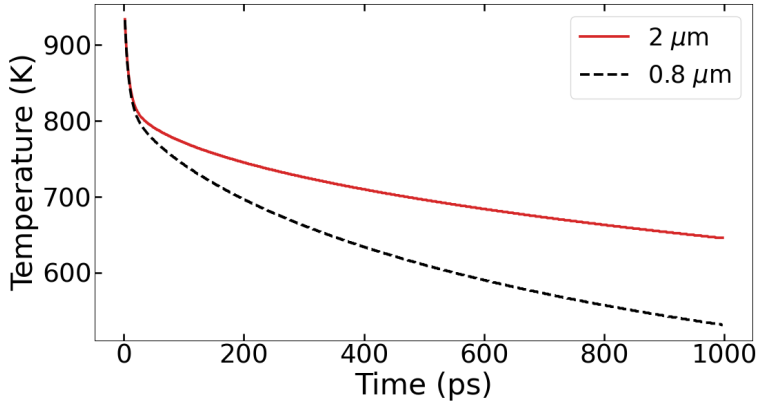

Figure 5.8: Calculated temporal evolution of the surface temperature at the center of the illuminated spot on a 50 nm thick Ru film for a 2 μm (red) and a 0.8 μm (black dashed) beam diameter.

dial direction. For Ru, for spot sizes smaller than about 1 μm diameter, loss of heat in the center of the spot due to radial heat diffusion overtakes loss of heat by diffusion into the substrate. This results in a more rapid in-plane heat transport and, therefore, more rapid temperature decrease.

5.4 Discussion

The partial oxidation of the Ru film, which prevents dissolution of the exposed regions in the NaClO solution, occurs as a consequence of a laser-induced temperature increase of the metal. A thick enough oxide is formed once a high enough temperature is reached and maintained for a long enough time. Testing the Ru/RuO_2 formation method on Ru films with different thicknesses and on films deposited on different substrates provides insight into the role of heat diffusion orthogonal to the sample surface. In particular, the results presented in figures 5.3 indicate that the threshold fluence necessary for the formation of a thick enough RuO_2 layer (F_0) depends directly on the initial Ru thickness. This result, combined with the fact that the calculated optical properties of Ru showed a moderate dependence on the film thickness between $\sim$ 8 nm and 100 nm (figure 5.2), strongly suggests that the threshold fluence for Ru/RuO_2 island formation in these samples solely depends on the energy density in the film after exposure. This conclusion holds as long as the Ru film is homogeneously heated over its thickness. For much thicker films this consideration probably does not hold. However, within the limit of homogeneously heated films, once

F_0 has been determined for the exposure conditions used, such as the number of pulses or the beam diameter, it is possible to estimate a priori the value of F_0 for a different film thickness.

The observation of similar island-formation threshold fluences obtained for Ru deposited on substrates with a relatively large difference in thermal conductivities (sapphire, silicon and glass) can be explained in terms of the interfacial thermal conductance between the metal and the substrate. For a homogeneously heated Ru film the lattice temperature decreases as a consequence of in-plane heat transport and diffusion into the substrate. Ideally, if the ITC between the metal and the substrate was infinite, heat diffusion from the Ru into the substrate would be purely determined by the thermal conductivity and the heat capacity of the substrate, as well as the total thermal energy contained in the Ru, and so would the threshold fluence F_0. However, finite values of ITC limit the heat diffusion from the metal into the substrate. It is therefore possible that differences in the thermal conductivities of the substrates are compensated by differences in the ITC, resulting in similar threshold fluences. This hypothesis should be confirmed by measurements of the ITC, which unfortunately are non-trivial to do and which were not performed at this stage.

The role of in-plane heat diffusion is understood as follows. Figure 5.7 shows a steep non-linear decrease of F_0 obtained after exposure to an increasing number of pulses using a 0.8 μm beam diameter. This result differs from our previous observation of a moderate linear decrease obtained when using a 2 μm exposure diameter[111] (chapter 4). The calculated temporal evolution of the Ru lattice-temperature at the surface of the film shows a faster temperature decay after exposure to the 0.8 μm beam starting from approximately 20 ps after exposure. This is due to the fact that the smaller exposure spot corresponds to a steeper radial temperature gradient. This increases the rate of in-plane heat diffusion and results in a faster temperature decay. For this reason, the decrease of the surface temperature at the center of the exposed region during the 5 μs occurring between the arrival of each laser pulse (since the repetition rate of the laser is 200 kHz) is significantly larger for exposure to the 0.8 μm beam than for the 2 μm one. The key difference here is that, after exposure to a 2 μm spot, a high enough temperature necessary for oxidation is maintained for a long enough time, allowing oxidation of a small fraction of the film. For the 0.8 μm beam and the same number of laser exposure pulses, on the other hand, the decay is too fast. Therefore, a higher initial temperature needs to be reached, and thus a higher fluence has to be used, so that the surface lattice temperature is maintained above the oxidation threshold temperature for a long enough time after exposure. The latter conclusion is also supported by the fact that, overall, the threshold fluences extracted for exposure to the 0.8

μm exposure diameter are higher than those extracted for the 2 μm exposure.

5.5 Conclusion

We have studied the formation of Ru/RuO_2 islands on various substrates, formed by partial oxidation of the Ru by multiple focused laser pulses, followed by removal of the unoxidized Ru in a NaClO solution. From measurements on 20- and 50-nm-thick Ru layers on glass, and from the calculated amount of absorbed light, we conclude that the fluence threshold for island formation can be estimated a priori for different layer thicknesses. Subsequently, the role of the substrate material was tested leading to the conclusion that the main parameter determining the island-formation threshold fluence for different substrate materials is the interfacial thermal conductance between the Ru and the substrate, rather than the thermal conductivity of the substrate alone.

When using a sub-micron exposure beam diameter we also show that in-plane heat diffusion likely affects the island-formation process. Although a small exposure diameter may make it possible to produce patterns with increasingly small dimensions, we show that the role of in-plane heat diffusion must be taken into account as it may limit the effective spatial resolution achievable by this patterning method.

LIST OF PUBLICATIONS

This thesis is based on the following publications:

Chapter 3: Lorenzo Cruciani[1,2,3,4,5,6], Stefan van Vliet[2,6], Alessandro Troglia[2,6], Roland Bliem[6,7], Klaasjan van Druten[1,6,7], and Paul Planken[1,6,7]; *Femtosecond Laser-Induced Emission of Coherent Terahertz Pulses from Ruthenium Thin Films*, *The Journal of Physical Chemistry C* **2023** 127 (46), 22662-22672 DOI: 10.1021/acs.jpcc.3c05525

Chapter 4: Lorenzo Cruciani[1,2,3,4,5,6], Marnix Vreugdenhil[2,6], Stefan van Vliet[2,6], Ester Abram[2,6], Dries van Oosten[6,7], Roland Bliem[6,7], Klaasjan van Druten[1,6,7], Paul Planken[1,2,6,7]; *Direct laser patterning of ruthenium below the optical diffraction limit*, *Appl. Phys. Lett.* **2024**, 124 (17): 171902. DOI: 10.1063/5.0205538

Chapter 5: Lorenzo Cruciani[1,2,3,4,5,6], Marnix Vreugdenhil[2,6], Dries van Oosten[6,7], Klaasjan van Druten[1,6,7] and Paul Planken[1,2,6,7]; *Effect of Substrate and Beam Diameter on Direct Laser Patterning of Ruthenium Thin Films* Submitted to *Optical Materials Express*

[1] Conceptualization
[2] Data acquisition (experiments)
[3] Data analysis
[4] Manuscript preparation
[5] Writing (original draft)
[6] Writing (review)
[7] Supervision

SUMMARY

Ruthenium thin films: terahertz generation and direct laser patterning

The study of materials and the development of suitable techniques to exploit them have always been a driving force for the technological advancement of humanity. In the current era, information technology plays a central role in the global economy and society. Therefore, a significant effort is directed towards the improvement of materials and techniques involved in the production of electronic devices, such as integrated circuits. In this field, one of the main challenges is the need to manufacture components with increasingly small features, allowing to increase the computational power of the final products. Decreasing the production costs by establishing novel processing techniques or optimizing existing ones, as well as introducing novel materials, can promote the development of this field. Optical lithography is one of the main techniques used to produce printed circuits. It consists of changing the solubility of a resist deposited on top of the end material by shining a light source onto it. This way, it is possible to selectively remove certain portions of the end material or add other materials and obtain a conductive pattern.

Ruthenium is a candidate for applications in the field described above thanks to its relatively high electrical conductivity, chemical stability and high melting temperature. The latter property allows it to withstand high power illumination before incurring into light-induced damage. In addition, the oxide RuO_2 is also metallic, compared to other metal-oxides, such as copper-oxides. For these reasons, this thesis focuses on the study of ruthenium.

In detail, Chapter 3 focuses on the emission of coherent terahertz (THz) electromagnetic radiation from Ru thin films. It is demonstrated that Ru emits THz radiation as a result of illumination with a near-infrared femtosecond laser pulse through a second-order nonlinear optical process. It is also shown that laser-induced oxidation can occur and that the amount of oxidation, resulting either from laser exposure or from thermal annealing, correlates with the emission-strength of the THz radiation. This result also shows that THz radiation can be used as a probe for the degree of oxidation of Ru samples.

The angle of the THz polarization was determined and a surprising dependence on the substrate materials and on oxidation was observed. While the THz electric field is polarized orthogonally to the sample surface for un-oxidized Ru films on sapphire and calcium fluoride (CaF_2), an additional polarization component, parallel to the sample surface is present for un-oxidized Ru deposited on boro-silicate glass. Furthermore, for (partially) oxidized Ru films, this THz polarization component parallel to the sample surface is present also for films deposited on sapphire or CaF_2, in addition to Ru on glass. Even more surprisingly, any time a THz polarization component parallel to the sample surface is present, it is shown that the THz electric field points towards a fixed direction along the sample surface. This observation highlights the presence of some source of asymmetry, resulting in a preferential orientation of the THz electric field. The source of this asymmetry was searched through two-dimensional x-ray-diffraction and atomic force microscopy but it is currently unknown. Since the only evidence of this asymmetry is the polarization of the THz radiation, this shows that THz emission can be used as a tool for the study of material properties with a potentially higher sensitivity compared to other techniques.

In Chapter 4, the laser-induced oxidation process demonstrated in Chapter 3, is applied to produce patterns. Immersion in a NaClO solution in water dissolves and removes the Ru from the substrates, leaving only the partially oxidized areas. Laser-induced oxidation and removal of the un-oxidized Ru through the NaClO solution is presented as a method for producing conductive patterns consisting of Ru with a thin layer of RuO_2 on top. A proof of concept is provided by producing near-circular Ru/RuO_2 islands with an as-small-as-possible diameter. Remarkably, islands with a diameter as small as 500 nm were obtained using a 1030 nm wavelength exposure laser, focused to a spot with a 2 μm diameter. These islands, therefore, have a diameter below the optical diffraction limit of the optical system used for exposure.

The island formation process is compared between the case of laser exposure performed using a high-repetition-rate laser focused to a spot with a diameter of 8 μm and that of exposure to a low-repetition-rate laser focused to a spot with a diameter of 2 μm. Evidence of heat accumulation and in-plane heat diffusion was observed in the first case. This is because the short time interval occurring between the arrival of each laser pulse does not allow the lattice to return to its initial temperature. The low-repetition-rate laser, on the other hand, showed evidence of accumulation of oxidation, rather than accumulation of heat.

In chapter 5 the patterning method introduced in chapter 4 is further investigated with the goal of providing insight on its potential and its limitations, as well as additional under-

standing of the island-formation process. The role of Ru film thickness is probed showing that within the limits in which the Ru film can be considered to be homogeneously heated by the exposure-laser pulses, the threshold fluence for island formation can be determined a priori. In addition, the method is tested on Ru deposited on different substrates: glass, sapphire and silicon. It is shown that the island formation threshold fluence depends weakly on the substrate. This is because, after laser exposure, heat diffusion into the substrate is limited by the finite interfacial thermal conductance (ITC) between the ruthenium and the material underneath.

The role of the exposure-beam diameter is tested by measuring the island formation threshold fluence as a function of the number of laser pulses using a 0.8 μm exposure beam diameter. These results are compared to the ones presented in chapter 4, obtained by using a 2 μm beam diameter. By combining this with heat diffusion calculations it is shown that in-plane heat diffusion has a stronger effect when using a sub-micron exposure beam diameter, compared to the 2 μm one. While, in principle, one could expect that a smaller beam diameter allows to obtain Ru/RuO_2 patterns with smaller dimensions, in-plane heat diffusion could limit the sharpness of the obtained patterns.

In conclusion, the study of THz emission from Ru provided additional understanding of its optical and material properties. THz emission can be applied to the study of materials given its high sensitivity which allows to detect features which can go unnoticed through other techniques. Further, a method for producing Ru based conductive patterns was introduced, representing a cheaper and simpler alternative to conventional optical lithography.

SAMENVATTING
Ruthenium dunne lagen: terahertz generatie en directe laser patroonvorming

Het onderzoeken van materialen en de zoektocht naar geschikte technische toepassingen zijn altijd al een drijvende kracht achter de technologische vooruitgang van de mensheid geweest. In deze moderne tijd speelt informatietechnologie een centrale rol in de wereldeconomie en samenleving. Daarom wordt er veel moeite gestoken in het verbeteren van de materialen en technieken die betrokken zijn bij de productie van elektronische apparaten, zoals geïntegreerde schakelingen. Een van de grootste uitdagingen in dit onderzoeksgebied is het vervaardigen van steeds kleinere structuren op deze componenten, waardoor de rekenkracht van het eindproduct kan worden vergroot. Het ontwikkelen van nieuwe procestechnieken, het optimaliseren van bestaande methoden, evenals de introductie van nieuwe materialen kunnen de productiekosten verlagen en daarmee de vooruitgang van dit onderzoeksgebied stimuleren.

Optische lithografie is een van de belangrijkste technieken die wordt gebruikt voor het vervaardigen/printen van computerchips. Dit proces omvat het lokaal veranderen van de oplosbaarheid van een fotolak die is aangebracht op een dunne laag, door blootstelling aan een lichtbron. Hierdoor kunnen bepaalde delen van die laag selectief worden verwijderd, of juist toegevoegd worden, wat resulteert in een elektrisch geleidend patroon.

Ruthenium is een veelbelovende materiaal in de technologie zoals hierboven beschreven. Dit komt dankzij zijn relatief hoge elektrische geleidbaarheid, chemische stabiliteit en hoog smeltpunt. Vanwege dit hoge smeltpunt kan het ook een hoge lichtintensiteit weerstaan zonder dat er licht-geïnduceerde schade optreedt. Bovendien heeft het oxide RuO_2 dat zich vormt ook een relatief hoge geleidbaarheid in vergelijking met andere metaaloxiden, zoals koperoxiden.

Hoofdstuk 3 zich op de emissie van coherente terahertz (THz) elektromagnetische straling van dunne lagen ruthenium (Ru). Hier wordt aangetoond dat de THz-straling die het ruthenium uitzendt, het gevolg is van de bestraling met een nabij-infrarode femtoseconde laserpuls en via een niet-lineair optisch proces van de tweede orde verloopt. Ook

wordt aangetoond dat laser-geïnduceerde oxidatie kan optreden en dat de mate van oxidatie, zowel door blootstelling van de laser als door verwarming in een oven correleert met de sterkte van de THz-emissie. Dit resultaat toont bovendien aan dat THz-straling kan worden gebruikt om de oxidatiegraad van Ru lagen te bepalen.

Door de polarisatiehoek van de THz-straling te meten, is er een verrassende afhankelijkheid van de substraatmaterialen en oxidatie vastgesteld. Terwijl voor niet-geoxideerde Ru-films op saffier en calciumfluoride (CaF_2), de polarisatie van het THz-elektrische veld loodrecht op het Ru oppervlak is gericht, is er bij niet-geoxideerd Ru op borosilicaatglas een extra polarisatiecomponent parallel aan het oppervlak aanwezig. Verder is deze parallelle polarisatiecomponent ook aanwezig bij (gedeeltelijk) geoxideerde Ru lagen wanneer deze op saffier of CaF_2 substraten zijn gefabriceerd. Nog verrassender is dat, telkens wanneer een parallelle THz-polarisatiecomponent aanwezig is, het THz-elektrische veld een vaste richting langs het oppervlak aanneemt. Dit wijst op een asymmetrische effect dat een voorkeursrichting van het THz-veld veroorzaakt. Hoewel er met behulp van tweedimensionale röntgendiffractie en atoomkrachtmicroscopie gezocht is naar de onderliggende oorzaak van deze asymmetrie, is deze tot op heden nog steeds onbekend. Aangezien de polarisatie van de THz-straling de enige aanwijzing voor deze asymmetrie is, betekent dit dat de THz-emissie kan worden gebruikt als een gevoelige techniek voor het bestuderen van materiaaleigenschappen.

In Hoofdstuk 4 wordt het laser-geïnduceerde oxidatieproces van Hoofdstuk 3 toegepast om patronen te produceren. Door het onderdompelen van het ruthenium in een NaClO-oplossing, wordt het niet-geoxideerde Ru opgelost en verwijderd, waarbij alleen de gebieden die gedeeltelijk zijn geoxideerde achter blijven. Laser-geïnduceerde oxidatie en het vervolgens verwijderen van het niet-geoxideerde Ru met de NaClO-oplossing, wordt gepresenteerd als een methode om geleidende patronen te vervaardigen die bestaan uit Ru met een dunne laag RuO_2 aan de bovenzijde. Als proof-of-concept worden quasi-cirkelvormige Ru/RuO_2-eilanden geproduceerd met een zo klein mogelijke diameter. Het opmerkelijke hieraan is dat eilanden met een diameter van slechts 500 nm gemaakt konden worden met behulp van een laser met een golflengte van 1030 nm, gefocuseerd tot een spot van 2 μm diameter. Deze eilanden hebben dus een diameter kleiner dan de diffractielimiet van het optische systeem dat is gebruikt voor de belichting van het Ru.

Er wordt vergeleken wat het verschil is in het eilandvormingsproces tussen blootstelling aan een laser met een hoge herhalingsfrequentie, gefocuseerd tot een spot met een diameter van 8 μm, en blootstelling aan een laser met een lage herhalingsfrequentie, gefocuseerd tot een spot van 2 μm. In het eerste geval worden warmteaccumulatie en warmtetransport in het

vlak waargenomen, omdat het tijdsinterval tussen de laserpulsen te kort is voor het rooster om naar de initiële temperatuur terug te keren. De laser met de lage herhalingssnelheid zorgde, in plaats voor warmteaccumulatie, juist voor een accumulatie van het oxide.
In Hoofdstuk 5 wordt de patroonvormingsmethode uit Hoofdstuk 4 verder onderzocht, met als doel het bieden van inzicht in de mogelijkheden en beperkingen van deze methode, alsmede het verkrijgen van een beter begrip over het eilandvormingsproces. Daarom wordt hier de invloed van de dikte van de Ru-film onderzocht. Hierbij wordt aangetoond dat, wanneer de Ru-film nog dun genoeg is zodat nog aangenomen kan worden dat de Ru-laag homogeen wordt opgewarmd door de laserpulsen, de drempelfluentie voor eilandvorming vooraf kan worden bepaald. Daarnaast wordt de methode getest op Ru lagen die zijn gefabriceerd op verschillende substraten: glas, saffier en silicium. Het blijkt dat de drempelfluentie voor eilandvorming slechts licht wordt beïnvloed door het substraat, omdat de warmteverspreiding, na de blootstelling aan de laser, wordt beperkt door de eindige thermische weerstand tussen het ruthenium en substraat.
De rol van de diameter van de laserspot wordt getest door de drempelfluentie voor eilandvorming te meten als functie van het aantal laserspot met een diameter van 0.8 μm. Deze resultaten worden vervolgens vergeleken met die uit Hoofdstuk 4, waar de laserspot diameter van 2 μm heeft. Door dit te combineren met warmtevergelijkingsberekeningen, wordt er aangetoond dat de diffusie van de warmte in het Ru vlak sterker is bij gebruik van een submicron diameter laserspot in vergelijking met een 2 μm diameter laserspot. Hoewel men in theorie zou verwachten dat een kleinere diameter het mogelijk maakt om Ru/RuO_2 patronen met kleinere afmetingen te fabriceren, kan in werkelijkheid de warmtediffusie in evenwijdig aan het vlak van de film de resolutie van de patronen beperken.
Deze studie van THz-emissie aan Ru heeft bijgedragen tot een beter begrip van de optische en materiaaleigenschappen. Er is aangetoond dat THz-emissie kan worden toegepast op materiaalstudies dankzij de hoge gevoeligheid waarmee eigenschappen kunnen worden gedetecteerd die met andere technieken onopgemerkt blijven. Bovendien is er een methode geïntroduceerd voor het vervaardigen van geleidende patronen in Ru, die een goedkoper en eenvoudiger alternatief biedt voor de conventionele optische lithografie methodes.

ACKNOWLEDGMENTS

It is not very original to say that a Ph.D. is hard. However, in some periods I felt that it was too much for me. Without the support of certain people, I am sure that I would not have been able to make it until the end. Here, I would like to say "thank you" to those people and tell them that they inhabit a special place inside my heart.

First of all prof. Paul Planken. Thank you for believing in me and accepting me in your group. Many times I entered your office a bit demotivated or worried. However, after a short (actually, quite often long, but always interesting!) chat with you I always left your office with a restored motivation and many good vibes that filled me with energy. I think that this is a gift that you have and that makes you such a great supervisor and a splendid person.

Prof. Klaasjan van Druten. You are one of the kindest and most sympathetic people I know. I am also grateful to you for believing in me at the beginning and continuing to do so later on. I always felt a huge support from you and a genuine effort to always understand my difficulties and help me.

I feel extremely lucky to have been part of the *light-matter interaction group*. My former colleague Guido de Haan helped me so much at the beginning. Guido, I entered your lab many times asking for help and you were always happy to assist me. You taught me a lot and thanks to you I was able to put my hands on the optics with a bit of confidence and knowledge. I admired you so much for your knowledge and skills, and I still do.

Thomas Meijvogel, thank you for your patience and for never saying "no" to my requests. You were always ready to help with anything I needed in the lab and, also, you were always careful in doing things in the best possible way: even when I thought that it was good enough you just had to make things perfect. This is an example that I will try to follow. Also, you are a man of culture and of fine taste when it comes to music, movies and books, I will never forget your version of "Fire" by Arthur Brown, and I do not think I am alone in this.

Thomas van den Hooven, you also helped me a lot and I think you are a great person. In particular, I really enjoyed a chat we had once about life, our insecurities, our hopes etc. You had a couple beers so maybe you do not even remember that chat (LOL!) but it is a touching memory that I will carry with me.

Ester Abram, when I first met you I was already in the Netherlands for more than two years, but I think I really got into Dutch culture through you. You made me feel at home, you introduced me to your sister Leah and your friend Binkie, which, together with you, I consider my dutch family. The Borrels at your place were always special, just like you. You are full of energy, passions and interests and in all this you also are always there for your friends. I am grateful to have been so lucky to meet you.
Christoph Morscher, I enjoyed so much spending time with you in the lab when you enthusiastically showed me the results of your projects. Also, I loved randomly meeting you in the corridors and just giving each other a hug. These moments filled me with joy and made me feel supported and loved.
Barsha Bhattacharjee, you have a huge, shining soul that one can spot just by looking into your eyes or listening to you sing. I remember the first night that we went out alone, eating veggies and chips in front of the UvA building; we bonded instantly. I am thankful for having you in my life.
Augustas Karpavičious, you are an old-fashioned hopeless romantic with a deep soul, uncommon intelligence, kind and funny (your "that's what she said" jokes never failed to make me laugh). I will never forget our day at the beach in Italy. Thank you for being who you are.
Matthias Gouder, you are just from another universe. I never met someone so joyful, caring, kind, intelligent, enthusiastic, determined etc. I do not know enough adjectives to describe you. I only know that I never met anyone like you. You are special and I hope that the world gives you back even just a small portion of the beauty that you bring in it. Thank you for being my friend.
Nataliia Kuzkova, you have the mind of a scientist and the soul of an artist. You appreciate beauty and kindness and you also radiate them to your surroundings. Thank you for giving them to me as well.
Matthijs Velsink, your intelligence and skills are combined with a huge kindness and sense of humor. I regret not spending more time with you but I am thankful for having met you.
Ester Pérez Penco, you have such a strong empathy and you are one of the most sweet and funny people I know. You made Amsterdam more sunny by just being there.
I also thank Stefan van Vliet, Alessandro Troglia and Marnix Vreugdenhill for their help in our research.

Federico Caporaletti, sei uno dei piú bei regali che mi ha fatto Amsterdam. É stato cosí bello passare il tempo con te che, grazie a te, ricordo la pandemia come un bel periodo.

Le cene, le serate passate a guardare video trash, il capodanno nel tuo appartamento con Daniela e quella indimenticabile focaccia con le cime di rapa (e ovviamente i ciauscoli!). Grazie a te e a Daniela per essere persone cosí uniche.
Andrea Orsini, sei accanto a me da quasi 15 anni. Non potrei immaginare la mia vita senza di te, sei un fratello maggiore a cui sono grato per tutto l'affetto ed il supporto, oltre che per le risate. Concetta Nardella, grazie anche a te per continuare ad essere nella mia vita.
Nicoló Capozza, abbiamo stretto amicizia in tempi recenti ma mi sembra di essere tuo amico da sempre. Hai una profonditá ed una sensibilitá fuori dal comune. Grazie per essermi amico.
Lucrezia Lo Dico, sei stata il regalo di bentornato che ho trovato a Roma. Tu, Andrea e Viola siete un concentrato di amore e dolcezza che mi ha aiutato a ricominciare a sentire Roma come casa mia.
Piergiorgio Solvi, grazie per avermi aiutato ad affrontare l'ultimo periodo del mio dottorato e a rimettermi sul sentiero verso la feliciá. Grazie per la tua disponibilitá, la tua empatia, la tua gentilezza, i tuoi interessantissimi spiegoni sulla psicologia. Se sono riuscito ad arrivare alla fine di questo percorso é anche grazie a te.
Papá e Mamma, andando in giro per il mondo non ho mai camminato solo sulle mie gambe. C'eravate e ci siete sempre voi ad alleviare il peso dello zaino che io, come tutti, porto sulle spalle. A volte, nonostante ció, questo peso mi é risultato troppo grande, ma voi non avete mai vacillato. Se sarete fieri di me non dimenticate che ho solo ricevuto il testimone dei vostri valori; dei valori dei nonni, che serbo nel mio cuore.
Alfredo, grazie per dimostrarmi l'amore ed il supporto che si mostra ad un figlio. Grazie per amare mia madre e per essere la persona paziente e gentile che sei.
Elena, grazie per avermi sempre fatto sentire affetto e dolcezza; anche tu sei un grande riferimento per me. Grazie per amare mio padre.
Marco, grazie per esserci sempre nel momento del bisogno. Francesco, grazie per la gioia che porti nella nostra famiglia. So che ci renderai fieri di te.

Giada, sebbene le nostre strade si siano divise non posso non ringraziarti per gli anni meravigliosi che mi hai regalato. Sono stati anni complicati e mi dispiace non averti potuto dare una versione di me piú spensierata ed avventurosa. Ti ringrazio per avermi dato la forza nei momenti piú difficili. Ti ringrazio per la goia e per l'amore, per le risate con il fischio, per ogni singolo ricordo. Ti ringrazio perché ci sei tu in tutto quello che di bello c'é stato in questi anni.

Bibliography

[1] Peter Rowley-Conwy. *From Genesis to Prehistory: The Archaeological Three Age System and its Contested Reception in Denmark, Britain, and Ireland*. Oxford University Press, 11 2007. ISBN 9780199227747. doi: 10.1093/oso/9780199227747.001.0001. URL https://doi.org/10.1093/oso/9780199227747.001.0001.

[2] Peter Turchin, Harvey Whitehouse, Sergey Gavrilets, Daniel Hoyer, Pieter François, James S. Bennett, Kevin Carter Feeney, Peter Neal Peregrine, Gary M. Feinman, Andrey Korotayev, Nikolay Kradin, Jill Levine, Jenny Reddish, Enrico Cioni, Romain Wacziarg, Gavin Mendel-Gleason, and Majid Benam. Disentangling the evolutionary drivers of social complexity: A comprehensive test of hypotheses. *Science Advances*, 8, 2022. URL https://api.semanticscholar.org/CorpusID:250022526.

[3] Manuel Castells. *The Rise of the Network Society*. John Wiley and Sons, Ltd, 2009. ISBN 9781444319514. doi: https://doi.org/10.1002/9781444319514.fmatter. URL https://onlinelibrary.wiley.com/doi/abs/10.1002/9781444319514.fmatter.

[4] Gordon E Moore. Cramming more components onto integrated circuits. *Electronics*, 38(8), 1965.

[5] Hiromitsu Takase, Shigeru Terashima, Yoshio Gomei, Masayuki Tanabe, Yutaka Watanabe, Takashi Aoki, Katsuhiko Murakami, Shuichi Matsunari, Masahito Niibe, and Yukinobu Kakutani. Study of ruthenium-capped multilayer mirror for EUV irradiation durability. In Michael J. Lercel, editor, *Emerging Lithographic Technologies X*, volume 6151, page 615135. International Society for Optics and Photonics, SPIE, 2006. doi: 10.1117/12.657089. URL https://doi.org/10.1117/12.657089.

[6] Grant R. Fowles. *Introduction to modern optics*. 1968. URL https://api.semanticscholar.org/CorpusID:120407687.

[7] Harry J. Levinson. The potential of EUV lithography. In Uwe F.W. Behringer and Jo Finders, editors, *35th European Mask and Lithography Conference (EMLC 2019)*, volume 11177, page 1117702. International Society for Optics and Photonics, SPIE, 2019. doi: 10.1117/12.2528446. URL https://doi.org/10.1117/12.2528446.

[8] Takashi Ito and Shinji Okazaki. Pushing the limits of lithography. *Nature*, 406: 1027–31, 09 2000. doi: 10.1038/35023233.

[9] Elizabeth Buitrago, Marieke Meeuwissen, Oktay Yildirim, Rolf Custers, Rik Hoefnagels, Gijsbert Rispens, Michaela Vockenhuber, Iacopo Mochi, Roberto Fallica, Zuhal Tasdemir, and Yasin Ekinci. State-of-the-art EUV materials and processes for the 7nm node and beyond. In Eric M. Panning, editor, *Extreme Ultraviolet (EUV) Lithography VIII*, volume 10143, page 101430T. International Society for Optics and Photonics, SPIE, 2017. doi: 10.1117/12.2260153. URL https://doi.org/10.1117/12.2260153.

[10] Sasa Bajt, Zu Rong Dai, Erik J. Nelson, Mark A. Wall, Jennifer B. Alameda, Nhan Q. Nguyen, Sherry L. Baker, Jeffrey C. Robinson, John S. Taylor, Andrew L. Aquila, and Nora V. Edwards. Oxidation resistance and microstructure of ruthenium-capped extreme ultraviolet lithography multilayers. *Journal of Micro/Nanolithography, MEMS, and MOEMS*, 5(2):023004, 2006. doi: 10.1117/1.2201027. URL https://doi.org/10.1117/1.2201027.

[11] Fedor Akhmetov, Igor Milov, Sergey Semin, Fabio Formisano, Nikita Medvedev, Jacobus M. Sturm, Vasily V. Zhakhovsky, Igor A. Makhotkin, Alexey Kimel, and Marcelo Ackermann. Laser-induced electron dynamics and surface modification in ruthenium thin films. *Vacuum*, 212:112045, 2023. ISSN 0042-207X. doi: https://doi.org/10.1016/j.vacuum.2023.112045.

[12] R.W. Powell, R.P. Tye, and Margaret J. Woodman. The thermal conductivity and electrical resistivity of polycrystalline metals of the platinum group and of single crystals of ruthenium. *Journal of the Less Common Metals*, 12(1):1–10, 1967. ISSN 0022-5088. doi: https://doi.org/10.1016/0022-5088(67)90062-8. URL https://www.sciencedirect.com/science/article/pii/0022508867900628.

[13] J.H. Huang and J.S. Chen. Material characteristics and electrical property of reactively sputtered ruo2 thin films. *Thin Solid Films*, 382(1):139–145, 2001. ISSN 0040-6090. doi: https://doi.org/10.1016/S0040-6090(00)01777-6. URL https://www.sciencedirect.com/science/article/pii/S0040609000017776.

[14] Dipanwita Majumdar, Thandavarayan Maiyalagan, and Zhongqing Jiang. Recent progress in ruthenium oxide-based composites for supercapacitor applications. *ChemElectroChem*, 6(17):4343–4372, 2019. doi: https://doi.org/10.1002/celc.201900668.

[15] J.H. Huang and J.S. Chen. Material characteristics and electrical property of reactively sputtered ruo2 thin films. *Thin Solid Films*, 382(1):139–145, 2001. ISSN 0040-6090. doi: https://doi.org/10.1016/S0040-6090(00)01777-6.

[16] Patrick Quarterman, Congli Sun, Javier García-Barriocanal, Mahendra Dc, Yang Lv, Sasikanth Manipatruni, Dmitri E. Nikonov, Ian A. Young, Paul M. Voyles, and Jianping Wang. Demonstration of ru as the 4th ferromagnetic element at room tempera-

ture. *Nature Communications*, 9, 2018. URL https://api.semanticscholar.org/CorpusID:44071705.

[17] Igor Milov, Igor A. Makhotkin, Ryszard Sobierajski, Nikita Medvedev, Vladimir Lipp, Jaromir Chalupský, Jacobus M. Sturm, Kai Tiedtke, Gosse de Vries, Michael Störmer, Frank Siewert, Robbert van de Kruijs, Eric Louis, Iwanna Jacyna, Marek Jurek, Libor Juha, Věra Hájková, Vojtěch Vozda, Tomáš Burian, Karel Saksl, Bart Faatz, Barbara Keitel, Elke Plönjes, Siegfried Schreiber, Sven Toleikis, Rolf Loch, Martin Hermann, Sebastian Strobel, Han-Kwang Nienhuys, Grzegorz Gwalt, Tobias Mey, Hartmut Enkisch, and Fred Bijkerk. Mechanism of single-shot damage of ru thin films irradiated by femtosecond extreme uv free-electron laser. *Opt. Express*, 26(15):19665–19685, Jul 2018. doi: 10.1364/OE.26.019665. URL https://opg.optica.org/oe/abstract.cfm?URI=oe-26-15-19665.

[18] Igor A. Makhotkin, Ryszard Sobierajski, Jaromir Chalupský, Kai Tiedtke, Gosse de Vries, Michael Störmer, Frank Scholze, Frank Siewert, Robbert W. E. van de Kruijs, Igor Milov, Eric Louis, Iwanna Jacyna, Marek Jurek, Dorota Klinger, Laurent Nittler, Yevgen Syryanyy, Libor Juha, Věra Hájková, Vojtěch Vozda, Tomáš Burian, Karel Saksl, Bart Faatz, Barbara Keitel, Elke Plönjes, Siegfried Schreiber, Sven Toleikis, Rolf Loch, Martin Hermann, Sebastian Strobel, Han-Kwang Nienhuys, Grzegorz Gwalt, Tobias Mey, and Hartmut Enkisch. Experimental study of EUV mirror radiation damage resistance under long-term free-electron laser exposures below the single-shot damage threshold. *Journal of Synchrotron Radiation*, 25(1):77–84, Jan 2018. doi: 10.1107/S1600577517017362. URL https://doi.org/10.1107/S1600577517017362.

[19] Cristiane R. Stilhano Vilas Boas, Jacobus M. Sturm, Wesley T.E. van den Beld, and Fred Bijkerk. Oxidation kinetics of transition metals exposed to molecular and atomic oxygen. *Materialia*, 20:101203, 2021. ISSN 2589-1529. doi: https://doi.org/10.1016/j.mtla.2021.101203. URL https://www.sciencedirect.com/science/article/pii/S2589152921002064.

[20] H A Hafez, X Chai, A Ibrahim, S Mondal, D Férachou, X Ropagnol, and T Ozaki. Intense terahertz radiation and their applications. *Journal of Optics*, 18(9):093004, aug 2016. doi: 10.1088/2040-8978/18/9/093004. URL https://dx.doi.org/10.1088/2040-8978/18/9/093004.

[21] Charlotte Bull, Simmone M. Hewett, Ruidong Ji, Cheng-Han Lin, Thomas Thomson, Darren M. Graham, and Paul W. Nutter. Spintronic terahertz emitters: Status and prospects from a materials perspective. *APL Materials*, 9(9):090701, 09 2021. ISSN 2166-532X. doi: 10.1063/5.0057511. URL https://doi.org/10.1063/5.0057511.

[22] H A Hafez, X Chai, A Ibrahim, S Mondal, D Férachou, X Ropagnol, and T Ozaki. Intense terahertz radiation and their applications. *Journal of Optics*, 18(9):093004, aug 2016. doi: 10.1088/2040-8978/18/9/093004. URL https://dx.doi.org/10.1088/2040-8978/18/9/093004.

[23] Martin van Exter, Ch. Fattinger, and D. Grischkowsky. Terahertz time-domain spectroscopy of water vapor. *Opt. Lett.*, 14(20):1128–1130, Oct 1989. doi: 10.1364/OL.14.001128. URL https://opg.optica.org/ol/abstract.cfm?URI=ol-14-20-1128.

[24] M M Nazarov, A P Shkurinov, E A Kuleshov, and V V Tuchin. Terahertz time-domain spectroscopy of biological tissues. *Quantum Electronics*, 38(7):647, jul 2008. doi: 10.1070/QE2008v038n07ABEH013851. URL https://dx.doi.org/10.1070/QE2008v038n07ABEH013851.

[25] John David Jackson. *Classical Electrodynamics, 3rd Edition*. 1998.

[26] A. Rice, Y. Jin, X. F. Ma, X.-C. Zhang, D. Bliss, J. Larkin, and M. Alexander. Terahertz optical rectification from ⟨110⟩ zinc-blende crystals. *Applied Physics Letters*, 64(11):1324–1326, 1994. doi: 10.1063/1.111922. URL https://doi.org/10.1063/1.111922.

[27] V Apostolopoulos and M E Barnes. Thz emitters based on the photo-dember effect. *Journal of Physics D: Applied Physics*, 47(37):374002, aug 2014. doi: 10.1088/0022-3727/47/37/374002. URL https://dx.doi.org/10.1088/0022-3727/47/37/374002.

[28] R A Lewis. A review of terahertz sources. *Journal of Physics D: Applied Physics*, 47(37):374001, aug 2014. doi: 10.1088/0022-3727/47/37/374001. URL https://dx.doi.org/10.1088/0022-3727/47/37/374001.

[29] E. V. Suvorov, R. A. Akhmedzhanov, D. A. Fadeev, I. E. Ilyakov, V. A. Mironov, and B. V. Shishkin. Terahertz emission from a metallic surface induced by a femtosecond optic pulse. *Opt. Lett.*, 37(13):2520–2522, Jul 2012. doi: 10.1364/OL.37.002520. URL https://opg.optica.org/ol/abstract.cfm?URI=ol-37-13-2520.

[30] G K P Ramanandan, G Ramakrishnan, N Kumar, A J L Adam, and P C M Planken. Emission of terahertz pulses from nanostructured metal surfaces. *Journal of Physics D: Applied Physics*, 47(37):374003, aug 2014. doi: 10.1088/0022-3727/47/37/374003. URL https://doi.org/10.1088/0022-3727/47/37/374003.

[31] S Swann. Magnetron sputtering. *Physics in Technology*, 19(2):67, mar 1988. doi: 10.1088/0305-4624/19/2/304. URL https://dx.doi.org/10.1088/0305-4624/19/2/304.

[32] Fred A. Stevie and Carrie L. Donley. Introduction to x-ray photoelectron spectroscopy. *Journal of Vacuum Science & Technology A*, 38(6):063204, 2020. doi: 10.1116/6.0000412. URL https://doi.org/10.1116/6.0000412.

[33] Y. Waseda, E. Matsubara, and K. Shinoda. *X-Ray Diffraction Crystallography: Introduction, Examples and Solved Problems*. Springer Berlin Heidelberg, 2011. ISBN 9783642166358. URL https://books.google.it/books?id=vk9fnLH56DYC.

[34] P. K. Hansma, J. P. Cleveland, M. Radmacher, D. A. Walters, P. E. Hillner, M. Bezanilla, M. Fritz, D. Vie, H. G. Hansma, C. B. Prater, J. Massie, L. Fukunaga, J. Gurley, and V. Elings. Tapping mode atomic force microscopy in liquids. *Applied Physics Letters*, 64(13):1738–1740, 03 1994. ISSN 0003-6951. doi: 10.1063/1.111795. URL https://doi.org/10.1063/1.111795.

[35] David C. Joy and James B. Pawley. High-resolution scanning electron microscopy. *Ultramicroscopy*, 47(1):80–100, 1992. ISSN 0304-3991. doi: https://doi.org/10.1016/0304-3991(92)90186-N. URL https://www.sciencedirect.com/science/article/pii/030439919290186N.

[36] Irene Prencipe, Daniele Rizzo David Dellasega, Alessandro Zani, and Matteo Passoni. Energy dispersive x-ray spectroscopy for nanostructured thin film density evaluation. *Science and Technology of Advanced Materials*, 16(2):025007, 2015. doi: 10.1088/1468-6996/16/2/025007.

[37] Georgi L. Dakovski, Brian Kubera, and Jie Shan. Localized terahertz generation via optical rectification in znte. *J. Opt. Soc. Am. B*, 22(8):1667–1670, Aug 2005. doi: 10.1364/JOSAB.22.001667. URL https://opg.optica.org/josab/abstract.cfm?URI=josab-22-8-1667.

[38] Ajay Nahata, Aniruddha S. Weling, and Tony F. Heinz. A wideband coherent terahertz spectroscopy system using optical rectification and electro-optic sampling. *Applied Physics Letters*, 69(16):2321–2323, 1996. doi: 10.1063/1.117511. URL https://doi.org/10.1063/1.117511.

[39] Ajay Nahata, James T. Yardley, and Tony F. Heinz. Free-space electro-optic detection of continuous-wave terahertz radiation. *Applied Physics Letters*, 75(17):2524–2526, 10 1999. ISSN 0003-6951. doi: 10.1063/1.125065. URL https://doi.org/10.1063/1.125065.

[40] Paul C. M. Planken, Han-Kwang Nienhuys, Huib J. Bakker, and Tom Wenckebach. Measurement and calculation of the orientation dependence of terahertz pulse detection in znte. *J. Opt. Soc. Am. B*, 18(3):313–317, Mar 2001. doi: 10.1364/JOSAB.18.000313. URL https://opg.optica.org/josab/abstract.cfm?URI=josab-18-3-313.

[41] Q. Wu and X.-C. Zhang. Ultrafast electro-optic field sensors. *Applied Physics Letters*, 68(12):1604–1606, 03 1996. ISSN 0003-6951. doi: 10.1063/1.115665. URL https://doi.org/10.1063/1.115665.

[42] N. van der Valk. *Towards terahertz microscopy*. PhD thesis, Delft University of technology, 2005.

[43] M L Meade. Advances in lock-in amplifiers. *J.*, 15(4):395, apr 1982. doi: 10.1088/0022-3735/15/4/001. URL https://dx.doi.org/10.1088/0022-3735/15/4/001.

[44] D. A. Van Baak and George Herold. Response of a lock-in amplifier to noise. *American Journal of Physics*, 82(8):785–797, 08 2014. ISSN 0002-9505. doi: 10.1119/1.4873915. URL https://doi.org/10.1119/1.4873915.

[45] J. M. Liu. Simple technique for measurements of pulsed gaussian-beam spot sizes. *Opt. Lett.*, 7(5):196–198, May 1982. doi: 10.1364/OL.7.000196.

[46] Ester Abram, Igor Milov, Nikolai Orlov, Klaasjan van Druten, Erik C. Garnett, and Paul Planken. Pre-ablation regime light-induced optical changes in nanometer thick metal films. *Opt. Express*, 32(3):4564–4587, Jan 2024. doi: 10.1364/OE.507689. URL https://opg.optica.org/oe/abstract.cfm?URI=oe-32-3-4564.

[47] Lan Jiang and Hai-Lung Tsai. Improved Two-Temperature Model and Its Application in Ultrashort Laser Heating of Metal Films. *Journal of Heat Transfer*, 127(10):1167–1173, 06 2005. ISSN 0022-1481. doi: 10.1115/1.2035113. URL https://doi.org/10.1115/1.2035113.

[48] Fedor Akhmetov, Igor Milov, Sergey Semin, Fabio Formisano, Nikita Medvedev, Jacobus M. Sturm, Vasily V. Zhakhovsky, Igor A. Makhotkin, Alexey Kimel, et al. Laser-induced electron dynamics and surface modification in ruthenium thin films. *Vacuum*, 212:112045, 2023. ISSN 0042-207X. doi: https://doi.org/10.1016/j.vacuum.2023.112045. URL https://www.sciencedirect.com/science/article/pii/S0042207X23002427.

[49] D.J. Griffiths. *Introduction to Electrodynamics*. Cambridge University Press, 2023. ISBN 9781009397759. URL https://books.google.it/books?id=I9jbEAAAQBAJ.

[50] Vitalyi E. Gusev and Oliver B. Wright. Ultrafast nonequilibrium dynamics of electrons in metals. *Phys. Rev. B*, 57:2878–2888, Feb 1998. doi: 10.1103/PhysRevB.57.2878. URL https://link.aps.org/doi/10.1103/PhysRevB.57.2878.

[51] Hee Jun Shin, Jeong-Min Lee, Seongkwang Bae, Woo-Hee Kim, and Sangwan Sim. Metal-insulator transition and interfacial thermal transport in atomic layer

deposited ru nanofilms characterized by ultrafast terahertz spectroscopy. *Applied Surface Science*, 563:150184, 2021. ISSN 0169-4332. doi: https://doi.org/10.1016/j.apsusc.2021.150184. URL https://www.sciencedirect.com/science/article/pii/S0169433221012605.

[52] R.I. Hickson, S.I. Barry, G.N. Mercer, and H.S. Sidhu. Finite difference schemes for multilayer diffusion. *Mathematical and Computer Modelling*, 54 (1):210–220, 2011. ISSN 0895-7177. doi: https://doi.org/10.1016/j.mcm.2011.02.003. URL https://www.sciencedirect.com/science/article/pii/S0895717711000938.

[53] Vitalij L. Malevich, Ramūnas Adomavičius, and Arūnas Krotkus. Thz emission from semiconductor surfaces. *Comptes Rendus Physique*, 9(2):130–141, 2008. ISSN 1631-0705. doi: https://doi.org/10.1016/j.crhy.2007.09.014. URL https://www.sciencedirect.com/science/article/pii/S163107050700240X. Recent developments in terahertz optoelectronics.

[54] D. Côté, J. M. Fraser, M. DeCamp, P. H. Bucksbaum, and H. M. van Driel. Thz emission from coherently controlled photocurrents in gaas. *Applied Physics Letters*, 75(25):3959–3961, 1999. doi: 10.1063/1.125531. URL https://doi.org/10.1063/1.125531.

[55] Sergey Vainshtein, Juha Kostamovaara, Valentin Yuferev, Wojciech Knap, Abdel Fatimy, and Nina Diakonova. Terahertz emission from collapsing field domains during switching of a gallium arsenide bipolar transistor. *Phys. Rev. Lett.*, 99:176601, Oct 2007. doi: 10.1103/PhysRevLett.99.176601. URL https://link.aps.org/doi/10.1103/PhysRevLett.99.176601.

[56] M. Venkatesh and A.K. Chaudhary. Generation of temporally shaped terahertz (thz) pulses from zinc telluride (znte) crystal using tunable femtosecond laser wavelengths. In *13th International Conference on Fiber Optics and Photonics*, page Tu4A.17. Optica Publishing Group, 2016. doi: 10.1364/PHOTONICS.2016.Tu4A.17. URL https://opg.optica.org/abstract.cfm?URI=Photonics-2016-Tu4A.17.

[57] Xiaojun Wu, Sergio Carbajo, Koustuban Ravi, Frederike Ahr, Giovanni Cirmi, Yue Zhou, Oliver D. Mücke, and Franz X. Kärtner. Terahertz generation in lithium niobate driven by ti:sapphire laser pulses and its limitations. *Opt. Lett.*, 39(18):5403–5406, Sep 2014. doi: 10.1364/OL.39.005403. URL https://opg.optica.org/ol/abstract.cfm?URI=ol-39-18-5403.

[58] Kodo Kawase, Manabu Sato, Tetsuo Taniuchi, and Hiromasa Ito. Coherent tunable thz-wave generation from linbo3 with monolithic grating coupler. *Applied Physics Letters*, 68(18):2483–2485, 1996. ISSN 0003-6951. doi: 10.1063/1.115828.

[59] E. Beaurepaire, G. M. Turner, S. M. Harrel, M. C. Beard, J.-Y. Bigot, and C. A. Schmuttenmaer. Coherent terahertz emission from ferromagnetic films excited by femtosecond laser pulses. *Applied Physics Letters*, 84(18):3465–3467, 2004. doi: 10.1063/1.1737467. URL https://doi.org/10.1063/1.1737467.

[60] D. J. Hilton, R. D. Averitt, C. A. Meserole, G. L. Fisher, D. J. Funk, J. D. Thompson, and A. J. Taylor. Terahertz emission via ultrashort-pulse excitation of magnetic metalfilms. *Opt. Lett.*, 29(15):1805–1807, Aug 2004. doi: 10.1364/OL.29.001805. URL https://opg.optica.org/ol/abstract.cfm?URI=ol-29-15-1805.

[61] Filip Kadlec, Petr Kužel, and Jean-Louis Coutaz. Optical rectification at metal surfaces. *Opt. Lett.*, 29(22):2674–2676, Nov 2004. doi: 10.1364/OL.29.002674. URL https://opg.optica.org/ol/abstract.cfm?URI=ol-29-22-2674.

[62] Filip Kadlec, Petr Kužel, and Jean-Louis Coutaz. Study of terahertz radiation generated by optical rectification on thin gold films. *Opt. Lett.*, 30(11):1402–1404, Jun 2005. doi: 10.1364/OL.30.001402. URL https://opg.optica.org/ol/abstract.cfm?URI=ol-30-11-1402.

[63] Liangliang Zhang, Fabrizio Buccheri, Cunlin Zhang, and X.-C. Zhang. Terahertz emission from thin metal films with porous nanostructures. *Applied Physics Letters*, 107(7):071107, 2015. doi: 10.1063/1.4929404. URL https://doi.org/10.1063/1.4929404.

[64] Stefan A Maier. *Plasmonics: fundamentals and applications*, volume 1. Springer, 2007.

[65] Justyna Zawadzka, Dino A. Jaroszynski, John J. Carey, and Klaas Wynne. Evanescent-wave acceleration of ultrashort electron pulses. *Applied Physics Letters*, 79(14):2130–2132, 10 2001. ISSN 0003-6951. doi: 10.1063/1.1406562. URL https://doi.org/10.1063/1.1406562.

[66] Gregor H. Welsh, Neil T. Hunt, and Klaas Wynne. Terahertz-pulse emission through laser excitation of surface plasmons in a metal grating. *Phys. Rev. Lett.*, 98: 026803, Jan 2007. doi: 10.1103/PhysRevLett.98.026803. URL https://link.aps.org/doi/10.1103/PhysRevLett.98.026803.

[67] Gopakumar Ramakrishnan and Paul C. M. Planken. Percolation-enhanced generation of terahertz pulses by optical rectification on ultrathin gold films. *Opt. Lett.*, 36(13):2572–2574, Jul 2011. doi: 10.1364/OL.36.002572. URL https://opg.optica.org/ol/abstract.cfm?URI=ol-36-13-2572.

[68] Gopakumar Ramakrishnan, Gopika K. P. Ramanandan, Aurèle J. L. Adam, Man Xu, Nishant Kumar, Ruud W. A. Hendrikx, and Paul C. M. Planken. Enhanced terahertz emission by coherent optical absorption in ultrathin semiconductor films on

metals. *Opt. Express*, 21(14):16784–16798, Jul 2013. doi: 10.1364/OE.21.016784. URL https://opg.optica.org/oe/abstract.cfm?URI=oe-21-14-16784.

[69] S. van Vliet, A. Troglia, E. Olsson, and R. Bliem. Identifying silicides via plasmon loss satellites in photoemission of the ru-si system. *Applied Surface Science*, 608:155139, 2023. ISSN 0169-4332. doi: https://doi.org/10.1016/j.apsusc.2022.155139. URL https://www.sciencedirect.com/science/article/pii/S0169433222026678.

[70] David Nečas and Petr Klapetek. Gwyddion: an open-source software for spm data analysis. *Open Physics*, 10(1):181–188, 2012. doi: doi:10.2478/s11534-011-0096-2. URL https://doi.org/10.2478/s11534-011-0096-2.

[71] Mischa Bonn, Daniel N. Denzler, Stephan Funk, Martin Wolf, S.-Svante Wellershoff, and Julius Hohlfeld. Ultrafast electron dynamics at metal surfaces: Competition between electron-phonon coupling and hot-electron transport. *Phys. Rev. B*, 61:1101–1105, Jan 2000. doi: 10.1103/PhysRevB.61.1101. URL https://link.aps.org/doi/10.1103/PhysRevB.61.1101.

[72] David J. Morgan. Resolving ruthenium: Xps studies of common ruthenium materials. *Surface and Interface Analysis*, 47(11):1072–1079, 2015. doi: https://doi.org/10.1002/sia.5852. URL https://analyticalsciencejournals.onlinelibrary.wiley.com/doi/abs/10.1002/sia.5852.

[73] Marc Assael, S. Botsios, K. Gialou, and Ifigeneia Metaxa. Thermal conductivity of polymethyl methacrylate (pmma) and borosilicate crown glass bk7. *International Journal of Thermophysics*, 26:1595–1605, 01 2005. doi: 10.1007/s10765-005-8106-5.

[74] Stanley S. Ballard, Kathryn A. McCarthy, and William C. Davis. A method for measuring the thermal conductivity of small samples of poorly conducting materials such as optical crystals. *Review of Scientific Instruments*, 21(11):905–907, 1950. doi: 10.1063/1.1745460. URL https://doi.org/10.1063/1.1745460.

[75] Kathryn A. McCarthy and Stanley S. Ballard. New data on the thermal conductivity of optical crystals*. *J. Opt. Soc. Am.*, 41(12):1062–1063, Dec 1951. doi: 10.1364/JOSA.41.001062. URL https://opg.optica.org/abstract.cfm?URI=josa-41-12-1062.

[76] Emil V. Jelenkovic and K. Y. Tong. Thermally grown ruthenium oxide thin films. *Journal of Vacuum Science & Technology B: Microelectronics and Nanometer Structures Processing, Measurement, and Phenomena*, 22(5):2319–2325, 2004. doi: 10.1116/1.1783319. URL https://avs.scitation.org/doi/abs/10.1116/1.1783319.

[77] R. Coloma Ribera, R. W. E. van de Kruijs, S. Kokke, E. Zoethout, A. E. Yakshin, and F. Bijkerk. Surface and sub-surface thermal oxidation of thin ruthenium films. *Applied Physics Letters*, 105(13):131601, 2014. doi: 10.1063/1.4896993. URL https://doi.org/10.1063/1.4896993.

[78] Jian Shen, Dan Zhang, Fei-Hu Zhang, and Yang Gan. Afm tip-sample convolution effects for cylinder protrusions. *Applied Surface Science*, 422:482–491, 2017. ISSN 0169-4332. doi: https://doi.org/10.1016/j.apsusc.2017.06.053. URL https://www.sciencedirect.com/science/article/pii/S0169433217317087.

[79] J Trey Diulus, Benjamin Tobler, Jürg Osterwalder, and Zbynek Novotny. Thermal oxidation of ru(0001) to ruo2(110) studied with ambient pressure x-ray photoelectron spectroscopy. *Journal of Physics D: Applied Physics*, 54(24):244001, mar 2021. doi: 10.1088/1361-6463/abedfd. URL https://dx.doi.org/10.1088/1361-6463/abedfd.

[80] Yoshitaka Murakami, Jinwang Li, and Tatsuya Shimoda. Highly conductive ruthenium oxide thin films by a low-temperature solution process and green laser annealing. *Materials Letters*, 152:121–124, 2015. ISSN 0167-577X. doi: https://doi.org/10.1016/j.matlet.2015.03.084. URL https://www.sciencedirect.com/science/article/pii/S0167577X15004486.

[81] Seungmin Yeo, Ji-Yoon Park, Seung-Joon Lee, Do-Joong Lee, Jong Hyun Seo, and Soo-Hyun Kim. Ruthenium and ruthenium dioxide thin films deposited by atomic layer deposition using a novel zero-valent metalorganic precursor, (ethylbenzene)(1,3-butadiene)ru(0), and molecular oxygen. *Microelectronic Engineering*, 137:16–22, 2015. ISSN 0167-9317. doi: https://doi.org/10.1016/j.mee.2015.02.026. URL https://www.sciencedirect.com/science/article/pii/S0167931715000787. Materials for Advanced Metallization 2014.

[82] L. Pasquali, N. Mahne, M. Montecchi, V. Mattarello, and S. Nannarone. Formation and distribution of compounds at the ru–si(001) ultrathin film interface. *Journal of Applied Physics*, 105(4):044304, 2009. doi: 10.1063/1.3079507. URL https://doi.org/10.1063/1.3079507.

[83] Christian Chatillon, Ioana Nuta, Fatima-Zhara Roki, and Evelyne Fischer. Chemical thermodynamics of ruo2(s). *Journal of Nuclear Materials*, 509:742–751, 2018. ISSN 0022-3115. doi: https://doi.org/10.1016/j.jnucmat.2018.05.060. URL https://www.sciencedirect.com/science/article/pii/S0022311518307001.

[84] Sheng Zhang, Yongwei Cui, Shunjia Wang, Haoran Chen, Yaxin Liu, Wentao Qin, Tongyang Guan, Chuanshan Tian, Zhe Yuan, and Lei Zhou et al. Nonrelativistic and nonmagnetic terahertz-wave generation via ultrafast current control in anisotropic conductive heterostructures. *Advanced Photonics*, 5(5):056006,

2023. doi: 10.1117/1.AP.5.5.056006. URL https://doi.org/10.1117/1.AP.5.5.056006.

[85] Burak Guzelturk, Antonio B. Mei, Lei Zhang, Liang Z. Tan, Patrick Donahue, Anisha G. Singh, Darrell G. Schlom, Lane W. Martin, and Aaron M. Lindenberg. Light-induced currents at domain walls in multiferroic bifeo3. *Nano Letters*, 20(1): 145–151, 2020. doi: 10.1021/acs.nanolett.9b03484. URL https://doi.org/10.1021/acs.nanolett.9b03484. PMID: 31746607.

[86] Baoping Bob He, Uwe Preckwinkel, Kingsley L. Smith, and Bruker Analytical. Fundamentals of two-dimensional x-ray diffraction (xrd 2). 2000. URL https://api.semanticscholar.org/CorpusID:387241.

[87] Erik Milosevic, Sit Kerdsongpanya, Amirali Zangiabadi, Katayun Barmak, Kevin R. Coffey, and Daniel Gall. Resistivity size effect in epitaxial Ru(0001) layers. *Journal of Applied Physics*, 124(16):165105, October 2018. doi: 10.1063/1.5046430.

[88] H. Zhong, G. Heuss, and V. Misra. Electrical properties of ruo_2 gate electrodes for dual metal gate si-cmos. *IEEE Electron Device Letters*, 21(12):593–595, 2000. doi: 10.1109/55.887476.

[89] Il-Hwan Kim and Kwang-Bum Kim. Ruthenium oxide thin film electrodes for supercapacitors. *Electrochemical and Solid-State Letters*, 4(5):A62, mar 2001. doi: 10.1149/1.1359956.

[90] Nezih Pala and Mustafa Karabiyik. *Electron Beam Lithography (EBL)*, pages 1033–1057. Springer Netherlands, Dordrecht, 2016. ISBN 978-94-017-9780-1. doi: 10.1007/978-94-017-9780-1_344. URL https://doi.org/10.1007/978-94-017-9780-1_344.

[91] W. F. van Dorp and C. W. Hagen. A critical literature review of focused electron beam induced deposition. *Journal of Applied Physics*, 104(8):081301, 10 2008. ISSN 0021-8979. doi: 10.1063/1.2977587.

[92] Steven M. George. Atomic layer deposition: An overview. *Chemical Reviews*, 110 (1):111–131, 2010. doi: 10.1021/cr900056b. PMID: 19947596.

[93] Adriaan J. M. Mackus, Marc J. M. Merkx, and Wilhelmus M. M. Kessels. From the bottom-up: Toward area-selective atomic layer deposition with high selectivity. *Chemistry of Materials*, 31(1):2–12, 2019. doi: 10.1021/acs.chemmater.8b03454. PMID: 30774194.

[94] Toshihiko Kaneda, Daisuke Hirose, Takaaki Miyasako, Phan Trong Tue, Yoshitaka Murakami, Shinji Kohara, Jinwang Li, Tadaoki Mitani, Eisuke Tokumitsu, and Tatsuya Shimoda. Rheology printing for metal-oxide patterns and devices. *J. Mater. Chem. C*, 2:40–49, 2014. doi: 10.1039/C3TC31842G.

[95] Lorenzo Cruciani, Stefan van Vliet, Alessandro Troglia, Roland Bliem, Klaasjan van Druten, and Paul Planken. Femtosecond laser-induced emission of coherent terahertz pulses from ruthenium thin films. *The Journal of Physical Chemistry C*, 127 (46):22662–22672, 2023. doi: 10.1021/acs.jpcc.3c05525.

[96] A. Jablonski and J. Zemek. Overlayer thickness determination by xps using the multiline approach. *Surface and Interface Analysis*, 41(3):193–204, 2009. doi: https://doi.org/10.1002/sia.3005.

[97] Alexander G. Shard. A straightforward method for interpreting xps data from core–shell nanoparticles. *The Journal of Physical Chemistry C*, 116(31):16806–16813, 2012. doi: 10.1021/jp305267d.

[98] Marnix Vreugdenhil and Dries van Oosten. A highly automated apparatus for ultrafast laser ablation studies. *Review of Scientific Instruments*, 93(7):073003, 07 2022. ISSN 0034-6748. doi: 10.1063/5.0095719.

[99] Felipe Oliveira, Rafael Cipriano, Felipe Silva, Estaner Romão, and C. dos Santos. Simple analytical method for determining electrical resistivity and sheet resistance using the van der pauw procedure. *Scientific Reports*, 10, 10 2020. doi: 10.1038/s41598-020-72097-1.

[100] D. Ugur, A. J. Storm, R. Verberk, J. C. Brouwer, and W. G. Sloof. Kinetics of reduction of a ruo2(110) film on ru(0001) by h2. *The Journal of Physical Chemistry C*, 116(51):26822–26828, 2012. doi: 10.1021/jp309905z.

[101] Akira Izumi, Tomoya Ueno, Yasuo Miyazaki, Hiroaki Oizumi, and Iwao Nishiyama. Reduction of oxide layer on various metal surfaces by atomic hydrogen treatment. *Thin Solid Films*, 516(5):853–855, 2008. ISSN 0040-6090. doi: https://doi.org/10.1016/j.tsf.2007.06.094. Proceedings of the Fourth International Conference on Hot-Wire CVD Cat-CVD Process.

[102] Hee Jun Shin, Jeong-Min Lee, Seongkwang Bae, Woo-Hee Kim, and Sangwan Sim. Metal-insulator transition and interfacial thermal transport in atomic layer deposited ru nanofilms characterized by ultrafast terahertz spectroscopy. *Applied Surface Science*, 563:150184, 2021. ISSN 0169-4332. doi: https://doi.org/10.1016/j.apsusc.2021.150184. URL https://www.sciencedirect.com/science/article/pii/S0169433221012605.

[103] J. Hohlfeld, S.-S. Wellershoff, J. Güdde, U. Conrad, V. Jähnke, and E. Matthias. Electron and lattice dynamics following optical excitation of metals. *Chemical Physics*, 251(1):237–258, 2000. ISSN 0301-0104. doi: https://doi.org/10.1016/S0301-0104(99)00330-4.

[104] Dooho Choi and Katayun Barmak. On the potential of tungsten as next-generation semiconductor interconnects. *Electronic Materials Letters*, 13:449–456, 2017. URL https://api.semanticscholar.org/CorpusID:136283025.

[105] Jun Hwan Moon, Eunjin Jeong, Seunghyun Kim, Taesoon Kim, Eunsoo Oh, Keun Lee, Hauk Han, and Young Keun Kim. Materials quest for advanced interconnect metallization in integrated circuits. *Advanced Science*, 10(23):2207321, 2023. doi: https://doi.org/10.1002/advs.202207321. URL https://onlinelibrary.wiley.com/doi/abs/10.1002/advs.202207321.

[106] Erik Milosevic, Sit Kerdsongpanya, Amirali Zangiabadi, Katayun Barmak, Kevin R. Coffey, and Daniel Gall. Resistivity size effect in epitaxial Ru(0001) layers. *Journal of Applied Physics*, 124(16):165105, October 2018. doi: 10.1063/1.5046430.

[107] Liang Gong Wen, Philippe Roussel, Olalla Varela Pedreira, Basoene Briggs, Benjamin Groven, Shibesh Dutta, Mihaela I. Popovici, Nancy Heylen, Ivan Ciofi, Kris Vanstreels, Frederik W. Østerberg, Ole Hansen, Dirch H. Petersen, Karl Opsomer, Christophe Detavernie, Christopher J. Wilson, Sven Van Elshocht, Kristof Croes, Jürgen Bömmels, Zsolt Tőkei, and Christoph Adelmann. Atomic layer deposition of ruthenium with tin interface for sub-10 nm advanced interconnects beyond copper. *ACS Applied Materials & Interfaces*, 8(39):26119–26125, 2016. doi: 10.1021/acsami.6b07181. URL https://doi.org/10.1021/acsami.6b07181. PMID: 27598509.

[108] Shruti Gupta, Mangalika Sinha, R. Dhawan, R. Jangir, A. Bose, P. Gupta, M.K. Swami, and Mohammed H Modi. Study of oxidation behaviour of ruthenium thin film after thermal annealing in oxygen environment. *Thin Solid Films*, 764:139606, 2023. ISSN 0040-6090. doi: https://doi.org/10.1016/j.tsf.2022.139606.

[109] H.-C. Wen, P. Lysaght, H. N. Alshareef, C. Huffman, H. R. Harris, K. Choi, Y. Senzaki, H. Luan, P. Majhi, B. H. Lee, M. J. Campin, B. Foran, G. D. Lian, and D.-L. Kwong. Thermal response of Ru electrodes in contact with SiO_2 and Hf-based high-k gate dielectrics. *Journal of Applied Physics*, 98(4):043520, 08 2005. ISSN 0021-8979. doi: 10.1063/1.2012510. URL https://doi.org/10.1063/1.2012510.

[110] Sergiy Yulin, Nicolas Benoit, Torsten Feigl, Norbert Kaiser, Ming Fang, and Manish Chandhok. Mo/Si multilayers with enhanced TiO_2- and RuO_2-capping layers. In Frank M. Schellenberg, editor, *Emerging Lithographic Technologies XII*, volume 6921, page 692118. International Society for Optics and Photonics, SPIE, 2008. doi: 10.1117/12.772653. URL https://doi.org/10.1117/12.772653.

[111] Lorenzo Cruciani, Marnix Vreugdenhil, Stefan van Vliet, Ester Abram, Dries van Oosten, Roland Bliem, Klaasjan van Druten, and Paul Planken. Direct laser patterning of ruthenium below the optical diffraction limit. *Applied Physics Letters*,

124(17):171902, 04 2024. ISSN 0003-6951. doi: 10.1063/5.0205538. URL https://doi.org/10.1063/5.0205538.

[112] Nenad Milošević and Ivana Nikolić. Thermophysical properties of solid phase ruthenium measured by the pulse calorimetry technique over a wide temperature range. *International Journal of Materials Research*, 106(4):361–367, 2015. doi: doi:10.3139/146.111192. URL https://doi.org/10.3139/146.111192.